Submesoscale Statistics from Surface Drifters: Biases and Benefits

by
Jenna Pearson
B. A., Mathematics, Northeastern Illinois University, 2014
B. A., Earth Science, Northeastern Illinois University, 2014

A dissertation submitted in partial fulfillment of the
requirements for the Degree of Doctor of Philosophy in
the Department of Earth, Environmental and Planetary Sciences
at Brown University

Providence, Rhode Island
May 2020

This dissertation by Jenna Pearson is accepted in its present form
by the Department of Earth, Environmental and Planetary Sciences
as satisfying the dissertation requirement for the degree of Doctor of Philosophy.

Date _____ _____
Baylor Fox-Kemper, Advisor

Recommended to the Graduate Council

Date _____ _____
Scott Bachman, Reader
(Oceanography Section, NCAR)

Date _____ _____
Donald Forsyth, Reader

Date _____ _____
Timothy Herbert, Reader

Date _____ _____
John Bradley Marston, Reader
(Department of Physics)

Date _____ _____
Björn Sandstede, Reader
(Division of Applied Mathematics)

Approved by the Graduate Council

Date _____ _____
Andrew G. Campbell
Dean of the Graduate School

JENNA L. PEARSON

PhD Candidate of Earth, Environmental, & Planetary Sciences

Brown University, 167 Thayer St., Providence, RI 02912

jenna_pearson@brown.edu | jlpearso.github.io

Education

PhD in Earth, Environmental and Planetary Sciences 2015-Expected 2020
Advisor: Prof. Baylor Fox-Kemper *Brown University*

B.A. in Mathematics 2008-2014
Advisor: Prof. Lidia Filus *Northeastern Illinois University*
Magna cum laude

B.A. in Earth Science 2008-2014
Advisor: Prof. Ken Voglesonger *Northeastern Illinois University*
Magna cum laude

Professional & Teaching Experience

Graduate Research Assistant Fall 2015-Present
Advisor: Prof. Baylor Fox-Kemper *Brown University*
Statistical methods paired with models, observations, and theory to isolate biases in Lagrangian observation platforms as well as characterize reactive-tracer fields in the presence of turbulence

Course Designer and Co-instructor for Summer @ Brown Summer 2018 - 2019
Studying the Ocean from the Classroom to the Bay taught with Abigail Bodner *Brown University*
Developed and co-taught a two-week summer course introducing pre-college students to oceanography

Graduate Teaching Assistant Spring 2019
Intro. to Oceanography under Prof. Steve Clemens *Brown University*

Graduate Teaching Assistant Fall 2017
Global Climate & Weather under Prof. Amanda Lynch *Brown University*

Undergraduate Researcher Summer 2014
Advisor: Prof. Björn Sandstede, Division of Applied Mathematics *Brown University*
Analysis of data assimilation and parameter estimation schemes applied to traffic models

Undergraduate Researcher Summer 2013
Advisor: Prof. Alkes Price, Department of Epidemiology *Harvard University*
Statistical methods to infer consistency across populations of genetic variants associated with type-II diabetes

U.S. Army National Guard 2005-2013
Served in Iraq as an E-4 Specialist during 2011, honorably discharged in 2013.
Health care specialist, as well as medical trainer for the State of IL and in Balad, Iraq

Publications

1. **Pearson, J.**, Fox-Kemper, B., Pearson, B., Chang, H., Huntley, H., Haus, B., Horstmann, J., Huntley, H., Kirwan, D. A., Jr., Poje, A., *Under Review*: Biases in structure functions from observations of submesoscale flows. *Journal of Geophysical Research: Oceans.*

2. Chang, H., Huntley, H., Kirwan, D., Jr., Carlson, D., Mensa, J., Mehta, S., Novelli, G., Ozgokomen, T., Fox-Kemper, B., Pearson, B., **Pearson, J.**, Harcourt, R., 2019: Small-scale dispersion observations in the presence of Langmuir circulation. *Journal of Physical Oceanography. 49, 3069-3085* DOI

3. **Pearson, J.**, Fox-Kemper, B., Barkan, R., Choi, J., Bracco, A., & McWilliams, J., 2019: Impacts of convergence on structure functions from surface drifters in the Gulf of Mexico. *Journal of Physical Oceanography, 49, 675-690.* DOI

4. Xia, C., Cochrane, C., DeGuire, J., Fan, G., Holmes, E., McGuirl, M., Murphy, P., **Palmer, J.**, Carter, P., Slivinski, L., & Sandstede, B., 2017: Assimilating Eulerian and Lagrangian data in traffic-flow models. *Physica D: Nonlinear Phenomena*, 346, 59-72. DOI

Awards & Honors

Funding

Fluids and Health 2019 Junior Researcher Fellowship	2019
Brown University Graduate School Conference Travel Grant	2019
Brown University Graduate School International Travel Grant	2019
First Year Graduate Fellowship, Brown University	2015-2016
National Science Foundation MaPs Scholar, Northeastern Illinois University	2012-2014
National Institute for Mathematical and Biological Synthesis Travel Grant	2013
Society for Advancement of Chicanos and Native Americans in Science Travel Grant	2012

Honors

Tse Cheuk Ng Tai Innovations in Fluids and Health 2019 Award, Tse Cheuk Ng Tai Innovation Fund	2019
GoMRI Scholar, Gulf of Mexico Research Initiative	2018
Dean's List, Northeastern Illinois University	2008-2014
Army Achievement Medal, ILARNG	2011

For meritorious achievement, outstanding performance, personal sacrifice, and service as the primary instructor during the battalions Combat Lifesaver Course.

Command Sergeant Major's Award, ILARNG	2009

For outstanding service in successfully training soldiers in Combat Lifesaver skills, and performance of the highest standards befitting of soldiers who lead from the front.

Skills & Training

Computer Languages & Software: MATLAB, Python, R, Java and LaTeX

Community Earth System Model (CESM) Tutorial 2019 08/05-08/09 2019

1 week of lecture and hands on activities to learn to operate CESM. *NCAR, CO*

Cornell Satellite Remote Sensing Training Program 06/03-06/14 2019

2 week summer course on remote sensing with a focus on ocean color. *Ithaca, NY*

American Institute of Biological Sciences & RI NSF EPSCoR/RI C-AIM Feb 2019

Enabling Interdisciplinary and Team Science Workshop: A Professional Development Program from AIBS *Kingston, RI*

The Harriet W. Sheridan Center for Teaching and Learning Fall 2018

Certificate I: Reflective Teaching *Providence, RI*

GODAE Oceanview International School Fall 2017

New frontiers in operational oceanography — *Mallorca, Spain*

Consortium for Advanced Research on Transport of Hydrocarbon in the Environment III — Summer 2017

2 weeks launching driftcards in the Gulf of Mexico shelf area of LA — *Grande Isle, LA*

Northeastern Illinois University Field School — Summer 2014

2 weeks producing detailed geologic maps, stereonets, and reports on geomorphological and glacial features of the Baraboo syncline area — *Baraboo, WI*

Service & Outreach

Contributions

Big Bang Science Fair Demonstrator, Waterfire in Providence, RI	Sept 2019
Career Day Geosciences Speaker, Lincoln Middle School	Apr 2019
GradCon Coordinator, Brown University	2018-2019
Elementary School Science Instructor, Vartan Gregorian Elementary	2015 - 2016
GRE Math Preparation Course Instructor, Northeastern Illinois University	Aug 2015
EMERGE Peer Leader, Northeastern Illinois University	Jul-Aug 2015
Mathematics Enrichment Workshop Program Peer Leader, Northeastern Illinois University	2010-2012
Combat Lifesaver Course Coordinator and Instructor, ILARNG	2009-2011

Reviews

Reviewer, Ocean Science	2019-Present
Reviewer, Journal of Physical Oceanography	2019-Present
Reviewer, Journal of Fluid Mechanics	2018-Present
Expert Reviewer, Intergovernmental Panel on Climate Change	2018-2019

Departmental Service

International Graduate Student Mentor, Brown University	Fall 2017-2019
First Year Graduate Student Mentor, Brown University	Fall 2017 - Spring 2018
Geoclub Treasurer, Brown University	Fall 2016 - Spring 2017

Select Presentations

1. **Pearson, J.**, T., Sane, A., Ben-Horin, Fox-Kemper, B., 2019: Pathogen Dispersal in Narragansett Bay. Fluids and Health. **Oral**.

2. **Pearson, J.**, Fox-Kemper, B., Huntley, H., Chang, H., Kirwan, D., Jr., Pearson, B., 2019: Systematic Differences Between Eulerian and Surface Drifter Statistics in the Gulf of Mexico. AOFD, abstract 358490. Poster.

3. **Pearson, J.**, Fox-Kemper, B., Huntley, H., Chang, H., Kirwan, D., Jr., Pearson, B., 2019: Do surface drifters accurately represent Eulerian turbulence statistics? LAPCOD. **Oral**.

4. **Pearson, J.**, Fox-Kemper, B., Huntley, H., Chang, H., Kirwan, D., Jr., Pearson, B., 2019: Observed biases in surface drifter statistics in the Gulf of Mexico. CLIVAR. **Oral**.

5. **Pearson, J.**, Fox-Kemper, B., Barkan, R., Choi, J., Bracco, A., McWilliams, J., 2018: Impacts of convergence zones on Lagrangian structure function statistics in the Gulf of Mexico. GRS. Poster.

6. **Pearson, J.**, Fox-Kemper, B., Barkan, R., Choi, J., Bracco, A., McWilliams, J., 2018: Impacts of Convergence Zones on Lagrangian Structure Function Statistics in the Gulf of Mexico. KITP. Poster.

7. **Pearson, J.**, Fox-Kemper, B., Barkan, R., Choi, J., Bracco, A., McWilliams, J., 2018: Impacts of convergence zones on Lagrangian structure function statistics in the Gulf of Mexico. Waters Edge. Poster.

8. **Pearson, J.**, Fox-Kemper, B., Barkan, R., Choi, J., Bracco, A., McWilliams, J., 2018: Impacts of Convergence Zones on Lagrangian Structure Function Statistics in the Gulf of Mexico. OSM, abstract PS33A-01. Poster.

9. **Pearson, J.**, Fox-Kemper, B., Barkan, R., Choi, J., Bracco, A., McWilliams, J., 2017: Evaluation of Lagrangian Structure Function Statistics in the Gulf of Mexico. AOFD. **Oral**.

10. **Pearson, J.**, Fox-Kemper, B., Barkan, R., Choi, J., Bracco, A., McWilliams, J., 2017: Impacts of Convergence Zones on Lagrangian Structure Function Statistics in the Gulf of Mexico. GODAE International School. Poster.

11. **Pearson, J.**, Fox-Kemper, B., Bodner, A., 2016: Preparing for Model-Data Comparison: Structure Functions and Frontogenesis. CARTHE II All Hands Meeting. **Oral**.

12. **Pearson, J.**, Fox-Kemper, B., Barkan, R., Choi, J., Bracco, A., McWilliams, J., 2016: Structure Function Statistics to Detect Submesoscale Cascades. OSM, abstract PO34C-3066. Poster.

13. **Pearson, J.**, Xia, C., Cochrane, C., DeGuire, J., Fan, G., Holmes, E., McGuirl, M., Murphy, P., Carter, P., Slivinski, L., Sandstede, B., 2015: Microscopic and macroscopic traffic modeling utilizing data assimilation. The 5th Workshop in Statistical Mathematical Modeling. **Invited Oral**.

Affiliations and Memberships

Affiliate Graduate Student in the Institute at Brown for Environment Society (IBES)
Consortium for Advanced Research on Transport of Hydrocarbon in the Environment (CARTHE)
Graduate Fellow of the Rhode Island Consortium for Coastal Ecology Assessment Innovation & Modeling (RI C-AIM)
American Meteorological Society
American Geophysical Union
Graduate Women in Science & Engineering
Association for the Sciences of Limnology and Oceanography

Acknowledgements

While the science presented below reflects five years of my hard work, it would have been impossible without the support and guidance of many people and institutions. To begin, none of this research would have been feasible without generous funding from Brown University, the Office and Naval Research, and the Consortium for Advanced Research on Transport of Hydrocarbon in the Environment. I am also very fortunate to have had excellent mentorship throughout my academic career, and my PhD advisor Prof. Baylor Fox-Kemper is no exception to that rule. His welcoming personality and his intense scientific curiosity drew me into oceanography, and his deep passion for research and positive attitude kept me here. I will always remember going into his office during my first year disheartened about problems I was having or worried about lack of progress made, and then somehow always leaving his office feeling refreshed, inspired, and with a little less weight on my shoulders. His broad knowledge, insight, and resourcefulness was invaluable for the duration of my PhD, and I will certainly miss hearing his laughter echo through the halls of Geochem. I would also like to thank the other members of both my preliminary exam and PhD defense committees – Scott Bachman, Steve Clemens, Don Forsyth, Tim Herbert, Brad Marston, Martin Maxey, Björn Sandstede – for their thoughtful and provoking questions over the last four years that really helped shape this dissertation into a polished an approachable product.

I am also grateful to have been a part of such a supportive cohort and lab group at Brown. Thanks to Abigail Bodner for her extraordinary friendship, co-teaching skills, and the endless stream of photos and videos of her son Micah to remind me to smile and laugh throughout the day. Thanks to Bar Guzi for conspiring with Abigail to send said reminders, as well as providing me with good food, wine, and philosophy discussions. Thanks to Qing Li for starring in the "Ask Qing" show for many years, answering any and all questions regardless of the time of day or time required to answer them. Thank you to Leah Johnson for taking over for Qing when he graduated. Thank you to Aakash Sane and Chris Horvat for always having interesting stories, for your efforts (even those that were unsuccessful) in helping our summer course learn about drones, and creating a inviting lab environment. Thank you to Sydney Clark for the random coffee dates, and both Sydney and Noah Hammond for jam sessions and music outings. Thanks to Richard Vachula, Jack Krantz, Allison Jacobel, Johnny Ryan, and Sarah Cooley for excellent trivia nights, as well as guidance and feedback on my work over the years without complaint. Thanks to Jordyn and Travis Babikoff, as well as Rachel Sheppard, Matt Yeaton, Bry Power, and Ross Potter for game nights and escape rooms to

keep my mind sharp.

I am also in debt to all the other researchers that have shared their time, thoughtsa, and resources with me – Dhruv Balwada, Roy Barkan, Annalisa Bracco, Bianca Broman, Henry Chang, Jun Choi, Rabitah Daud, Helga Huntley, Denny Kirwan Jr., Jim McWilliams, Andrew Poje, and many, many others. These great discussions and insights ultimately broadened the scope of my work, and have helped me transition more smoothly into the future.

I am thankful for my sister Jessica, who inspired me to pursue higher education to begin with, and has always been an amazing example of overcoming your circumstances. I am appreciative of her positive energy, her sense of humor, and her constant praise and support of both my research, and me as a person.

Finally, I would like to thank my husband Brodie, for always being the brightest spot in my life during many stressful times throughout my PhD. Thank you for always believing me to be more capable than I thought, listening to me vent through waves of doubt and frustration, then confidence and successes, and for being my partner in everything – I couldn't have gotten to this point without you.

Contents

List of Tables xiii

List of Figures xiv

1 Introduction 1
- 1.1 Motivation . . . 1
  - 1.1.1 Ocean Turbulence . . . 1
  - 1.1.2 Submesoscale Dynamics . . . 1
  - 1.1.3 Measuring Ocean Turbulence with Surface Drifters . . . 3
  - 1.1.4 Upper Ocean Energetics . . . 4
- 1.2 Phenomenology . . . 5
  - 1.2.1 Statistical Models of Turbulence: K41 Theory . . . 5
  - 1.2.2 Beyond K41: Geophysical Turbulence . . . 8
- 1.3 Statistics . . . 12
  - 1.3.1 Eulerian Structure Functions . . . 12
    - Second-Order Structure Functions . . . 13
    - Helmholtz Decomposition . . . 14
    - Third-Order Structure Functions . . . 15
  - 1.3.2 Lagrangian Structure Functions and the Autocorrelation Function . . . 15
  - 1.3.3 Eddy Diffusivity and the Lagrangian Integral Time . . . 16
  - 1.3.4 Probability and Travel Time Maps . . . 19
- 1.4 Outline of Thesis . . . 19

2 Identifying the Bias: Systematic Biases in Eulerian Structure Functions Derived from Synthetic Surface Drifters 21
- 2.1 Introduction . . . 22
- 2.2 Model Configuration and Trajectory Details . . . 25
- 2.3 Methods . . . 27
  - 2.3.1 Structure Functions . . . 27
  - 2.3.2 Wilcoxon Rank Sum Test . . . 29

2.3.3 Helmholtz Decomposition . . . 29
2.3.4 Specifications . . . 31
2.4 Results . . . 31
2.4.1 Second Order Structure Functions . . . 31
2.4.2 Third Order Structure Functions . . . 35
2.4.3 Wilcoxon Rank Sum Test . . . 35
2.4.4 Helmholtz Decomposition . . . 36
2.5 Conclusions . . . 40
2.6 Acknowledgments . . . 41

3 Refining the Bias: Accumulation vs. Background Bias from Surface Drifter Observations 42
3.1 Introduction . . . 43
3.2 Data . . . 45
3.2.1 LASER Drifters . . . 45
3.2.2 X-band Radar . . . 46
3.2.3 Data Windows . . . 47
3.3 Methods . . . 47
3.3.1 Structure Functions . . . 47
3.3.2 Computational Details . . . 51
3.4 Results . . . 51
3.4.1 First-Order Structure Functions . . . 51
3.4.2 Second-Order Structure Functions . . . 53
Corrected Second-Order Structure Functions . . . 54
S_γ^2 as a Function of Divergence and Vorticity . . . 55
Biases in Second-Order Structure Functions at a Front . . . 56
Biases in Second-Order Structure Functions in a Vortex . . . 58
3.4.3 Third-order Structure Functions . . . 59
Corrected Third-Order Structure Functions . . . 60
S_γ^3 as a Function of Divergence and Vorticity . . . 61
Biases in Third-Order Structure Functions at a Front . . . 61
Biases in Third-Order Structure Functions at a Vortex . . . 62
3.5 Conclusions . . . 62

4 Benefits of the Bias: Corrected Estimates of Transport and Dispersion Parameters from Surface Drifter Observations 64
4.1 Introduction . . . 65
4.2 GLAD and LASER Drifters . . . 67
4.3 Methods . . . 67
4.3.1 Probability and Travel Time Maps . . . 67

4.3.2 Lagrangian Structure Functions and Autocorrelation Functions 68
4.3.3 Corrected Lagrangian Structure Functions and Autocorrelation Functions . . 69
4.3.4 Horizontal Eddy Diffusivity and the Lagrangian Integral Time 70
4.3.5 Computational Details 71
4.4 Results 72
4.4.1 Probability and Travel Time Maps 72
4.4.2 Lagrangian Autocorrelation Functions 73
4.4.3 Lagrangian Integral Time 75
4.4.4 Absolute Eddy Diffusivity 76
4.5 Discussion and Conclusions 78
4.6 Acknowledgments 78

5 Conclusions **79**
5.1 Summary 79
5.2 Implications and Future Work 81

List of Tables

3.1 Data Windows 48

List of Figures

1.1 Cyanobacterial bloom patterns at different spatial scales in the Baltic Sea, captured on August 11 2015 by the Operational Land Imager (OLI) on Landsat 8. Translucent areas in the top image indicate the extent of the bottom panels. At the highest zoom level (bottom right), a ferry can be discerned that passed through the bloom and caused vertical mixing along its track. Source: NASA Earth Observatory. Figure and caption from Grötsch (2018). 2

1.2 Depiction of Richardson's cascade idea paired with some of Kolmogorov's hypotheses. Energy is injected from the large scale flow at rate ϵ into large eddies at the integral length scale. The large eddies break up into smaller eddies, which break up into even smaller eddies, and so on until they are small enough to be effectively dissipated by viscosity at rate ϵ. As they do break up into smaller and smaller eddies, energy is carried to smaller scales also at rate ϵ. At scales above the integral scale separating the inertial range from the energy containing range, flow statistics depend on how the turbulence was generated. At scales below the integral length scale, the flow statistics are universal (but scale-dependent). 7

1.3 Depiction of an ideal 3D cascade in stationary, homogeneous, isotropic turbulence based on the ideas of Richardson, Kolmogorov, Onsager, and others. Similar to Figure 1.2 in concept, the additional assumptions of Kolmogorov permit scaling laws in terms of ϵ and κ to be formed, resulting in a slope of $-5/3$ on a log-log plot in the inertial range. 8

2.1 (a) Deployment patterns and launch locations for the gridded (blue) and cluster (black) surface drifter releases. For each location (East and West insets) an S-shape and Clover pattern was implemented to reproduce those of the GLAD (S-Shape) and LASER (Clover shape) experiments. S-shape patterns contain 90 drifters each, Clover patterns contain 300 drifters each, and the gridded release contains 28870 drifters. (b) Cluster trajectories for the entire 3 month period. Note the outline of the model domain is plotted in green. 23

2.2 The gridded semi-Lagrangian and Eulierian second order longitudinal (D_L^2) and transverse (D_T^2) velocity structure functions. All structure functions here are calculated by using means, in contrast to the medians used in the WRST. Structure functions found at each time step are bootstrapped with 10,000 resamples to obtain 95% confidence intervals, as noted by shading around them. A guideline of slope 1 and 2/3 is provided. 32

2.3 The second order structure functions of (a) longitudinal D_L^2 and (b) transverse D_T^2 velocities, and (c) the third order structure function of longitudinal velocity D_L^3. All structure functions here are calculated by using means, in contrast to the medians used in the WRST. The Eulerian structure functions found at each time step are bootstrapped with 10,000 resamples to obtain 95% confidence intervals, as noted by shading around them in (a) and (b). The dashed and dotted lines represent semi-Lagrangian structure functions with different deployment locations, and differences between lines with the same line-style represent varying deployment patterns. The deviations due to differing deployment patterns are typically small or under-resolved with our model resolution. Guidelines with slopes of 2,1,and 2/3 are provided by the solid brown lines for reference. Only the absolute values of negative data points are plotted here. Note that LASER P1 and one of the summer eastern trajectories only had one negative value in this range at the smallest bin, and are not plotted. A guideline of slope 1 and 2/3 is provided. 33

2.4 Medians of ESF2s and LSF2s in winter. The interquartile range is represented by shading. Circles represent rejection of the null hypothesis that the two datasets have equal medians. Stars represent acceptance of this hypothesis with a corresponding p-value of greater than 0.05. 36

2.5 The second order structure functions of (a) divergent D_D^2, and (b) rotational D_R^2 motions. Eulerian structure functions are calculated by decomposing the velocity field directly. The semi-Lagrangian cluster release structure functions are calculated from the longitudinal and transverse structure functions following Lindborg (2015). Note that for (a) the semi-Lagrangian divergence structure functions are faded gray, as they were all negative, but have been reproduced as positive values on this plot to make clear their magnitude is similar to that of other positive structure functions. . 37

2.6 Second order structure functions from the cluster releases of (a) divergence, and (b) curl calculated using means. Bootstrapped 95% confidence intervals for the Eulerian statistics from 10,000 resamples are denoted by shading. 39

3.1 **(a)** Trajectories for the P1 **(green)**, P2 & P3 **(pink)** and LDA **(orange)** drifter deployments. The shiptrack X-band radar footprint is shown in black. To ensure the best overlap between the two datasets, the drifters and X-band measurements were analyzed only in the indicated domains and the time-frames shown in Table 1. **(b)** – **(d)** Scaled divergence δ/f from X-band radar for the time-frames and domains for **(b)** P1, **(c)** P2 & P3, and **(d)** LDA. 45

3.2 Demonstration of the relationship between the first-order structure function and drifters subject to **(a)** convergent flow, **(b)** divergent flow, **(c)** counterclockwise rotation, and **(d)** clockwise rotation. When subtracting the variables of the second drifter from the first (an arbitrary choice), the sign of the first-order structure function is determined. The signs of the differences that go into forming the $S_L^1 = \langle \Delta u_x \Delta x + \Delta u_y \Delta y \rangle$ and $S_T^1 = -\Delta u_x \Delta y + \Delta u_y \Delta x$ are provided. 50

3.3 The **(top row)** first-order and **(middle row)** second-order longitudinal *(solid)* and transverse *(dashed)* velocity structure functions, and **(bottom row)** the absolute values of negative *(circle)* and positive *(plus)* third-order longitudinal velocity structure function values for the P1 *(left)*, P2 & P3 *(middle)*, and LDA *(right)* launches. The drifter deployments are given by the colored lines and symbols and the corresponding Eulerian X-band radar data by the black lines and symbols. Bootstrapped 95% bias corrected and accelerated confidence intervals for the time mean of the first- and second-order structure functions are provided as shading around each line. Dashed gray guidelines through zero are shown in the upper panels. Dashed gray guidelines for the middle panels correspond to theoretical second-order structure function slopes in 3D (2/3) and frontogenesis or an internal gravity wave field (1). A guideline of slope 1 is also shown for the lower panels for the linear slope of the 3rd order structure function predicted in the energy cascade region of 3D, 2D, or QG turbulence. Notice the difference in the y-axes for the first and third-order structure functions. 52

3.4 The quasi-Lagrangian second-order **(upper row)** and third-order **(lower row)** structure functions (green, pink, and orange) and corrected structure functions (blue) from P1 **(left)**, P2 & P3 **(middle)** and LDA **(right)** drifter data. Confidence intervals and guidelines are the same as in Figure 3.3. 54

3.5 The X-band second-order **(upper row)** and third-order **(lower row)** structure functions (black) and corrected structure functions (blue) in the P1 **(left)**, P2 & P3 **(middle)**, and LDA **(right)** domains. Confidence intervals and guidelines are the same as in Figure 3.3. 55

3.6 Eulerian longitudinal **(a,c)** and transverse **(b,d)** uncorrected second-order structure functions as a function of divergence and scale **(a,b)** and of vorticity and scale **(c,d)**, denoted by the blue to yellow logarithmic colormap. The joint probability density function of divergence and separation distance **(a,b)** and vorticity and separation distance **(c,d)** is shown by contours colored using the black to white colormap. Both divergence and vorticity are scaled by the mean Coriolis parameter in the domain. . 56

3.7 **(a)** The velocity and divergence fields at a front on 31 January 2016 at 12:16:19 UTC. Eulerian velocities are given by black arrows, and the P2 & P3 velocities by the pink arrows. Underlain is the Eulerian divergence field scaled by f. **(b)** Same as (a) but with the scaled vorticity field instead of divergence. P2 & P3 drifter (left) and corresponding X-band (right) **(c, d)** first-order, **(e, f)** second-order, and **(g, h)** third-order structure functions. The corrected second- and third-order structure functions are given by the blue markers in **(e)**–**(h)**. Negative and positive values for the third-order structure functions are plotted with dots and pluses, respectively. The 95% bias corrected and accelerated confidence intervals are shown with shading. Note that these confidence intervals are formed from the mean value at a given scale for this particular snapshot. Guidelines are the same as in Figure 3.3. 57

3.8 Same as Figure 3.6 but for data from a vortex on 12 February 2016 at 6:00:59 UTC, using LDA drifters instead of P2 & P3 drifters. 59

3.9 The absolute value of the Eulerian longitudinal *uncorrected* third-order structure function dependent on divergence and scale **(a)** and vorticity and scale **(b)**, denoted by the blue to yellow logarithmic colorbar. Negative values are stippled with a '•' and positive values are left un-stippled. The joint probability density function of divergence and separation distance **(a)** and vorticity and separation distance **(b)** is shown by contours and the black to white linear colorbar. 60

4.1 The GLAD **(top)** and LASER **(bottom)** probability **(left)** and mean travel time **(right)** maps. The colorscale for probability is logarithmic and the colorscale for mean travel time is linear. Colorbars are constrained such that the minimum value on the colorbar is the largest minimum value between GLAD and LASER and the minimum value on the colorbar is the smallest maximum value between GLAD and LASER. Note that because GLAD had fewer drifters total, the probability for just one drifter is higher than that for LASER. 73

4.2 Uncorrected **(a,c,e,f)** and corrected **(b,d,g,h)** Lagrangian autocorrelation functions in the zonal **(a,b,e,f)** and meridional **(c,d,g,h)** directions of GLAD **(upper)** and LASER **(lower)** drifters. Analysis is for 15 day long non-overlapping trajectory segments, and bins that have less then 10% of the maximum number of values in any bin for individual drifter estimates are removed. 74

4.3 Uncorrected **(a,c,e,f)** and corrected **(b,d,g,h)** Lagrangian integral time in the zonal **(a,b,e,f)** and meridional **(c,d,g,h)** directions of GLAD **(upper)** and LASER **(lower)** drifters. Analysis is for 15 (12) day long non-overlapping trajectory segments GLAD (LASER). The colorbars are capped to 2 days for the uncorrected estimates and 10 days for the corrected estimates. The maximum values for GLAD rounded to the nearest 0.1 day are $LIT_u = 1.5$; $LIT'_u = 10.5$; $LIT_v = 2$; $LIT'_v = 8.9$. The maximum values for LASER are $LIT_u = 1.8$; $LIT'_u = 9.4$; $LIT_v = 1.6$; $LIT'_v = 11.7$. 75

4.4 Uncorrected **(a,c,e,f)** and corrected **(b,d,g,h)** absolute eddy diffusivity in the zonal **(a,b,e,f)** and meridional **(c,d,g,h)** directions of GLAD **(upper)** and LASER **(lower)** drifters. Analysis is for 15 day long non-overlapping trajectory segments. The colorbars are capped to $1 \times 10^4 m^2/s$ for the uncorrected estimates and $0times10^4 m^2/s$ for the corrected estimates. The maximum values rounded to the nearest $0.1 \times 10^4 m^2/s$ for GLAD are $ED_u = 2.9$; $ED'_u = 17.8$; $ED_v = 2.3$; $ED'_v = 15.0$. The maximum values rounded to the nearest $0.1 \times 10^4 m^2/s$ for LASER are $ED_u = 1.7$; $ED'_u = 23.3$; $ED_v = 4.3$; $ED'_v = 19.2$. 77

Chapter 1

Introduction

1.1 Motivation

1.1.1 Ocean Turbulence

The ocean is highly turbulent. This is illustrated in Figure 1.1, where cyanobacteria in the upper ocean highlight the irregular motion that varies across a rich array of space and time scales. In 1922 Lewis Fry Richardson eloquently articulated turbulence in the context of weather forecasting as

Big whorls have little whorls that feed on their velocity,
and little whorls have lesser whorls and so on to viscosity.

This simple limerick illustrates a phenomena that is challenging to describe precisely, even though turbulence is ubiquitous in a number of fields. The physical attributes of turbulence are illustrated through its many observed forms – from storms in the atmosphere, to foam lines in lakes and oceans, wakes behind boats, and stirred milk in coffee. Turbulence is responsible for the transfer of enstrophy (the squared vorticity), energy, and tracer variance across scales. Stirring by turbulence also makes mixing properties such as temperature more efficient. Despite much progress in the field over the last decades, a complete understanding of *geophysical turbulence* – where planetary rotation and stratification are present – is still lacking. In particular, while the large ($>$ 10km, many days to months) and small ($<$ 0.1km, minutes to hours) turbulent motions of the ocean are comparatively well described (Kolmogorov, 1941b; Kraichnan, 1967; Charney, 1971; Kunze, 2019), only recently has the intermediate range of scales ($0.1-10km$, hours to a few days), termed *submesoscales*, become a focus of scientific study (see for example the overviews McWilliams, 2016, 2019).

1.1.2 Submesoscale Dynamics

The submesocale range of motion plays a large role in altering the state of the upper ocean by providing pathways to energy dissipation (Molemaker et al., 2005; McWilliams, 2008; D'Asaro et al.,

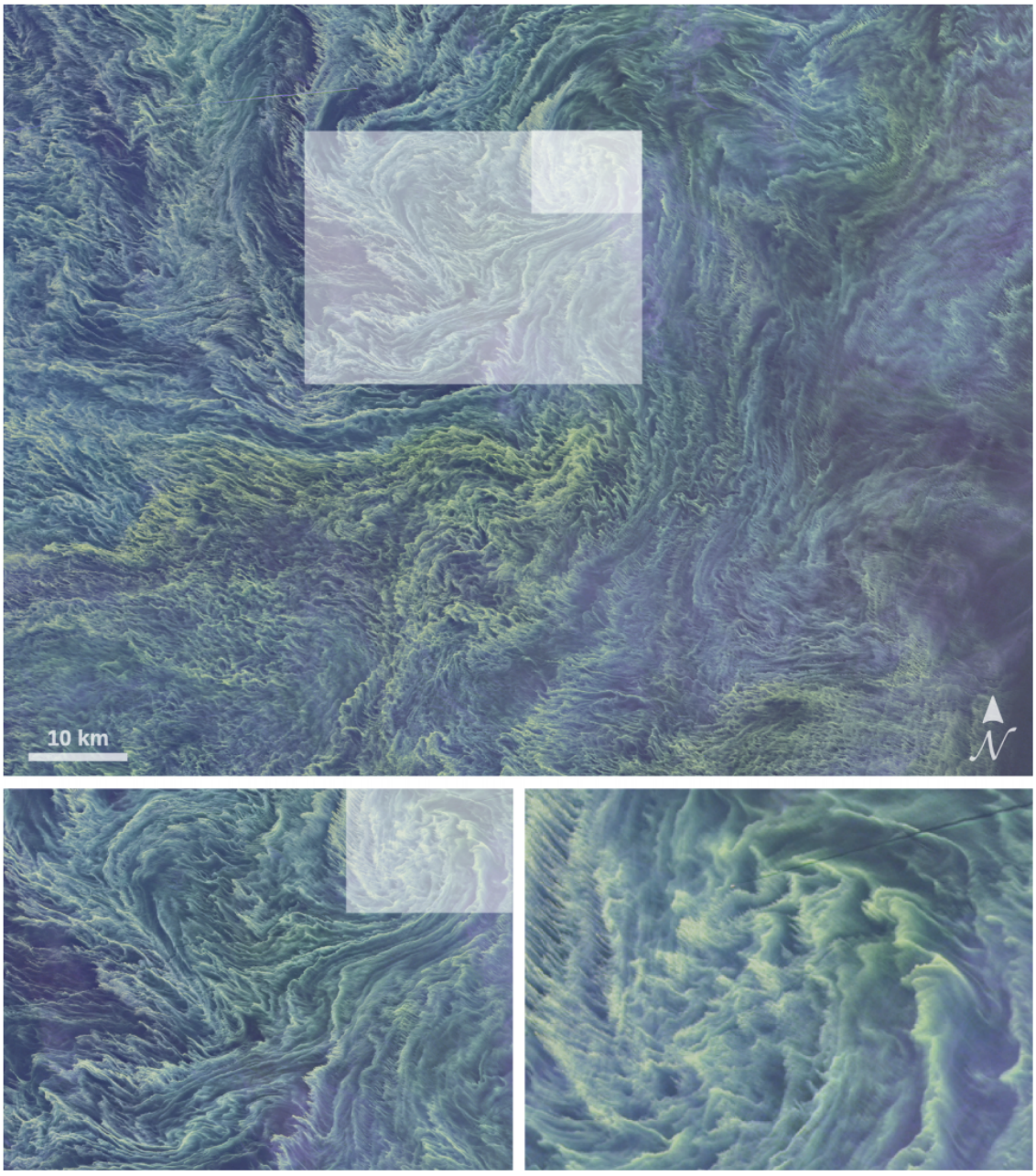

Figure 1.1: Cyanobacterial bloom patterns at different spatial scales in the Baltic Sea, captured on August 11 2015 by the Operational Land Imager (OLI) on Landsat 8. Translucent areas in the top image indicate the extent of the bottom panels. At the highest zoom level (bottom right), a ferry can be discerned that passed through the bloom and caused vertical mixing along its track. Source: NASA Earth Observatory. Figure and caption from Grötsch (2018).

2011; Poje et al., 2017), altering sea-ice distributions (Manucharyan and Thompson, 2017), and affecting both the horizontal distribution and vertical transport of pollutants, heat, freshwater, and

nutrients within and across the mixed layer (Mahadevan and Tandon, 2006; Klein and Lapeyre, 2009; Zhong et al., 2012; Li et al., 2012; Zhong and Bracco, 2013; Poje et al., 2014; Rosso et al., 2014; Omand et al., 2015; Özgökmen et al., 2016; Smith et al., 2016; Mahadevan et al., 2016; Lévy et al., 2018; Siegelman et al., 2019). In particular, on April 20, 2010 the oil rig Deepwater Horizon exploded near DeSoto Canyon in the Northern Gulf of Mexico (GoM). This catastrophic event released an unprecedented amount of oil and gas over the course of about 3 months (Crone and Tolstoy, 2010), resulting in 11 human deaths and countless environmental impacts (e.g. Hayworth et al., 2011; White et al., 2012; Passow et al., 2012). Response and recovery efforts by both the academic communities and government agencies were immediate. In concert with skimming, burning, and releasing dispersants, an ensemble of forecast models with horizontal resolution at or above $\sim$ 4km were ran with particle tracking schemes to provide estimates of the oil dispersal over time. While these models aided mitigation strategies, there were clear shortcomings, including inaccurate representation of ocean circulation at subgrid scales (Liu et al., 2011) and the effects of topography on near-shore transport (e.g. Restrepo et al., 2014). Additionally, satellite imagery during the spill revealed a rich array of submesoscale processes expressed in oil patterns at the sea surface (e.g. Poje et al., 2014), highlighting the importance of processes at scales $<$ 10km. **This dissertation focuses on the submesoscale range of motion in the Northern GoM near the initial location of the Deepwater Horizon Oil Spill – isolating how fluid parcels interact with submesoscale features, characterizing the turbulence statistics that emerge from those interactions, and providing a framework for future forecast model improvement and tests of model fidelity.**

1.1.3 Measuring Ocean Turbulence with Surface Drifters

Material transport is naturally investigated by following fluid parcels in a Lagrangian framework (Bennett et al., 2006; LaCasce, 2008; Van Sebille et al., 2018), in contrast to the fixed-space Eulerian approach implemented in many ocean models (e.g. Griffies and Adcroft, 2008). After the Deepwater Horizon Oil Spill, several campaigns to release surface drifters were conducted near DeSoto Canyon, including the Grand LAgrangian Deployment (GLAD) during summer 2012 (Poje et al., 2014) and the LArangian Submesoscale ExpeRment (LASER) during winter 2016 (D'Asaro et al., 2018). Using these surface drifters to interpret upper ocean pathways is advantageous, as drifter trajectories contain information about instantaneous ocean properties at a given time and spatial location, as well as the history of a water parcel along its trajectory.

Surface drifters have demonstrated ability to follow submesoscale currents and features (e.g. Novelli et al., 2017), unlike many other observational platforms such as moored buoys and coarse resolution satellites. Oil is typically less dense than seawater (Wang et al., 2003), and depending on the sea-state and composition much of it resides at the sea-surface in the form of micron to centimeter thin slicks and films that can span hundreds of kilometers (Daling et al., 2003). The range of scales governing oil dispersion and transport are thus many, which makes numerical representations difficult. Observations are more practicable, via the direct release of oil (Faksness et al.,

2016), or through the less detrimental release of surface drifters as substitutes for oil (Fingas, 2011; Novelli et al., 2018), which can aid in model evaluation and improvement (Reed et al., 1994, 1999; Jones et al., 2016; Spaulding, 2017). There are a few distinctions between oil and drifter proxies. For instance, surface drifters do not mimick effects such as biodegradation of oil by bacteria and sunlight (e.g. Bacosa et al., 2015). Additonally under conditions of strong wind-wave induced vertical shear drogued drifters (i.e. drifters with a sea-sail) were found to exhibit different behavior than oil, undrogued drifters (no sea-sail), or driftcards (bamboo plates) in laboratory experiments and in drifter releases in the Gulf of Mexico (Haza et al., 2018; Novelli et al., 2020). Despite these limitations, drifters still offer invaluable insight into upper ocean processes across a range of scales currently unresolved or not captured by most other observational platforms and numerical models (e.g. Poje et al., 2014; Mariano et al., 2016; Beron-Vera and LaCasce, 2016; Balwada et al., 2016; Poje et al., 2017; D'Asaro et al., 2018; Novelli et al., 2020).

1.1.4 Upper Ocean Energetics

With the onset of a multitude of submesoscale tracking drifter releases in the GoM, interest has grown in understanding upper ocean turbulence in this region through the lens of surface drifters (e.g Balwada et al., 2016; LaCasce, 2016; Poje et al., 2017). One of the key ways turbulence is classified is through its Eulerian kinetic energy spectrum, which is the distribution of turbulent kinetic energy per unit mass across wavenumbers. While there are many studies devoted to understanding the energy spectrum of the atmosphere (e.g. Nastrom et al., 1984; Tulloch and Smith, 2006; Lindborg, 2006; Callies et al., 2014), the energy spectrum of the ocean is more challenging to examine due to smaller length and time scales. On top of these obstacles, surface submesoscale features are an added difficulty due to the the complex dynamics of the mixed layer as well as their relatively small size and ephemeral nature (Thomas et al., 2008). Indeed, the behavior of the energy spectrum across the submesoscale range is still an open question with results suggesting a strong dependence on time and space (e.g. Timmermans and Winsor, 2013; Callies et al., 2015; Rocha et al., 2016a,b; Qiu et al., 2017; Cao et al., 2019; Chereskin et al., 2019).

Analysis of GLAD drifters reveals that they poorly estimate the Eulerian kinetic energy spectrum of the Northern Gulf of Mexico (LaCasce, 2016). However, characterizing turbulent behavior with drifters by calculating the real space counterpart to spectra, structure functions, is considered more reliable, despite also having shortcomings (LaCasce, 2016). The *nth*-order *Eulerian velocity structure function* is given as $S^n_\gamma(r) = \langle \Delta u^n_\gamma \rangle$, where Δu is the difference of the γ velocity component between two points separated by r, and $\langle ... \rangle$ is an ensemble average (see Section 1.3.1 for more details). The slope and magnitude of the second-order structure function offers information about the slope and magnitude of the kinetic energy spectrum (Kraichnan, 1967, 1971; Charney, 1971; Bennett, 1984; Babiano et al., 1985; Callies and Ferrari, 2013), and the sign and magnitude of third-order structure function offers information about the direction (i.e. from large to small wavenumber or vice versa) energy or enstrophy is transferred and the average rate at which this

transfer occurs (Kolmogorov, 1941b; Lindborg, 1999, 2007). Recent analysis of GLAD-derived Eulerian structure functions indicates shallower second order structure-functions, as well as larger and negative third-order structure functions than expected (Poje et al., 2017). Other studies using the same or similar datasets also highlight that drifter motion in this region is strongly dependent on divergence and vorticity fields (e.g. D'Asaro et al., 2018; Chang et al., 2019).

The bulk of this thesis is devoted to connecting these two findings by isolating how convergence zones and vortices create shallower second-order and larger third-order drifter-derived Eulerian structure functions than the statistics calculated from the Eulerian velocity field itself. The remaining chapter is devoted to using the knowledge gained from the biases identified in the previous two chapters alongside other Lagrangian statistics to understand where, when, and what properties both the GLAD and LASER drifters sampled.

1.2 Phenomenology

1.2.1 Statistical Models of Turbulence: K41 Theory

In fluid dynamics a turbulent flow is characterized by its Reynolds number (Reynolds, 1883). The Reynolds number is the dimensionless ratio of the non-linear advective (inertial) terms in the equations of motion to the kinematic viscosity

$$Re = \frac{UL}{\nu} \tag{1.1}$$

where U, L, and ν are characteristic velocity, length scale, and molecular kinematic viscosity of the prescribed flow. High Re numbers imply more turbulent flows, low Re numbers indicate more laminar and smooth flows, and $Re \gg \mathcal{O}(10^4)$ is the boundary for laminar flows to become turbulent (Reynolds, 1883). The ocean typically exceeds this requirement (Thorpe, 2007), and is thus taken to be highly turbulent everywhere. To isolate the turbulent component of the velocity field a *Reynolds' decomposition* is imposed assuming that there is a meaningful distinction between the background flow and the turbulent fluctuations about it. This decomposition dictates that $\mathbf{u} = \langle \mathbf{u} \rangle + \mathbf{u}'$, where $\langle \mathbf{u} \rangle$ is the background velocity, $\mathbf{u}'$ is the turbulent perturbation, and $\langle . \rangle$ is either a space, time, or ensemble average. With this decomposition at hand, the turbulent kinetic energy is defined as $TKE = \frac{1}{2}\langle \mathbf{u}'^2 \rangle$, and its budget and path from input to dissipation can be tracked.

The general ocean circulation is sustained by substantial inputs of energy. This energy comes from injections of momentum, heat, and freshwater, and, for a steady state ocean, this energy must be dissipated. To accomplish this, energy is fed from the large-scale circulation into the largest eddies of length L at rate ϵ. As noted above, in high Reynolds number flows viscous forces are small with respect to inertial forces, and smaller scale motion must necessarily be generated until a small enough scale is created that viscosity can act. Thus these large eddies are assumed to be unstable, and break up into smaller (littler) eddies, which in turn break up into smaller eddies,

and so on. This process continues until the small eddies associated with sharp velocity gradients are small enough that viscosity can efficiently transform the mechanical energy into heat at rate ϵ. During the break up, energy dissipation is much smaller than the transfer from scale to scale (in the inertial range), which is then also transferred at effectively rate ϵ. A depiction of this process is presented in Figure 1.2.

This 'cascading' or 'spectral flux' of energy from large to small scales reflects the ideas proposed by Richardson (1922, 1926), and is the basis for the pioneering work of Kolmogorov (1941b) dedicated to formalizing three dimensional (3D), stationary, homogeneous, isotropic turbulence termed "K41 Theory". Here *stationary* means that the statistics of turbulence are invariant to translations in time. *Homogeneous* means they are invariant to translations in space, and consequently only relative, not absolute coordinate systems are relevant. Finally, *isotropic* means the statistics are invariant to rotations, and thus have no directional dependence. A note that these assumptions imply there are no boundaries or the turbulence studied is far from them. Thus the Reynolds' number must be calculated with quantities intrinsic to the flow – the statistics of the turbulence itself. The velocity scale is prescribed as the root-mean-square (i.e. standard deviation) of the velocity field. The characteristic length scale L is taken as the integral of the of the velocity autocorrelation function defined in section 1.3.1.

Two other assumptions inherent to this theory are locality of scale and self-similarity (Frisch, 1995). Locality of scale requires that only scales near each other interact – small eddies are only swept around but not influenced by large eddies, however any small or large eddy can interact with those eddies directly below and above it in size. Secondly, self-similarity asserts that eddies break up into area-preserving smaller versions of themselves, and the geometry is therefore invariant under coordinate dilations. Armed with these conditions, in the limit of infinite Reynolds' number Kolmogorov (1941b) proposed three hypotheses describing the cascade process. These are summarized as:

1. **Local Isotropy Hypothesis:** At scales smaller than the integral length and time scale, a turbulent flow far from boundaries is locally isotropic, homogeneous, and stationary.

2. **First Similarity Hypothesis:** At scales much smaller than the integral length scale and time scale, the statistics of a turbulent flow have a universal form (i.e. are similar for any turbulent flow). Within this "dissipation range", the statistics only depend on the mean energy dissipation rate (ϵ) and the viscosity (ν).

3. **Second Similarity Hypothesis:** At scales smaller than the integral length and time scale, but larger than the dissipation length and time scale, the statistics of a turbulent flow are also universal. Within this "inertial range" the statistics only depend on ϵ and the local wavenumber κ (or scale r).

Figure 1.3 illustrates an ideal picture of an energy cascade in 3D turbulence under the assumptions that the ocean is steadily stirred by a homogeneous and isotropic force at large scales, and that

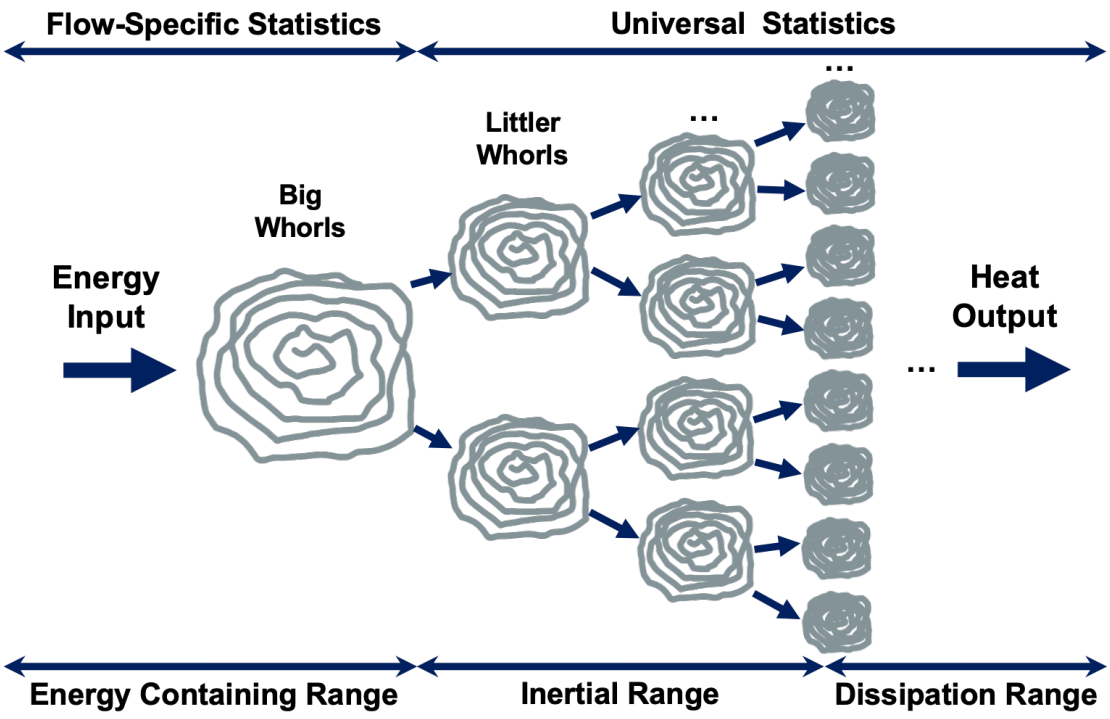

Figure 1.2: Depiction of Richardson's cascade idea paired with some of Kolmogorov's hypotheses. Energy is injected from the large scale flow at rate ϵ into large eddies at the integral length scale. The large eddies break up into smaller eddies, which break up into even smaller eddies, and so on until they are small enough to be effectively dissipated by viscosity at rate ϵ. As they do break up into smaller and smaller eddies, energy is carried to smaller scales also at rate ϵ. At scales above the integral scale separating the inertial range from the energy containing range, flow statistics depend on how the turbulence was generated. At scales below the integral length scale, the flow statistics are universal (but scale-dependent).

the turbulence is statistically stationary (i.e. the forcing and viscous dissipation have come into equilibrium). The theoretical turbulent kinetic energy spectra shown here is broken up into several ranges (bands) of wavenumbers satisfying different properties described in Kolmogorov's hypotheses outlined above. The *inertial range* is the band of wavenumbers over which energy is inviscidly transferred at a constant rate from large scales to smaller scales (small wavenumbers to larger wavenumbers). The inertial range is bounded above by the *integral scale* (wavenumber κ_I, length scale L), which is where energy is injected into the system, and bounded below by the *dissipation scale* (wavenumber κ_η, scale η), where viscous effects become non-negligible. The spectral distance between these two scales is set by the Re number of the integral scale. : $\kappa_I/\kappa_D \propto Re_{\kappa_I}^{3/4}$ (Pope, 2000). Because the ocean is so turbulent, this results in an inertial range of around 8-9 orders of magnitude (Baumert et al., 2005; D'Asaro et al., 2011).

Isotropic tensor analysis combined with Kolmogorov's hypotheses and dimensional analysis yields

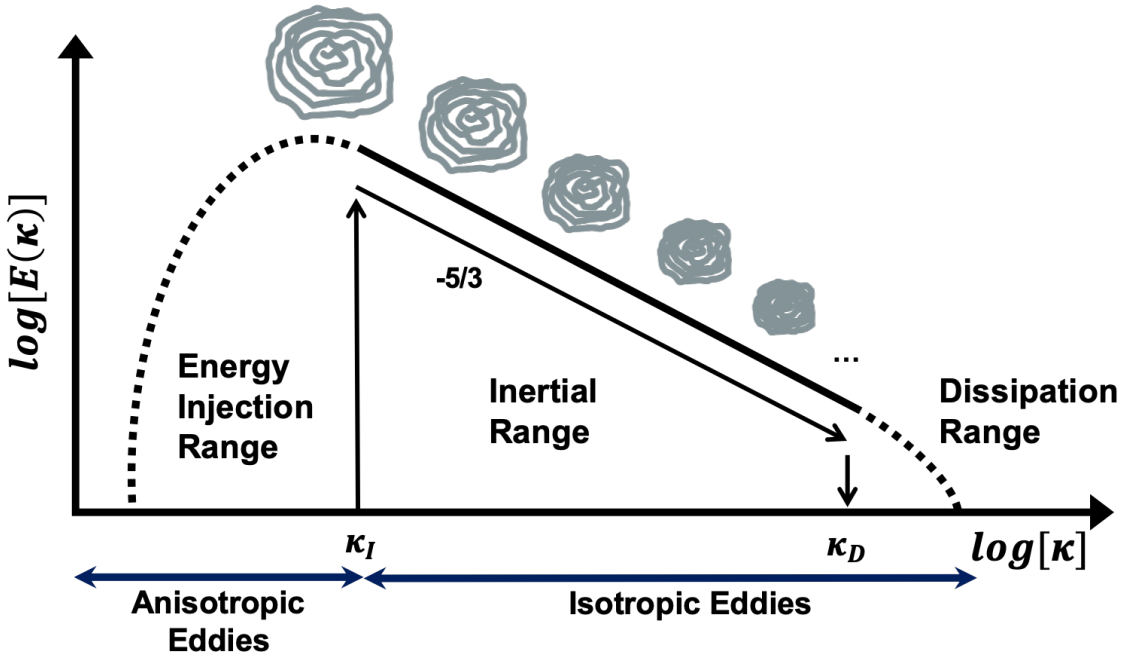

Figure 1.3: Depiction of an ideal 3D cascade in stationary, homogeneous, isotropic turbulence based on the ideas of Richardson, Kolmogorov, Onsager, and others. Similar to Figure 1.2 in concept, the additional assumptions of Kolmogorov permit scaling laws in terms of ϵ and κ to be formed, resulting in a slope of $-5/3$ on a log-log plot in the inertial range.

a predictive model of the cascade processes, whose limits and applications are testable both experimentally and observationally. Kolmogorov (1941b) applied these methods in real space to furnish scaling laws for the Eulerian second-order velocity structure functions, and Onsager (1945) applied similar arguments to arrive at a scaling law in spectral space (Jiménez, 2004; Eyink and Sreenivasan, 2006). If the statistics in the inertial range are determined by the local wavenumber κ with dimensions L^{-1} and ϵ with dimensions $\mathrm{L}^2\mathrm{T}^{-3}$, then the energy spectrum with dimensions $\mathrm{L}^3\mathrm{T}^{-2}$ is given by $E(\kappa) = C_K \epsilon^{2/3} \kappa^{-5/3}$, where C_K is a universal constant found to be near 1.6 (McComb, 1990). On a log-log plot, the energy spectrum therefore has a of slope $-5/3$ in the inertial range. Note that this result is consistent with earlier work by Obukhov (1941) who arrived at the same spectral scaling laws with a different approach (Yaglom, 1994). Under similar arguments the *Lagrangian kinetic energy spectrum*, where velocities are taken along a particle trajectory, should scale as as $L(\omega) = B\epsilon\omega^{-2}$, where ω is the frequency and B is a universal constant (Corrsin, 1963).

1.2.2 Beyond K41: Geophysical Turbulence

While verified in many settings (e.g. Grant et al., 1962; Gibson and Schwarz, 1963; Lumley, 1964), K41 theory is a tremendous simplification of a complex set of processes with inherent shortcomings. For example, one deficiency is the need to include the effects of *intermittency* – the bursty nature of turbulence – which results in skewed spatial and temporal distributions of turbulent statistics, as

demonstrated for ϵ in idealized 3D turbulence (Yaglom, 1966) and ocean mesoscales (Pearson and Fox-Kemper, 2018). For more examples of modifications and extensions of K41 see Frisch (1995).

In *geophysical turbulence*, while the same basic tenets (e.g. conservation of mass, momentum, energy) are still present, the presence of planetary rotation, stratification, and forcing also demand a refined scaling law for the energy spectrum, even if the flow is homogeneous and isotropic in the horizontal dimensions. At the largest scales, the ocean is primarily forced by winds, the equator-to-pole temperature gradient, and the gravitational forces that generate the tides. Other forces from heating/cooling and evaporation/precipitation are smaller, and at small scales the dynamics are three-dimensional, and vertical velocities are strong contributors to mixing (Ferrari and Wunsch, 2009). Between these regimes, the inertial range is populated with mesoscale ($\mathcal{O}(10 - 100$ km, many days)) and submesoscale eddies ($\mathcal{O}(0.1 - 10$ km, hours to a few days)), as well as other features for example inertial and internal-gravity waves. Accordingly, a suite of dynamical theories is needed to describe these spectral subranges. While not every flavor of geophysical turbulence is worked through here, an outline of many are presented and the reader is directed to Callies and Ferrari (2013) for additional review.

The basin-wide general circulation features (e.g. lateral boundary currents) release energy through barotropic and baroclinic instabilities, which manifests primarily as the generation of mesoscale eddies with diameters near the local internal Rossby deformation radius (Salmon, 1978). The *internal Rossby deformation radius* (defined here by the first baroclinic mode as $L = NH/f\pi$, where N is the buoyancy frequency, f is the Coriolis parameter at a prescribed latitude, and H is the depth of the upper ocean) is the distance a parcel of water can travel before being meaningfully affected by Earth's rotation and stratification; for the ocean this is typically 10-200 kilometers depending on the latitude (Cushman-Roisin and Manga, 1995). Mesoscale eddies are important because they play a large role in carrying heat, nutrients, and carbon across the oceans (e.g. Bryan, 1982; Volkov et al., 2008; Chelton et al., 2011; Zhang et al., 2014). The depth of mesoscale eddies compared to their horizontal width is typically small in both the ocean and the atmosphere. For example atmospheric cyclones are confined to the roughly 10km thick troposphere, but they have horizontal extents of 1000s of kilometers. The parameter that describes this is the aspect ratio, λ, given by:

$$\lambda = H/L \ll 1 \tag{1.2}$$

where H is the typical vertical scale and L the typical horizontal scale. Scale analysis of the continuity equation suggests that the vertical velocity, W, scales as $W \sim \lambda U$, and paired with small λ implies that $W \ll U$ and the flow is nearly two-dimensional (2D) (Cushman-Roisin and Manga, 1995). 2D flows have been investigated not only for the potential applications to large-scale meterological and oceanic turbulence, but also the feasibility of numerical simulation as compared to 3D flows.

The mesoscales are also subject to vertical rigidity from strong rotation and stratification. This is quantified by small *Rossby number*, which compares inertial and rotational forces, and small *Froude number*, which compares inertial forces to stratification effects:

$$Ro = \frac{U}{fL} \ll 1, \quad Fr = \frac{U}{NH} \ll 1 \tag{1.3}$$

where U is the characteristic velocity, f is the Coriolis parameter, L is the characteristic horizontal length scale, N is the buoyancy frequency (density stratification), and H is a typical vertical length scale. In the limit of $Ro,\ Fr \to 0$, the flow is termed *quasi-geostrophic* (QG), with dynamics similar to 2D turbulence aside from the retention of a 3D-like vortex stretching term and vorticies confined to isopycnal surfaces (i.e. surfaces of constant potential density) (Charney, 1971). In both 2D and QG turbulence there are two conserved variables that are inviscidly transferred across scales. In 2D flows energy cascades upscale with slope $-5/3$ and *enstrophy* ($\omega^2/2$), that is the squared *vorticity* ($\omega = \nabla \times \mathbf{u}$), cascades downscale as -3 (Kraichnan, 1967, 1971). In QG flows energy still cascades upscale as $-5/3$ but the *potential enstrophy* ($\tilde{q}^2/2$), that is the squared *potential vorticity* ($\tilde{q} = f + \nabla_h^2\psi + \frac{\partial}{\partial z}(\frac{fb}{N^2})$), cascades downscale with slope -3 where f is the Coriolis parameter, $\nabla_h\psi$ is the horizontal gradient of the velocity streamfunction, and b is the buoyancy (Charney, 1971).

At smaller scales, the flow is subject to other forms of turbulence. The gradient Richardson number is defined as

$$Ri = \frac{N^2}{|\frac{d\mathbf{U}}{dz}|^2} \tag{1.4}$$

where $\frac{d\mathbf{U}}{dz}$ the vertical shear of the background horizontal flow, and is a measure of both the stability of the stratification through the sign of N^2, as well as the competition of stratification and mean vertical shear through the magnitude. Shear provides kinetic energy for turbulence, while stable stratification limits turbulent motions. When $Ri < 0$, the stratification is unstable and the flow is conditionally subject to convective turbulence. When the $0 < Ri < 0.25$ the flow is subject to shear instability (Miles, 1961; Howard, 1961). This Kelvin-Helmholtz style instability tends to break up large scale features, as well as create patches of 3D turbulence, leading to a downscale cascade of energy known as *stratified turbulence* (Riley and Lindborg, 2008). From dimensional arguments, among other assumptions, the horizontal wavenumber spectra for stratified turbulence is presumed to scale as $E(\kappa_h) = C_{KE}\epsilon^{2/3}\kappa_h^{-5/3}$ where C_{KE} is a constant for the kinetic energy spectrum distinguished with the subscript 'KE' because there is also a predictable potential energy spectrum (Lindborg, 2005, 2006). While Lindborg (2006) argued that this could be an explanation for the observed mesoscale spectra of the atmosphere, it is also postulated to be the case for scales of 100s of meters in the ocean (e.g. Riley and Lindborg, 2008). Finally, stratification effects become unimportant when the Ozmidov scale, $\kappa_o = (N^2/\epsilon)^{1/2}$, is reached. These are the largest eddies that have enough kinetic energy to overcome stratification and overturn, and thus is the outer scale of 3D turbulence where the scalings of K41 theory of the previous section apply.

At intermediate scales where $Ro, Fr \sim 1$, submesoscale eddies act to churn the upper ocean, and are present alongside gravity waves, fronts, filaments, and tides. These motions contribute to conundrum of bridging the gap between the large-scale anisotropic but balanced mesoscale eddies and the isotropic 3D motion at small scales (e.g. McWilliams et al., 2001; McWilliams, 2003). While

the timescales of submesoscale eddies and near-inertial internal gravity waves often intersect, their motion is distinct because it is assumed that submesoscale motion is largely in balance (Thomas et al., 2008; McWilliams, 2016), and can therefore be described by a scalar field such as potential vorticity or a velocity streamfunction (McKiver and Dritschel, 2008). Further, submesoscale motion is characterized by $\mathcal{O}(1)$ Ro and $\mathcal{O}(1)$ $Ri \sim Fr^{-2}$, distinguishing them from the small and large values of Ro and Fr associated with mesoscale and small scale motion respectively (Thomas et al., 2008; McWilliams, 2016, 2019).

At the ocean surface, a vanishing vertical velocity permits strain at the edges of mesoscale eddies to sharpen horizontal buoyancy gradients (i.e. submesoscale fronts) (Lapeyre et al., 2006). This is unlike the ocean interior, where lack of an air-sea interface allows slumping of fronts, that is the movement of light waters to be above denser waters. Submesoscale fronts and associated eddies are ubiquitous in the upper ocean, and important because they act as conduits for carbon and heat to enter the deep ocean, they bring nutrients to the surface, and they restratify the mixed layer. Analagous to the internal Rossby deformation radius for mesoscale eddies, the deformation radius for submesoscale eddies is found by taking into account the depth and stratification of the mixed layer instead of the depth and stratification of the thermocline. Several classes of models have been developed to describe the dynamics of fronts. When the interior potential vorticity is assumed to be uniform, and motion is driven by buoyancy (or potential temperature) anomalies at the surface, a version of QG called *surface quasi-geostrophy (SQG)* applies (Blumen, 1978; Held et al., 1995). This type of flow is essentially 2D, where surface boundary conditions for buoyancy uniquely determine the fluid motion through an inversion principle. The stirring of surface buoyancy isolines leads to horizontal buoyancy gradients, and straining by a mesoscale eddy field sharpens fronts (e.g. Lapeyre et al., 2006). Secondary instabilities arise at the fronts and lead to a cascade of energy (Held et al., 1995; Juckes, 1995). With constant stratification and an infinitely deep ocean, an energy cascade with slope $-5/3$ is expected (Held et al., 1995). For finite-depth SQG primarily, setting the bottom potential temperature boundary to zero results in spectra this is QG/2D like with slope -3 at large scales and transitions into an SQG like slope of $-5/3$ at smaller scales (Tulloch and Smith, 2006).

While many studies are devoted to applications of surface quasi-geostrophy in the ocean (e.g LaCasce and Mahadevan, 2006; Tulloch and Smith, 2009; Wang et al., 2013; Liu et al., 2014), the restrictions of strong stratificaton and rotation in QG and SQG turbulence ($Ro \sim Fr \ll 1$) exclude ageostrophic motion necessary for submesoscale dynamics, and thus also realistic development of fronto- and filamentogenesis, restratification, and asymmetry between cyclones and anticyclones (Lapeyre et al., 2006; Klein et al., 2008). With weaker stratification ($Ro \sim Fr^2 \ll 1$), *semi-geostrophy (SG)* (Hoskins and Bretherton, 1972) is less restrictive than QG dynamics, and allows for a more realistic generation of surface divergence and vorticity fields. Andrews and Hoskins (1978) predicted that for an isolated 1D front allowed to reach infinite vorticity, the kinetic energy and potential energy would have an energy spectrum with slope $-8/3$. Ageostrophic effects accelerate frontogenesis, and following the development past this singularity to account for the continued steepening of isopycnals a cascade with slope -2 is expected (Boyd, 1992), which is also the slope

given by spectral analysis of submesoscale resolving numerical models (Capet et al., 2008b; Klein et al., 2008). The *surface semi-geostrophy (SSG)* (Badin, 2013) is another model formally similar to SQG in it's boundary conditions that better represents the development of fronts, filaments, and secondary ageostrophic instabilities below the deformation radius, where SG lacks proper vortex dynamics to do so (Malardel et al., 1997). In this regime the spectra are found to be steeper due to the development of more filaments, near $-5/3$ (Ragone and Badin, 2016).

Many mathematical frameworks are in place for different classes of turbulence. However, the ocean is often more complex than the simplifying assumptions underlying the theories proposed above, and observations and models are needed for validation. **This thesis is devoted to aiding interpretations of structure functions (metrics related to the kinetic energy spectrum) through both observations and numerical models, with emphasis on the impacts of submesoscale features.**

1.3 Statistics

1.3.1 Eulerian Structure Functions

While the complexity of turbulence resists an analytic representation (e.g. Carlson et al., 2006), a statistical description is more tractable and offers desirable information about transport and mixing rates. This involves analyzing the moments of velocity differences, that is the *structure functions*. The nth-order Eulerian velocity structure function corresponding to the n^{th}-moment is given as $S^n_\gamma(\mathbf{x},\mathbf{r},t) = \langle[u_\gamma(\mathbf{x}+\mathbf{r},t) - u_\gamma(\mathbf{x},t)]^n\rangle$, where $\langle ...\rangle$ denotes an ensemble average, n is the order of the structure function, γ is the velocity component. Under the assumption of stationarity, the structure function is independent of time (i.e $S^n_\gamma(\mathbf{x},\mathbf{r},t) \equiv S^n_\gamma(\mathbf{x},\mathbf{r})$). Under the assumption of homogeneity the structure function is only dependent on $\mathbf{r}$ (i.e $S^n(\mathbf{x},\mathbf{r}) \equiv S^n(\mathbf{r})$). And finally the assumption of isotropy implies the structure function is only dependent on magnitude of $\mathbf{r}$ (i.e. $S^n(\mathbf{r}) \equiv S^n(r)$). This reduces the previous equation to

$$S^n_\gamma(r) = \langle \Delta u^n_\gamma \rangle \tag{1.5}$$

where the velocity difference is condensed with notation Δu.

It is the significant distortion of eddies that leads to energy transfer across scales (Frisch, 1995). An absolute framework is not capable of detecting this distortion, and therefore a relative framework is employed. To obtain the relative coordinate system, the velocity differences are projected along the line of separation between two points (longitudinal), or projected along the line perpendicular to the direction of separation (transverse). The structure functions corresponding to these directions are denoted by γ values of l and t for longitudinal and transverse respectively, with the projected velocity differences given by

$$\Delta u_l = \hat{\mathbf{k}} \cdot ([\mathbf{u}(\mathbf{x}+\mathbf{r}) - \mathbf{u}(\mathbf{x})] \times \hat{\mathbf{r}})$$
$$\Delta u_t = (\hat{\mathbf{r}} \times \hat{\mathbf{k}}) \cdot (\mathbf{u}(\mathbf{x}+\mathbf{r}) - \mathbf{u}(\mathbf{x})) \tag{1.6}$$

where $\hat{\mathbf{k}}$ is a unit vector in the vertical direction.

Second-Order Structure Functions

Of primary interest to turbulence studies are the second- and third-order structure functions. The second-order structure function, under homogeneity and stationarity, is a linear transformation of the auto-covariance function, defined as $\langle u_\gamma(\mathbf{x}) u_\gamma(\mathbf{x}+\mathbf{r})\rangle$. Specifically,

$$S^2_\gamma(r) = 2[\langle u_\gamma(\mathbf{x})^2\rangle - \langle u_\gamma(\mathbf{x}) u_\gamma(\mathbf{x}+\mathbf{r})\rangle] \tag{1.7}$$

In the limit of no correlation, the structure function levels off to twice the variance, $\langle u_\gamma(\mathbf{x})^2\rangle$. On the other end, when correlation is high, the structure function is relatively small. In-between these two extremes, the structure function is expected to grow with scale, as particles separated by larger and larger distances become less correlated.

Through the auto-covariance function, the second order structure function is also related to the stationary, isotropic, homogenous kinetic energy spectrum by

$$S^2_\gamma(r) = 2\int_0^\infty E_\gamma(\kappa)(1 - J_0(\kappa r) d\kappa \tag{1.8}$$

where $E_\gamma(\kappa)$ is the longitudinal or transverse component of the energy spectrum such that $u^2_\gamma = \int_0^\infty E_\gamma(\kappa) d\kappa$, and $J_0(\kappa r)$) is the zeroth-order Bessel function (Bennett, 1984; LaCasce, 2016). Under the asymptotic limits of $(1 - J_0(\kappa r))$, this is approximated as

$$S^2_\gamma(r) \approx \frac{r^2}{2}\int_0^{2/r} \kappa^2 E_\gamma(\kappa) d\kappa + \int_{2/r}^\infty E_\gamma(\kappa) d\kappa \tag{1.9}$$

which shows that second-order structure function for k corresponding to scale π/r is the sum of the enstrophy of the eddies larger than $\pi r/2$ and the energy from eddies smaller than $\pi r/2$ (Davidson and Pearson, 2005; Balwada et al., 2016). Additionally, structure functions are often preferred over spectra because they can be calculated from a wide array of platforms, and do not depend on even sampling intervals or continuous data-streams in either space or time (e.g. drifters, satellites).

For 3D turbulence, K41 theory suggests that statistics in the inertial range of scales (between the integral and dissipation scales) is solely determined by the local scale r with dimension L and ϵ with dimensions L^2T^{-3}. Thus to be dimensionally homogeneous, the second-order longitudinal structure function with dimensions L^2T^{-2} is given by $S^2_l(r) = C_2\epsilon^{2/3}r^{2/3}$, where C_2 is a universal constant. On a log-log plot, the second-order structure function has a slope of 2/3 in the inertial range. Further, the longitudinal and transverse structure functions in incompressible 3D flows are related by

$$S_t^2(r) = S_l^2(r) + \frac{r}{2}\frac{dS_l^2(r)}{dr} \tag{1.10}$$

(De Karman and Howarth, 1938). Then the scaling for the transverse second-order structure function follows as $S_t^2(r) = \frac{4}{3}C_2\epsilon^{2/3}r^{2/3}$ and thus both longitudinal and transverse structure functions have similar power laws but difference magnitudes. Aside from relationships to energy and enstrophy, these statistics are desirable due to their relationship with the mean dissipation rate per unit mass $\epsilon = 2\nu\langle s_{ij}s_{ij}\rangle$, where s_{ij} is the rate of strain tensor. To measure ϵ requires knowledge of the full velocity gradient tensor, and the structure functions are often a more practicable way to measure this quantity. However, use of this method is precluded without knowledge of the universal constant C_2, which has been experimentally determined as 2.13 ± 0.22 (Sreenivasan, 1995)

In geophysical turbulence, a suite of non-3D dynamics are often relevant. For a self similar kinetic energy spectra defined by $E(\kappa) \sim \kappa^\alpha$ the second order structure function scales as $S(\kappa) \sim \kappa^{-\alpha-1}$ (Bennett, 1984), provided $1 < \alpha < 3$ (Babiano et al., 1985). In two dimensional (2D) and (surface) quasi-geostrophic (QG) flows, in the energy cascade region the second-order structure function scales as $r^{2/3}$. In the (potential) enstrophy cascading range the second order structure function scales as r^2 for (QG) 2D flows. Here the spectra is on the boundary allowed for the transformation of spectra to structure functions, and in this case the second order structure function of vorticity can be more informative (e.g. Kramer et al., 2011). Finally in the presence of strong frontogenesis, the second order structure function scales as r^1 (Capet et al., 2008b).

Helmholtz Decomposition

The ratio of the transverse and longitudinal structure functions are related to the rotation and divergence within in a flow. For two-dimensional non-divergent flow the transverse and londitudinal structure functions are related by $S_t^2(r) = \frac{d}{dr}(rS_l^2(r))$ (Batchelor, 1953; Lindborg, 2007). Structure functions with a power law formulation $S_\gamma^2(r) \sim r^m$ in a purely divergent flow have the ratio $S_t^2/S_l^2 = \frac{1}{m+1}$, and in a purely rotational flow have the ratio $S_t^2/S_l^2 = m+1$ (Lindborg, 1996; Bühler et al., 2014; Balwada et al., 2016). Further, a Helmholtz decomposition is also possible, which isolates the rotational and divergent components of the relative velocity (Bühler et al., 2014; Lindborg, 2015):

$$\begin{aligned} S_d^2(r) &= S_l^2(r) - \textstyle\int_0^r \frac{1}{r}(S_t^2(r) - S_l^2(r))dr \\ S_r^2(r) &= S_t^2(r) + \textstyle\int_0^r \frac{1}{r}(S_t^2(r) - S_l^2(r))dr \end{aligned} \tag{1.11}$$

In two-dimensional or QG flows, the velocity field is expected to be non-divergent, or nearly so, such that the rotational component is dominant (i.e. $S_d^2 << S_r^2$). In the submesoscale range, to include frontogenesis and internal wave dynamics, the divergent component is expected to be as or more important depending on the type of regime.

Third-Order Structure Functions

While second-order statistics are proportional to ϵ, the proportionality constants for all dynamical regimes are not well defined, and because the second-order structure function is positive definite, the direction of energy transfer across scales in the cascade process is lost. To quantify this flux Kolmogorov (1941a) derived the "$4/5^{th}$ law" in which the third-order longitudinal structure function is related to ϵ by

$$S_l^3(r) = -\frac{4}{5}\epsilon r \tag{1.12}$$

through the Karman-Howarth equation for the two-point velocity correlation function (De Karman and Howarth, 1938). The negative sign here indicates a flux toward small scales, termed a *direct cascade*. The benefit of this equation is that it does not rely on unknown proportionality constants or dimensional arguments, and is thus one of the few "exact" laws of turbulence (of course still under the assumptions of stationarity, homogeneity, and isotropy).

For d-dimensional turbulence, a more general law is formulated as (Falkovich et al., 2001):

$$S_l^3(r) = \frac{-12}{d(d+2)}\epsilon r \tag{1.13}$$

Thus for 2D turbulence $S^3(r) = -\frac{3}{2}\epsilon r$ with $\epsilon < 0$ indicating an inverse, upscale cascade. In the enstrophy cascade regime it is found that

$$S_l^3(r) = \frac{1}{8}\epsilon_Z r^3 \tag{1.14}$$

with the enstrophy dissipation rate $\epsilon_Z > 0$ indicating a forward cascade of energy to smaller scales (Lindborg, 1999). Additionally alternate forms have been derived combining information from both the transverse and longitudinal components $\langle \Delta u_l^3 \rangle + \langle \Delta u_l \Delta u_t^2 \rangle = -2\epsilon r$ (Lindborg and Cho, 2001).

1.3.2 Lagrangian Structure Functions and the Autocorrelation Function

Structure functions can also be formulated in a Lagrangian framework by following particle trajectories. It is important to note that while the theory outlined below is for truly Lagrangian particles, the surface drifters utilized throughout this thesis are not truly Lagrangian because they are buoyantly confined to the surface ocean – at regions of subduction, they cease to follow the three-dimensional flow. However, there are many instances for which this type of trajectory is desirable in resembling a particular transport application (e.g. oil, plankton), and surface drifters are taken as proxies for these buoyant tracers. Thus, in the proceeding chapters "Lagrangian" is used interchangeably with "semi-Lagrangian".

The relationships between the Lagrangian kinetic energy spectra are analogous to the sections above regarding Eulerian spectra and structure functions, but in contrast to Eulerian structure

functions, Lagrangian velocity structure functions are the averaged powers of the Cartesian velocity difference between time $t+\tau$ and the time t along a trajectory:

$$S_{L\gamma}^{n}(\mathbf{a},t,\tau) = \langle (u_\gamma(\mathbf{a},t+\tau) - u_\gamma(\mathbf{a},t))^n \rangle \tag{1.15}$$

where the subscript γ is the Cartesian velocity increment along a particle trajectory (either zonal or meridional), $\mathbf{a}$ is the initial particle position (and remains as a particle label for all time, even though at later times it is not directly related to the particle position), t is time, τ is the time lag, n is the order of the structure function, and $\langle \cdot \rangle$ is an average over all differences at a particular lag for a given trajectory, and typically over all particle trajectories as well. As before, several simplifying assumptions are often applied. Statistical stationarity and homogeneity imply the structure functions are independent of translations in space and time. Thus the structure function is only dependent on the time lag τ, and not the absolute time t or initial position $\mathbf{a}$. This reduces Equation 4.3 to $S_{L\gamma}^{n}(\tau) = \langle \Delta u_\gamma^n \rangle$.

Note that as the particle position continues to evolve following the trajectory, the second-order structure function of this variety is *not* related via cosine transform to the power spectrum in time of the velocity at a fixed location. It is however, related in the same manner as Section 1.3.1 to the *Lagrangian* power spectrum, $L(\omega)$, where ω is frequency. If the Lagrangian kinetic energy spectrum is given by $L(\omega) \propto \omega^\alpha$, then $S_L^2(r) \propto r^{-\alpha-1}$ provided both follow a power law (Babiano et al., 1987). In this thesis, the primary concern is not with the Lagrangian frequency spectrum, but it's Fourier transform pair: the temporal autocorrelation function given by

$$R_{L\gamma}(\mathbf{a},t,\tau) = \frac{1}{\sigma_\gamma^2} \big\langle u_\gamma(\mathbf{a},t) u_\gamma(\mathbf{a},t+\tau) \big\rangle \tag{1.16}$$

where σ_γ^2 is the velocity variance of the γ component of velocity. In isotropic, stationary, and homogeneous flows, the autocorrelation function is also only dependent on the time lag τ. Under these assumptions, the temporal autocorrelation function is related to the Lagrangian second-order structure structure function by

$$R_{L\gamma}(\tau) = 1 - \frac{S_{L\gamma}^2(\tau)}{2\sigma_\gamma^2}. \tag{1.17}$$

For short time lags $R_{L\gamma}$ is expected to be close to one, and for long time lags the correlation is expected to go to zero. For more details, please review Babiano et al. (1987).

1.3.3 Eddy Diffusivity and the Lagrangian Integral Time

By assuming the scales of turbulence are very small compared to those of the mean field (Taylor, 1921), the evolution of a conservative tracer field can be represented by an advection-diffusion equation

$$\frac{\partial C}{dt} + \mathbf{U} \cdot \nabla C = -\nabla \cdot \langle \mathbf{u}' c' \rangle \equiv \nabla \cdot (\mathbf{K} \nabla C) \tag{1.18}$$

where $\mathbf{U} = (U, V, W)$ is the mean velocity vector, C is the mean concentration, c' is the fluctuation, $\mathbf{u}' = (u', v', w')$ is the turbulent velocity vector, and $\mathbf{K}$ is the eddy diffusivity tensor that accounts for the unresolved scales of turbulence (e.g. Fox-Kemper et al., 2013; Bachman et al., 2015). It is important to note that when the large scale flow is, for example, heterogeneous or non-stationary, the scale separation hypothesis may not hold such that the averaging procedure does not correctly resolve the mean, and the applicability of the advection-diffusion equation may be questionable (Gage and Nastrom, 1986; Davis, 1987; Zambianchi and Griffa, 1994; Falco et al., 2000; Zang and Wunsch, 2001). Although alternatives are available (Davis, 1987), the advection-diffusion equation is often used because of its utility and ease of implementation (e.g. Griffa, 1996; LaCasce, 2008; Falco et al., 2000) regardless of whether a scale separation is realized.

Equation 4.11 also results from Lagrangian trajectories experiencing random walks (Einstein, 1906, 1956). That is, the advection-diffusion equation is a macroscopic manifestation of molecular Brownian motion. The relationship stems from assuming the individual particle motion is given by the zeroth-order stochastic model

$$d\mathbf{x} = \mathbf{U}dt + \sqrt{2}\boldsymbol{\sigma}d\mathbf{W} \tag{1.19}$$

where $\mathbf{x}$ is the particle position, $\mathbf{U}$ is the background velocity, $\boldsymbol{\sigma}$ is the rms velocity, $d\mathbf{W}$ is the normally distributed random increment of a Weiner process (e.g. Griffa, 1996; Berloff and McWilliams, 2002; Brickman and Smith, 2002). Under this model, the probability of the particle position evolves according to the Fokker-Plank equation

$$\frac{\partial P}{\partial t} + \mathbf{U} \cdot \nabla P = \nabla \cdot (\mathbf{K} \nabla P) \tag{1.20}$$

which evolves exactly as the tracer in Equation 4.11 for appropriate choices of advection and diffusion.

While a useful first approximation due to mathematical simplicity, this model fails to capture some of the physical features of Brownian motion. In particular, this model misses the inertia of particles that recoil after their collisions and gain correlations between successive steps in time, the ballistic motion of particles when collisions are not well separated in time, and the particle interactions themselves that may preclude the use of individual noisy walkers that are independent of each other. To overcome the first two issues, Taylor (1921) used the notion of a "persistent random walk", where for finite times Lagrangian particle velocities are correlated, to develop a relationship between the autocorrelation function and absolute eddy diffusivity in homogeneous and stationary turbulence. This can be generalized to three dimensional, homogeneous, stationary, incompressible turbulence (Batchelor, 1949), however the simplified theory is presented here.

In a Lagrangian framework, the eddy diffusivity is defined as the rate of turbulent absolute (i.e. single-particle) dispersion, and given by the time derivative of the particle displacement covariance in the γ direction,

$$K_\gamma = \frac{1}{2}\frac{d}{dt}\langle (X'_\gamma)^2 \rangle \tag{1.21}$$

where X' is the residual particle displacement. Note here that the *absolute* diffusivity is distinct from the *relative* diffusivity (i.e. the time derivative of the relative (multi-particle) dispersion). Unlike absolute diffusivity, which describes the absolute rate of spreading at large-scales, the relative diffusivity determines the rate of spreading around of a a tracer cloud around it's center of mass Corrsin (1963); LaCasce (2008).

The single-particle dispersion is related to the autocorrelation function via

$$\langle (X'_\gamma)^2 \rangle = 2\sigma_\gamma^2 \int_0^t (t-\tau) R_{L\gamma}(\tau) d\tau. \tag{1.22}$$

Provided the autocorrelation function decreases to zero sufficiently fast as $t \to \infty$, the Lagrangian integral time is defined as

$$T_{L\gamma} = \int_0^\infty R_{L\gamma}(\tau) d\tau \tag{1.23}$$

and describes the memory of a particle along it's trajectory. It is a basic measure of predictability, and utilized in many Lagrangian Stochastic Models to parametrize the the transport and dispersion of scalars subject to a turbulent velocity field (e.g. Griffa, 1996; Haza et al., 2014). The Lagrangian integral time can be used to investigate the asymptotic limits of the absolute dispersion, and therefore the absolute eddy diffusivity. In the limit of short times, $R_{L\gamma}(\tau) \sim 1$ and therefore

$$\langle (X'_\gamma)^2 \rangle \approx 2\sigma_\gamma^2 \int_0^t (t-\tau) d\tau = \sigma_\gamma^2 t^2 \quad t \ll T_{L\gamma} \tag{1.24}$$

This is the initial growth phase, where particles disperse ballistically and the Eulerian field is best represented by a wave equation instead of a diffusion equation. In the limit of long times, the integral of $R_{L\gamma}(\tau)$ approaches $T_{L\gamma}$, and provided the integrals converge

$$\begin{aligned} \langle (X'_\gamma)^2 \rangle &= 2\sigma_\gamma^2 t \int_0^t R_{L\gamma}(\tau) d\tau - 2\sigma_\gamma^2 \int_0^t \tau R_{L\gamma}(\tau) d\tau & (1.25) \\ &\approx 2\sigma_\gamma^2 t T_{L\gamma} \quad t \gg T_{L\gamma} & (1.26) \end{aligned}$$

This is the random walk phases, where dispersion grows linearly in time. This implies that the eddy diffusivity is constant, and the motion is captured by a diffusion equation. Under the same limits, the diffusivity is

$$K_\gamma \approx \begin{cases} \frac{1}{2}\frac{d}{dt}\left[\sigma_\gamma^2 t^2\right] = \sigma_\gamma^2 t & t \ll T_{L\gamma} \\ \\ \frac{1}{2}\frac{d}{dt}\left[2\sigma_\gamma^2 t T_{L\gamma}\right] = \sigma_\gamma^2 T_{L\gamma} & t \gg T_{L\gamma} \end{cases} \tag{1.27}$$

Thus, if the Lagrangian integral time is known as well as the velocity variance, an estimate of the absolute eddy diffusivity can be made. A good review of these properties is given in LaCasce (2008).

1.3.4 Probability and Travel Time Maps

The probability map characterizes the number of trajectories that passed through a given bin (only counted at the first arrival) and the travel time map indicates the mean time at which the trajectories that passed through a bin first arrived there. This provides context for drifter sampling patterns and interpretations for the spatial maps of variables presented in the previous sections. To calculate the probability, the domain is broken up into boxes with lengths $dlon \approx dlat \approx 0.05km$, and the percentage of drifters that visit the i^{th} box is given by

$$P_i = \frac{N_i}{N} \tag{1.28}$$

Where N_i is the number of trajectories that made it to the i^{th} bin at least once in the roughly three month period for each season and N is the total number of trajectories that could have made it to the i^{th} bin over that timeframe. For GLAD, $N = 297$ and for LASER $N = 956$.

The travel time map is constructed such that the average time of arrival of the successful trajectories entering the i^{th} bin is given by

$$\overline{T}_i = \frac{\Sigma T_i}{N_i} \tag{1.29}$$

where the overbar indicates an average and the sum is over all 'first-hit' times T_i for the successful trajectories N_i.

1.4 Outline of Thesis

This thesis utilizes drifter observations and numerical simulations to understand how parcels of water experience and respond to oceanic turbulence. Specifically, how the features over the submesoscale range of motion affect their single- and two-point statistics.

In Chapter 2, numerical simulations of the Northern Gulf of Mexico are paired with Lagrangian particle tracking to understand the impact of convergence zones and vortices on turbulence statistics derived from synthetic surface drifters. Differences between Eulerian and semi-Lagrangian velocity structure functions are explained by correlated divergence and curl structure functions over the submesoscale range of motion.

In Chapter 3, observations are used to corroborate and refine the drifter bias noted in Chapter 2. Velocity structure functions from Eulerian X-band radar measurements and semi-Lagrangian surface drifter measurements are shown to disagree in a way consistent with the results of the previous chapter. Further, in addition to the accumulation bias from oversampling frontal regions and vortices noted in Chapter 2, the differences between Eulerian and surface drifter velocity structure functions are also found to be due to a background bias from non-zero first-order structure functions.

In Chapter 4, Lagrangian structure functions provide estimates of the Lagrangian integral time and eddy diffusivity. These are corrected for mean gradients in the flow, similar to the methods developed in Chapter 3. Spatial maps of both the Lagrangian integral time and absolute eddy

diffusivity are used alongside probability and travel time maps to characterize the transport and dispersion of GLAD and LASER drifters in the Northern Gulf of Mexico.

Finally, Chapter 5 summarizes the main conclusions of this thesis and the implications for using surface drifters to study submesoscale and mesoscale turbulence.

Chapter 2

Identifying the Bias: Systematic Biases in Eulerian Structure Functions Derived from Synthetic Surface Drifters

This chapter was published as Jenna Pearson, Baylor Fox-Kemper, Roy Barkan, Jun Choi, Annalissa Bracco, and James C. McWilliams, 2019: Impacts of Convergence on Structure Functions from Surface Drifters in the Gulf of Mexico. J. Phys. Oceanogr., 49, 675–690, https://doi.org/10.1175/JPO-D-18-0029.1. Recent analysis of GLAD-derived Eulerian structure functions indicate shallower second order structure-functions, as well as larger and negative third-order structure functions than expected (Poje et al., 2017). Other studies using the same or similar datasets also highlight that drifter motion in this region is strongly dependent on divergence and vorticity fields (D'Asaro et al., 2018; Chang et al., 2019). To diagnose the impact of convergence zones and vortices on turbulence statistics derived from synthetic surface drifters, numerical simulations of the Northern Gulf of Mexico are paired with Lagrangian particle tracking. Differences between Eulerian and semi-Lagrangian velocity structure functions are explained by correlated divergence and curl over the submesoscale range of motion. This chapter sets the stage for the analysis in Chapter 3, where Eulerian and drifter statistics are compared with observations to corroborate and refine the analysis presented here. Finally, the benefits of the biases identified in this chapter, as well as Chapter 3, are used alongside other semi-Lagrangian statistics to describe flow features related to convergence and rotation.

Abstract

There are limitations in approximating Eulerian statistics from surface drifters, due to biases from surface convergences. By contrasting second- and third-order Eulerian and surface drifter structure functions obtained from a model of the Gulf of Mexico, the consequences of the semi-Lagrangian nature of observations during the summer Grand LAgrangian Deployment (GLAD) and winter LAgrangian Submesoscale ExpeRiment (LASER) are estimated. By varying launch pattern and location, the robustness and sensitivity of these statistics are evaluated. Over scales less than 10 km, second-order structure functions of surface drifters consistently have shallower slopes ($\sim r^{2/3}$) than Eulerian statistics ($\sim r$), suggesting that surface drifter structure functions differ systematically, and don't reproduce the scalings of the Eulerian fields. Medians of Eulerian and cluster release second-order statistics are also significantly different across all scales. Synthetic cluster release statistics depend on launch location and weakly on launch pattern. The observations suggest little seasonal difference in the second-order statistics, but the LASER third-order structure function shows a sign change around 1 km, while GLAD and the synthetic cluster releases show a third-order structure function sign change around 10 km. Further, synthetic surface drifter cluster releases (and therefore likely the GLAD observations) show robust biases in the negative third-order structure functions, which may lead to significant overestimation of the spectral energy flux and underestimation of the transition scale to a forward energy cascade. The Helmholtz decomposition, and curl and divergence statistics, of Eulerian and cluster releases differ, particularly on scales less than 10 km, in agreement with observations of drifters preferentially sampling convergences in coherent structures.

2.1 Introduction

The global expanse of the ocean paired with seawater's small viscosity permits motion over a wide range of scales. The submesoscale range ($\mathcal{O}$(0.1-10 km, hours to days) has important effects on upper ocean dynamics (Thomas et al., 2008; Boccaletti et al., 2007; Klein et al., 2011; Fox-Kemper et al., 2011; McWilliams, 2016). The Gulf of Mexico (GoM) is a unique example of these dynamics, due to the rich array of submesoscale features seen in ocean color, its coastal geometry, and interactions between the Mississippi River plume and large eddies. Specifically, significant submesoscale activity is present near De Soto Canyon (Schiller et al., 2011), as revealed by two recent experiments using large numbers of semi-Lagrangian surface drifters along with other instruments (Poje et al., 2014; Haza et al., 2018; D'Asaro et al., 2018).

Surface drifters are one of the most promising technologies to resolve submesoscale flow characteristics well below the deformation radius of 10-50 km in the GoM (Chelton et al., 1998; Carrier et al., 2014a). Gridded satellite products and shiptrack data are too coarse to resolve submesoscale activity in this region (McWilliams, 2016). High-resolution models have been the prime exploratory tool of these scales (Luo et al., 2016; Barkan et al., 2017a,b; Choi et al., 2017), to include those utilizing data-assimilation (Carrier et al., 2014b), but direct observational evaluation of the statistics of submesoscale phenomena are more challenging to obtain and analyze. Their utility has led to

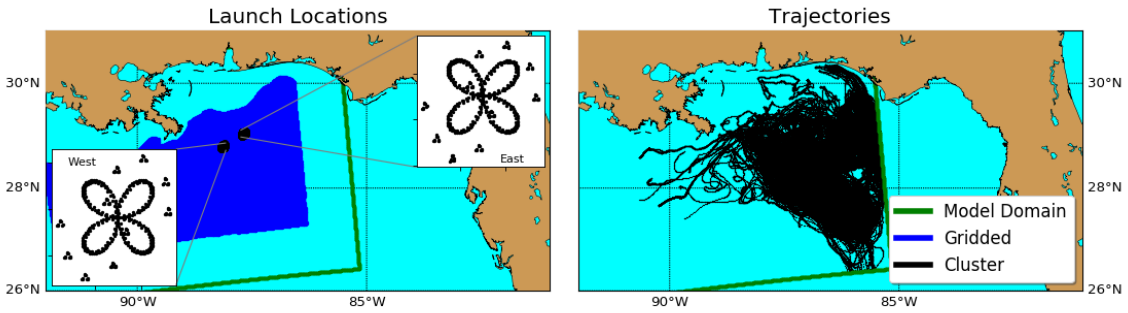

Figure 2.1: (a) Deployment patterns and launch locations for the gridded (blue) and cluster (black) surface drifter releases. For each location (East and West insets) an S-shape and Clover pattern was implemented to reproduce those of the GLAD (S-Shape) and LASER (Clover shape) experiments. S-shape patterns contain 90 drifters each, Clover patterns contain 300 drifters each, and the gridded release contains 28870 drifters. (b) Cluster trajectories for the entire 3 month period. Note the outline of the model domain is plotted in green.

several releases of surface drifters throughout the GoM in the last decades, from which previous work has made estimations of velocity statistics–sometimes without distinguishing between Eulerian and semi-Lagrangian sampling in interpretation–in the submesoscale range (Poje et al., 2014; Beron-Vera and LaCasce, 2016; Mariano et al., 2016; Balwada et al., 2016; Sansón et al., 2017). We revisit some of the conclusions made in those papers by exploiting releases of simulated surface drifters (Choi et al., 2017) mimicking the design of the Grand LAgrangian Deployment [GLAD, (Poje et al., 2014)] and LAgrangian Submesoscale ExpeRiment [LASER, (D'Asaro et al., 2018)].

While drifter data is crucial for obtaining information at the submesoscale, care must be taken when interpreting statistics derived from semi-Lagrangian datasets. Buoyant drifters are confined near the surface, and as they traverse the velocity field following water parcels in the horizontal, they often remain trapped in convergent zones such as fronts or windrows, or in long-lived eddies (D'Asaro et al., 2018; Barkan et al., 2017b; Choi et al., 2017). Surface drifters are therefore not capable of sampling the 3D, divergenceless velocity field (i.e. vertical motions). Specifically, the drifters in the studies identified here (GLAD, LASER) were drogued at $\mathcal{O}(0.5m)$ and moved under the influence of the currents at this depth. If the tendency of surface drifters to remain in convergent features is stronger than the tendency for wind slippage or other dynamics to break up the convergences, there is potential for biased statistics from surface drifter data versus Eulerian field statistics. Motivated by the probability density function (PDF) analysis of Choi et al. (2017), which showed that semi-Lagrangian data produces biased probability density functions in both divergence and vorticity, *the primary objectives of this paper are to examine the ability of semi-Lagrangian data to reproduce Eulerian velocity structure functions, and to better understand differences by examining curl and divergence structure functions.* The use of curl and divergence structure functions, in place of the PDF methods mentioned earlier, is advantageous because it is scale-selective. That is, both structure

functions and PDFs are capable of detecting differences between Eulerian and semi-Lagrangian estimates of the same object, but of the two methods only the structure function is capable of sorting these differences by scale.

The two Gulf of Mexico (GoM) cluster release considered in this work differ in the season they were conducted (GLAD in summer, LASER in winter) and in the deployment pattern used. Both modeling studies (Mensa et al., 2013; Brannigan et al., 2015) and observational studies (Callies et al., 2015; Buckingham et al., 2016) have focused on the seasonality of the submesoscale, and generally agree that there is stronger submesoscale activity in winter. The submesoscale, when dynamically defined (Thomas et al., 2008; Boccaletti et al., 2007), varies considerably in scale from summer to winter as the ocean mixed layer depth varies, and tends to be larger/stronger the deeper the mixed layer. One major consequence is that models with fixed resolution across seasons, including those used here, likely overestimate the degree of seasonality because summer submesoscale circulations are more difficult to resolve (Barkan et al., 2017b).

In the GoM river outflow induces strong lateral buoyancy gradients and shallow mixed-layer depths, which compete to induce or suppress submesoscale circulations in models, respectively. In summer, when mixed layer depths are typically shallow and thus more difficult to resolve in models, the river outflow buoyancy gradients induce stronger submesoscale activity than in the open ocean. In winter, a deep mixed layer would ordinarily have active submesoscales, but the effects of river forcing shoal the mixed layer and slightly reduce submesoscale activity. In model outputs, however, the submesoscales remain typically more active in winter than summer. This is especially true for the integrations analyzed here, where the representation of these circulations in summer is underestimated due to the fixed/limited resolution, and the use of climatological wind forcing (Barkan et al., 2017b) that confined the propagation of the river outflow too close to the coast between May and September compared to observations (`https://waterdata.usgs.gov/nwis/rt`).

Structure function analysis offers additional diagnostics of model fidelity–including comparing seasons–and comparing the summer and winter modeled Eulerian and semi-Lagrangian structure functions suggests very strong seasonality. This contrasts with our particular subset of observations from the GLAD and LASER campaigns which show weak seasonality, potentially due to hurricane activity during GLAD. Additional ongoing tests adjusting the wind forcing show that the use of climatological winds as in the simulations considered here rather than winds including synoptic and inertial variability influences significantly summer statistics, but only moderately winter statistics. Therefore, detailed simulation analysis has been limited to the winter simulations, which we deem most realistic. Within the winter runs, the pattern of release of synthetic drifters as well as location from GLAD and LASER is imposed to robustly assess which of these distinctions is most important, and a gridded large-scale release is performed to isolate the bias induced purely from the semi-Lagrangian nature of surface drifters. The results of the gridded release in summer are also briefly discussed, albeit not shown, to complement the evidence presented in the winter simulations.

Second-order structure functions (Kolmogorov, 1941b; Lindborg, 1999, 2007) offer comparable information to the kinetic energy spectrum (Callies and Ferrari, 2013; Bühler et al., 2014) under

certain limits (Babiano et al., 1985), and given their functionality and practicality for use with irregularly-sampled data, they are often preferred and therefore the focus of this paper. As structure functions of varying orders have been identified theoretically for a variety of turbulent cascades (Kolmogorov, 1941b; Lindborg and Cho, 2000; Lindborg, 2007; McCaffrey, 2015b), the behavior of a turbulent regime can potentially be identified by examining the slope and magnitude of structure functions of different orders. This approach is particularly useful in the upper ocean, where it is postulated that there exists a transition within the submesoscales from quasi-geostrophic turbulence at large scales to a forward energy cascade or inertia-gravity waves at the small scales (Thomas et al., 2008; Callies and Ferrari, 2013). While is it not to goal of this paper to make theoretical comparisons, drifter observations, paired with structure function analysis, could provide an opportunity to substantiate this conjectured transition in the Gulf of Mexico.

Supporting this class of conjecture, Bühler et al. (2014) developed a technique for performing a Helmholtz decomposition of a section of Eulerian velocities into its rotational and divergent parts. Lindborg (2015) adapted this idea to structure functions, which do not require a continuous section of observations, to estimate the rotational and divergent contributions to the flow statistics, again under certain limits (Babiano et al., 1985). Since we hypothesized that the convergence of semi-Lagrangian trajectories would be significant in understanding the biases of surface drifter observations, this decomposition method is applied here to the surface drifter statistics, for which the decomposition is otherwise hard to come by, and the modeled Eulerian field is Helmholtz decomposed directly. To add a complimentary line of evidence, we compute the second order curl and divergence structure functions. Through this analysis, insight into the contributions of oceanic trapping features to the structure functions, as well the relative importance of balanced (nondivergent) geostrophic motion and unbalanced divergent motion across scales, is gained.

2.2 Model Configuration and Trajectory Details

The Regional Oceanic Modeling System (ROMS) (Shchepetkin and McWilliams, 2005) was configured using a sequence of one-way nesting following the procedure outlined in Mason et al. (2010), and focuses on solutions in the Northern Gulf of Mexico near De Soto Canyon with approximately 500 m, nearly isotropic horizontal resolution. To test the effect of resolution on our results, we released 4 clusters of drifters in the center of a higher-level nested domain covering only De Soto Canyon at 150 m horizontal resolution in winter (Barkan et al., 2017a), and found similar outcomes, suggesting that, if there is sensitivity, it occurs at much higher resolution than we can currently afford with the given domain. The atmospheric forcing is climatological, with a QuikSCAT-based daily product of scatterometer wind stresses (Risien and Chelton, 2008), CORE (Large and Yeager, 2009) monthly heat-flux atmospheric forcing, and HOAPS (Andersson et al., 2010) monthly freshwater atmospheric forcing. No tidal forcing is used, and a daily river forcing is applied based on daily river volume flux data from the USGS for the year 2010. The analysis is carried out on the winter months (January, February, March) of year-long equilibrated solutions, using a twice-per-day

output frequency for Eulerian structure function calculations, and higher frequency output to simulate trajectories using the method described below. Additional information about the numerical setup is provided in Barkan et al. (2017b).

Near-surface drifters (hereafter surface drifters) are advected off-line by LTRANS v.2b (North et al., 2011) with a 30-minute averaged Eulerian velocity field located a half-grid cell beneath the surface, and produced by ROMS. All particles are released and confined near the surface through runtime, driven by the upper grid cell current, and the trajectories are sampled hourly for analysis (Choi et al., 2017).

A set of drifter clusters was released to mimic the Grand LAgrangian Experiment (GLAD) and LAgrangian Submesoscale ExpeRiment (LASER) in terms of release location (West vs. East), and release pattern (S- vs. Clover-shaped patterns) for a total of four deployments. To better span the model domain, 28870 particles on a regular grid with an initial separation of 0.02° and centered in the northern Gulf of Mexico were released where the water column is deeper than 50 m, considering that the mixed-layer baroclinic deformation radius cannot be resolved near the shore by our model resolution (Luo et al., 2016; Barkan et al., 2017b).

The deployment locations and patterns for both the gridded and cluster releases are shown in Figure 2.1(a). The S-shape (GLAD-like) and clover (LASER-like) clusters include 90 and 300 particles, respectively. A basic unit of S-shape and clover clusters is a triplet, and there is no fractal setup for the clover clusters. Both clusters are deployed at the centered locations of West or GLAD S1 ($88.13^\circ W, 28.8^\circ N$) site near the Deepwater Horizon site and East or LASER ($87.68^\circ W, 29.05^\circ N$) site near De Soto Canyon. The deployment period (day of year 20-109) mimics LASER, however the deployment patterns and locations mimic both GLAD and LASER. Statistics collected following these semi-Lagrangian trajectories are contrasted versus those evaluated at the Eulerian locations of the model grid. To provide the closest observational analogue, observed trajectory statistics *only* from the the P1 LASER and S1 GLAD deployments are included, and restricted to lie within the model domain.

When any particle reached the boundary of the domain, it was removed from the structure function calculations. Over the three-month experiment, many surface drifters in the cluster releases eventually reached the boundary. Even though sufficient pair separations remain at each scale, half of the western deployments were removed after about 52-54 days, likely due to the proximity to the Mississippi river plume, while the eastern deployment maintained more than half of its drifters for the entire duration of the experiment. Due to the drifters leaving the domain, under- or non-ergodic sampling could potentially explain some of the wiggles at the larger scales present in the second order statistics of the western deployments, but not as strongly present the eastern statistics. Therefore the focus of this study is on the submesoscale and lower end of the mesoscale (i.e. scales less than 30 km), where the impacts of this boundary condition are likely minimal. The second order velocity statistics of the gridded surface drifter release converge well to the Eulerian statistics a the largest scales, and we feel that any impacts of losing surface drifters for this release are negligible.

2.3 Methods

2.3.1 Structure Functions

The structure function is a two-point statistical measure of a fluid property, typically used to evaluate turbulent variability over a given separation (Lindborg, 2015; McCaffrey, 2015a,b). The n-th order velocity structure function is defined as

$$D^n_\gamma(\mathbf{x},\mathbf{r},t) = \langle [u_\gamma(\mathbf{x}+\mathbf{r},t) - u_\gamma(\mathbf{x},t)]^n \rangle. \tag{2.1}$$

Here $\langle ... \rangle$ is an ensemble average, n refers to the order of the structure function (or equally the power of the velocity differences, which are called increments in the turbulence literature), and subscripts refer to either the longitudinal (L) or transverse (T) velocity component.

$$\begin{aligned} \Delta u_L &= (\mathbf{u}(\mathbf{x}+\mathbf{r}) - \mathbf{u}(\mathbf{x})) \cdot \frac{\mathbf{r}}{|\mathbf{r}|}, \\ \Delta u_T &= \hat{\mathbf{k}} \cdot \left[(\mathbf{u}(\mathbf{x}+\mathbf{r}) - \mathbf{u}(\mathbf{x})) \times \frac{\mathbf{r}}{|\mathbf{r}|} \right]. \end{aligned} \tag{2.2}$$

Note that *surface drifters* are the target of this study, which means that all $\mathbf{r}$ separations are restricted to the horizontal, as are all measured velocity components. The magnitude of the transverse velocity component is arrived at by considering only the vertical component ($\hat{\mathbf{k}}\cdot$) of the cross-product between the surface velocity and surface distance. On horizontal separation scales larger than the boundary layer depth, it is expected that horizontal velocity increments will dominate (i.e., $\frac{w}{v} \sim \frac{H}{L} << 1$).

Equation 2.1 represents the average product of velocity differences for the collection of points separated by a distance $\mathbf{r}$. Under homogeneity, the structure function does not depend on absolute location $\mathbf{x}$, just the relative location $\mathbf{r}$. Under isotropy, the statistic does not vary with the absolute direction of $\mathbf{r}$, although it still depends on velocity direction relative to the separation, i.e., transverse versus longitudinal. Thus, the angle brackets will also be taken to average over $\mathbf{x}$ and orientation of $\mathbf{r}$, so $r = ||\mathbf{r}||$ is the sole independent coordinate of the structure functions. It is also assumed that over the three month window, stationarity holds, and therefore time averaged statistics are used. These assumptions lead to the simplified form

$$D^n_\gamma(r) = \langle \Delta u^n_\gamma \rangle \tag{2.3}$$

Where γ is the placeholder for either the transverse or longitudinal velocity component.

Theories predicting power law dependence of the second order structure function in turbulence cascades go back to Kolmogorov (1941b), and the kinetic energy spectrum equivalents are well known (Webb, 1964; McCaffrey, 2015a). These relationships may also be inferred for multiple cascades at different scales, as is common in geophysical flows (McCaffrey, 2015a; Frehlich and Sharman, 2010). Structure functions are a smoothed version of spectra, in the sense that they are related through a Fourier cosine transform (Babiano et al., 1985). Additionally, there are limits in converting from structure function to power spectrum if the spectral slope is too steep or too

shallow. In these limits, the structure function saturates and its slope is not related to the power spectrum slope. Due to the subsampling scheme used for the Eulerian fields, it is only possible to approximate the power spectrum with schemes allowing for gappy or irregular data (e.g., the Lomb-Scargle technique: Press and Rybicki, 1989). Further, with real semi-Lagrangian observations the spectra are poorly constrained (LaCasce, 2016), and so we refrain from detailed estimates of the spectral slope here. The conversion from structure function slope to power spectrum slope is only valid under spectral slopes between -1 and -3 (Babiano et al., 1985), and fortunately the surface submesoscale spectral slopes tend to be near -2 (Capet et al., 2008b). Here, the comparisons emphasize Eulerian structure function to semi-Lagrangian structure function *without any implied conversion to spectral slope*. Thus, these comparisons avoid the limits of Babiano et al. (1985) both physically and methodologically.

Theories relevant to submesoscale dynamics of kinetic energy spectra are summarized by LaCasce (2008); Callies and Ferrari (2013); Poje et al. (2017); Balwada et al. (2016). For third-order structure functions, see Lindborg (1999, 2007); Poje et al. (2017); Balwada et al. (2016). While past studies have utilized these theories to infer characteristics of the Eulerian field, we emphasize that the focus here is not on the evaluation of observations or models versus theories, but on the sensitivity of the amplitude and slope of structure functions to Eulerian and semi-Lagrangian sampling.

Assuming homogeneity, the second-order Eulerian structure function is equivalent to twice the variance minus the auto-covariance $D^2_\gamma(r) = 2(\langle u_\gamma(\mathbf{x})^2\rangle - \langle u_\gamma(\mathbf{x})u_\gamma(\mathbf{x}+\mathbf{r})\rangle)$. Thus, when comparing two second-order structure functions at a given separation r, a larger Eulerian structure function amplitude may result from larger average energy or decreased correlation at that separation scale. Likewise, a shallower structure function slope indicates a slower decay of correlation with separation scale. Although the real ocean is anisotropic, heterogeneous, and non-stationary, frequently it is assumed in observations that the statistical behaviors of homogeneous, stationary, isotropic turbulence scalings are informative, as is often found in idealized simulations operating in the oceanographic parameter range (Soufflet et al., 2016; Bachman et al., 2017). Here the primary concern of how closely Eulerian velocity statistics compare versus semi-Lagrangian surface drifter velocity statistics is added to any concerns about whether idealized turbulence scalings are meaningful in a realistic setting. In a 3D forward energy cascade, the Eulerian expectation is $D^2_\gamma(r) \propto r^{2/3}$ (Richardson, 1922; Kolmogorov, 1941b). In 2D (Kraichnan, 1971) or quasigeostrophic (Charney, 1971) turbulence, the Eulerian expectation is $D^2_\gamma(r) \propto r^2$ in the (potential) enstrophy cascade and $D^2_\gamma(r) \propto r^{2/3}$ in the inverse energy cascade. In the front-dominated submesoscale regime (Capet et al., 2008b), the Eulerian expectation is $D^2_L \propto r$. To give meaning to the third-order longitudinal structure function, the Eulerian expectation is $D^3_\gamma(r) \propto -\epsilon r$ in an energy cascade, where ϵ is the energy cascade rate. The cascade may be forward ($\epsilon > 0$) or inverse ($\epsilon < 0$). This proportionality holds for inverse and forward energy cascades in homogeneous, isotropic turbulence of any dimension (Lindborg and Cho, 2000; Falkovich et al., 2001). We reiterate that surface drifters only sample in two dimensions and where they happen to be, and inertial cascades are an idealization that only partly holds in the real world. Thus, there is no reason to suspect the drifter statistics will correspond to any of the Eulerian

expectations proposed above, which are formulated for homogeneous, isotropic, divergenceless flows. However, elsewhere in the literature theoretical inferences based on drifter statistics have been made, and it is therefore paramount to understand if surface drifter sampling is sufficiently different from Eulerian sampling to bias statistics.

2.3.2 Wilcoxon Rank Sum Test

To assess the statistical significance of differences between surface drifter and Eulerian structure functions, a Wilcoxon rank sum test (WRST) is performed. This non-parametric test is suitable for addressing continuous distributions that are non-Gaussian, have few elements, or compare datasets of different lengths. As with other positive-definite variables subject to extreme events, probability density functions (PDFs) of the structure function values at every scale (not shown) are extremely right-skewed. The observed distribution function makes the WRST an ideal test for our datasets.

Rank tests are based on the place of each observation in ordered data (the rank), and assesses the closeness of two datasets by comparing the medians. The highly skewed PDFs of both Eulerian and surface drifter structure functions (potentially due to intermittency, GPS positioning errors etc.) suggest the median may be the preferred center of the data, in contrast to the mean, which is traditionally used when calculating structure functions. Unlike the mean, the median is not very sensitive to outliers. Structure functions calculated with means are likely to be even less similar due to sampling biases, and therefore we suggest that the median may be preferred when using semi-Lagrangian data to gain the best estimates of the Eulerian statistics, as the effects of sampling bias and any added instrumentation noise are somewhat mediated by its use. Moore et al. (2014) provides the detailed procedure.

The null hypothesis is that the two samples, s_1 and s_2, with size n_1 and n_2 respectively, are from distributions with equal medians, tested against the alternative that the medians are not equal. Both data sets are grouped into one larger set, S, with size $N = n_1 + n_2$. S is ordered from largest to smallest, and the rank corresponding to the position in the ordered dataset is noted for each element. The ranks for each piece of data belonging to the smaller of the original sets is summed, forming the corresponding variable W (the fact that we use the smaller set does not influence the results, see Moore et al. (2014)). If W varies much from its expected value (i.e., probability-weighted mean), it is determined that the samples are pulled from distributions with different medians. More precisely, if the probability (p-value) of getting such a value W, given that the populations are drawn from distributions with equal medians, is high, then the null hypothesis is accepted.

2.3.3 Helmholtz Decomposition

Any velocity field can be decomposed into longitudinal and transverse components. If the velocity field is well-behaved, it can also be decomposed into rotational and divergent components, although uniqueness is not guaranteed in a bounded domain (Fox-Kemper et al., 2003). For isotropic flows in

which the component motions are uncorrelated,[1] then

$$\begin{gathered}\mathbf{u} = \mathbf{u}_L + \mathbf{u}_T = \mathbf{u}_R + \mathbf{u}_D, \\ \langle \Delta u^2 \rangle = \langle \Delta u_L^2 \rangle + \langle \Delta u_T^2 \rangle = \langle \Delta \mathbf{u}_R \cdot \Delta \mathbf{u}_R \rangle + \langle \Delta \mathbf{u}_D \cdot \Delta \mathbf{u}_D \rangle, \\ D^2 = D_L^2 + D_T^2 = D_R^2 + D_D^2.\end{gathered} \tag{2.4}$$

D_R^2 and D_D^2 are the rotational and divergent structure function respectively. For the Eulerian field, we directly compute the Helmholtz decomposition of the velocity field to generate the divergent and rotational velocity structure functions using independently vanishing boundary conditions. In order to minimize the effects of boundaries, where non-uniqueness may be concentrated, a subset of the data far from the coast and model domain edges is used.

The semi-Lagrangian versions of D_R^2 and D_D^2 could in principle be estimated by sampling the Eulerian fields nearest the positions of the model trajectories and observations. However, the subset domain for the Helmholtz decomposition removes many drifters from consideration, and prevents a full range of scales from being realized when calculating the structure functions, so instead the method of Lindborg (2015) is used to decompose the semi-Lagrangian velocities.

Stemming from the spectral approach to decompose the velocity field by Bühler et al. (2014), Lindborg (2015) showed that similar techniques can be used to estimate the second order divergent and rotational structure functions from the second order transverse and longitudinal structure functions

$$\begin{aligned}D_R^2 &= D_T^2 + \int_0^r \frac{1}{r}(D_T^2 - D_L^2)dr, \\ D_D^2 &= D_L^2 + \int_0^r \frac{1}{r}(D_L^2 - D_T^2)dr.\end{aligned} \tag{2.5}$$

and we employ this method to estimate the semi-Lagrangian rotational and divergent structure functions. Each of these equations contains two terms, one being the related velocity component, and the other the integrated exchange of dominance between the longitudinal and transverse structure functions necessary to maintain the budget of the rotational and divergent components. Note that all second-order (and indeed all even-order) structure functions should be positive from (2.3), although the Lindborg (2015) procedure in (2.5) does not guarantee positive-definiteness.

In preparation for integration, and solely for this purpose, the structure functions were first interpolated using a cubic spline. The residuals (not shown) suggest a reasonable fit, and these interpolated curves were used as arguments for (2.5), and the trapezoid rule was utilized for integration. It is important to point out that our discrete scheme does not have an accurate lower limit below the smallest sampled length scale of around 500 m. To address this, we fit both D_L and D_T to power laws, allowing for varying slopes and coefficients, $c_{1,2}$ and $s_{1,2}$ respectively. That is, we represent the structure functions as $D_T^2 = c_1 r^{s_1}, D_L^2 = c_2 r^{s_2}$. Under the assumption that the observed scales follow the same power laws as the unobserved scales, we can estimate the contributions

[1] In homogeneous, isotropic, stationary non-divergent turbulence it is straightforward using Fourier expansions to show that both transverse and longitudinal and rotational and divergent components should be uncorrelated. However, in divergent flows, transverse and longitudinal components can be correlated. Rotational and divergent components are expected to be correlated in a bounded domain or heterogeneous flow (Fox-Kemper et al., 2003).

of the small scales to the integrals in the Helmholtz decomposition method as

$$\int_0^{r_{min}} \frac{1}{r}(D_T^2 - D_L^2)dr = (c_1/s_1)r^{s_1} - (c_2/s_2)r^{s_2}\Big|_0^{r_{min}}. \tag{2.6}$$

where r_{min} is the smallest observed scale, taken to be around 500 m, and the coefficients and powers of r are found using the fit parameters from the observed scale power laws. These contributions were typically small.

2.3.4 Specifications

For this project, both semi-Lagrangian and Eulerian versions of the second order structure function, as well as the corresponding Helmholtz decompositions were calculated. Due to a large domain with high resolution, the model grid was randomly subsampled to obtain Eulerian statistics, with bootstrapping uncertainties calculated in the process. While the advantages of a structured grid are lost in this process, the structure function, unlike most Fourier methods, does not rely heavily on a uniformly sampled grid. To ensure this sampling did not significantly affect the results, random sampling of various levels of spatial and temporal coverage was performed. With relatively high spatial coverage especially at the small scales, and low but diverse temporal coverage, the Eulerian structure function statistics were deemed representative of the true Eulerian statistics. Thus 7,000 spatial points were considered (5,000 points were initially randomly sampled, and then another 2,000 points were added by taking 20 points near 100 of the original 5,000 points to ensure the small scale separations were well observed), and 19 time steps (about 6 per month roughly evenly distributed between days and nights). A similar setup was used to subsample the gridded Lagrangian releases such that 7000 drifters were ultimately tracked on the same 19 time steps used for the Eulerian structure functions. For the cluster release second and third order structure functions, no subsampling was implemented, and all drifters within the domain were used at every time step. However, for the divergence and curl structure functions, the grid was not sampled randomly as for the Eulerian statistics, but rather the nearest grid point to each drifter at every time step was found from the Eulerian fields. All structure functions were binned by separation distance such that roughly every fourth bin was a factor of 10 increase in scale.

2.4 Results

2.4.1 Second Order Structure Functions

Before introducing the results of the comparisons between the gridded and cluster release structure functions and the Eulerian statistics, we direct the reader once more to the relationship, assuming homogeneity, between the second order structure function and the auto-correlation function: $D_\gamma^2(r) = 2(\langle u_\gamma(\mathbf{x})^2\rangle - \langle u_\gamma(\mathbf{x})u_\gamma(\mathbf{x}+\mathbf{r})\rangle)$. Thus, at a given separation r, if one is larger than the other, it could be the result from larger average energy or decreased correlation, and vice versa.

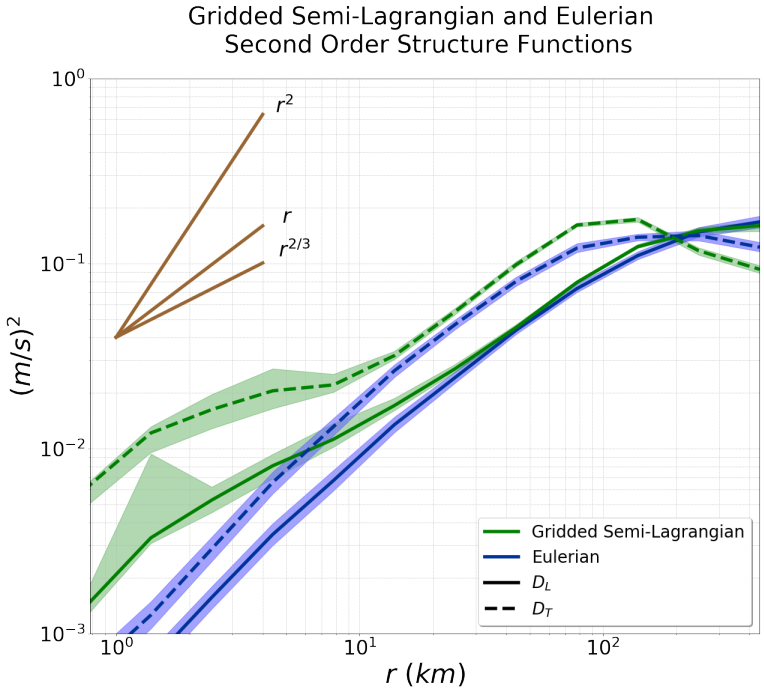

Figure 2.2: The gridded semi-Lagrangian and Eulerian second order longitudinal (D_L^2) and transverse (D_T^2) velocity structure functions. All structure functions here are calculated by using means, in contrast to the medians used in the WRST. Structure functions found at each time step are bootstrapped with 10,000 resamples to obtain 95% confidence intervals, as noted by shading around them. A guideline of slope 1 and 2/3 is provided.

The semi-Lagrangian second order structure functions for the gridded release (hereafter GSF2s, green) and Eulerian second order structure functions (hereafter ESF2s, blue) are plotted in Figure 2.2. The ESF2s at each time step were bootstrapped to obtain a 95% confidence interval using 10,000 resamples, as indicated by shading. Striking is the similarity between the GSF2s and ESF2s at large scales, and dissimilarity at smaller scales. Below about 10 km the GSF2s move from scaling as r to scaling nearer $r^{2/3}$, while the Eulerian statistics continue to scale as r. We note here that the summer simulations exhibit similar behavior, although the departure is for scales less than 8km. This suggests that if enough drifters are released, it is possible to accurately represent the largest scales well in terms of slope, albeit still not the magnitude of the structure functions since the Eulerian and gridded structure functions are outside of each other's confidence intervals for nearly the entire range of scales due to the offsets. This is in keeping with the idea that divergenceless quasi-geostrophic dynamics tend to dominate the mesoscale, and thus we may expect biases induced from convergent zones alone to be less present here.

The semi-Lagrangian second order structure functions for the cluster releases (hereafter CSF2s, dashed and dotted) and ESF2s (solid) are plotted in Figure 2.3. It is worth pointing out that the CSF2s (and observations) are more variable across scales than both the ESF2s, which tend to be

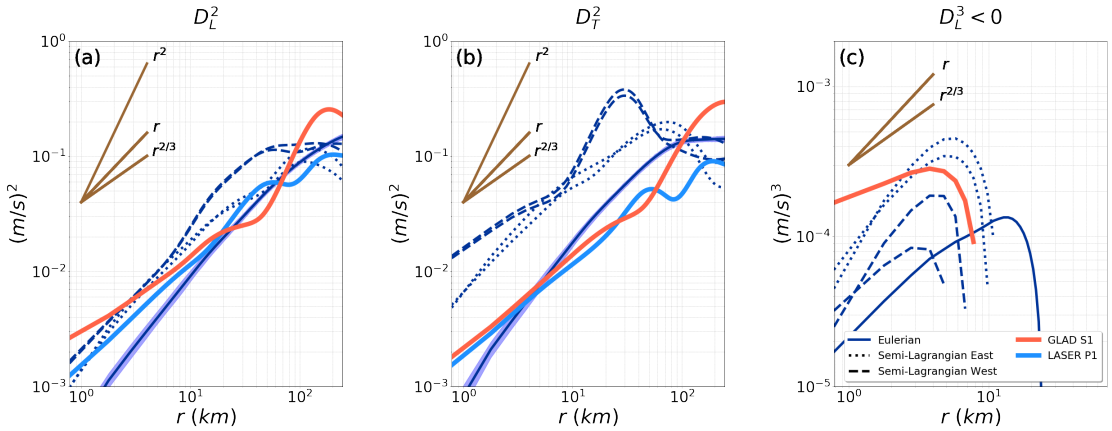

Figure 2.3: The second order structure functions of (a) longitudinal D_L^2 and (b) transverse D_T^2 velocities, and (c) the third order structure function of longitudinal velocity D_L^3. All structure functions here are calculated by using means, in contrast to the medians used in the WRST. The Eulerian structure functions found at each time step are bootstrapped with 10,000 resamples to obtain 95% confidence intervals, as noted by shading around them in (a) and (b). The dashed and dotted lines represent semi-Lagrangian structure functions with different deployment locations, and differences between lines with the same line-style represent varying deployment patterns. The deviations due to differing deployment patterns are typically small or under-resolved with our model resolution. Guidelines with slopes of 2,1,and 2/3 are provided by the solid brown lines for reference. Only the absolute values of negative data points are plotted here. Note that LASER P1 and one of the summer eastern trajectories only had one negative value in this range at the smallest bin, and are not plotted. A guideline of slope 1 and 2/3 is provided.

smooth and linear in log-log space, and the GSF2s, which show dramatically less variability across scales. As discussed previously, this could be an effect of choosing to remove drifters that reach the boundary, and thus much of the analysis presented focuses on scales where the impact is assumed to be smallest, those less than 30 km. Additionally we note that the effective resolution for the 500 m simulations is estimated as 4 km, and this should be kept in mind when interpreting flows on the low end of the submesoscale.

The slopes for the ESF2s and CSF2s differ systematically. The ESF2s share nearly the same slope, scaling as $\sim r$, or a bit more steeply, but far short of r^2. In contrast, there are variations among slopes in the CSF2s, particularly in D_T^2. However, the CSF2 slopes are typically shallower than the ESF2 slopes, especially at small scales and in D_T^2. When shallower, the CSFs slopes are near $r^{2/3}$. The LASER drifter observations, which are also semi-Lagrangian, have shallow slopes near $r^{2/3}$, although at roughly an order of magnitude less energy in the transverse velocity. Overall, the semi-Lagrangian structure functions are typically shallower than Eulerian structure functions, and this opens the question as to whether the scaling observed in the trajectories and observations may result in part from biased sampling.

The CSF2s generally overestimate the ESF2, particularly in D_T^2. To put this into context, when the submesoscale is more energetic and ubiquitous, it is expected that drifters are actively drawn into features more energetic than the typical velocity field, such as fronts, which could cause an increase

in magnitude of the CSF2s. The effect, however, will not necessarily expand across all scales, and local effects at key length scales could result in enhanced variability, or if increases persist across a subset of scales, the slope could be altered.

It is notable that within the CSF2s, D_T^2 shows a larger jump in magnitude from the ESF2 than does D_L^2. This could be attributed to drifters trapped in more persistent eddies, which might amplify the magnitude of the transverse velocity component across scales. We also note that for the western deployments, the large jump in magnitude in D_T^2 around 12km could be due to non-ergodic sampling, but that the eastern deployments are less likely subject to this problem. Further, as structure functions are formulated in a relative coordinate system, the conversion to frontal coordinates is not obvious. Therefore expected impacts onto the longitudinal and transverse components of drifters being drawn into fronts are not clear, except to say that the semi-Lagrangian and Eulerian structure functions are likely to be different as the energy and variability sampled are different.

Other differences within the CSF2s arise due to deployment location and launch pattern (note the ESF2 and GSF2 do not have these dependencies). Figures 2.3(a,b) show distinct groupings of East vs. West sets present in both D_L^2 and D_T^2, but is especially strong in D_T^2. The structure functions are not sensitive to whether particles are deployed in a clover or S-patterns, so they are given the same line-type in Figure 2.3. It is possible that these distinctions would be larger in simulations at higher resolution, as the patterns are small when compared to the model grid, so advection differences are only due to interpolation rather than turbulence on sub-kilometer scales. In our additional analysis of the simulation at 150m horizontal resolution, we find the differences between the structure functions are more pronounced, but are still weak compared to those from deployment location. Thus higher resolution yet may still be needed to isolate any deployment strategy effects on the structure functions.

We note that the model results do not reproduce LASER P1 observations exactly, particularly in D_T where the synthetic CSF2s overestimate the LASER P1 second order structure function by an order of magnitude. These differences could be attributed to numerical errors of the advection scheme used to propagate the particles, or more likely the limitations of the climatological forcing in the model. Climatological winds reduce the forcing of internal waves typically generated from high-frequency wind events (e.g. hurricanes or winter storms), and can be a major contributer to the small-scale spectrum (Callies and Ferrari, 2013), and therefore significantly alter structure functions (Beron-Vera and LaCasce, 2016).

Additionally, seasonal and inter-annual variability of river forcing have significant effects on the statistics of submesoscale circulations in the Northern GoM (Barkan et al., 2017b). A strong El Niño during LASER produced larger river discharge than during GLAD (`https://waterdata.usgs.gov/nwis/rt`) – an effect that is not included in the climatological wind, river, and heat flux forcing for the synthetic CSF2s– and could have also altered the structure functions enough to be different from what average conditions would have produced.

Finally, the eddy kinetic energy in the model is likely to be overestimated at all scales due to the absence of atmospheric coupling (Luo et al., 2016). The convergence of drifters in energetic

submesoscale structures, responsible for the ESF2-CSF2 differences, however, is well documented in both the model (Choi et al., 2017) and observations (Poje et al., 2014; D'Asaro et al., 2018).

2.4.2 Third Order Structure Functions

The negative portions of the Eulerian and semi-Lagrangian third order cluster release structure functions (ESF3s and CSF3s) are shown in Fig. 2.3c. Generally, winter energetics are amplified by semi-Lagrangian sampling: overestimating here by a factor of 2 to 8 in ϵ according to the standard linear fit to the homogeneous, isotropic energy cascade prediction. However, the power laws observed are more sensitive to launch pattern, as noted by curves with similar linestyle producing different slopes–consistent with added sensitivity of this higher-order statistic. As in other studies, only the negative third order structure function magnitudes are plotted which correspond to the values theoretically linked to a forward energy cascade (Lindborg and Cho, 2000; Poje et al., 2017). Both ESF3s and synthetic CSF3s generally scale as $\sim r$. Interestingly, the shallowest slope is from the GLAD observations, which is shallower still than $r^{2/3}$. A sign change is present in both ESF3s and all synthetic CSF3s across this range of scales. The LASER P1 third-order structure function only contains one negative value within the smallest bin (not shown), in contrast to GLAD, which shows a transition scale similar to the model CSF3s. The CSF3s consistently change sign at smaller separation scales than their corresponding ESF3s. Thus modeled CSF3s *underestimate the largest scale of the sign change* by 2-20 km, and CSF3s are *consistently larger in magnitude* by a factor of 2-8 than the ESF3s. The energy flux estimate in Figure 7b of Poje et al. (2017), which assumes the homogeneous, isotropic, arbitrary dimensionality d scaling for an energy cascade $\epsilon = -\frac{d(d+2)}{12r} D_L^3(r)$ following Falkovich et al. (2001)–but uses the CSF3 instead of the ESF3–will systematically and significantly overestimate the estimated spectral energy flux (ϵ) and underestimate the transition scale to a forward energy cascade regardless of dimensionality. The large scale separations could be affected by the non-ergodic sampling imposed by the domain boundary, but we assume these effects all occur on scales less than 30 km. Further, it should be emphasized that even though some modeled (and observed) structure function slopes appear to be consistent with some predictions of 3D Kolmogorov turbulence, the nature of the modeled flow at these scales can not be 3D turbulence due to resolution, numerics, and the length scales of the flows in question.

2.4.3 Wilcoxon Rank Sum Test

Figure 2.4 shows the medians for the grouped CSF2s and the ESF2s, with shading denoting the interquartile range. Superimposed on each data point is a marker which signifies the result of the Wilcoxon rank sum test (WRST). A circle means the test rejected the null hypothesis that the Eulerian and semi-Lagrangian data at each scale come from distributions with equal medians. A star implies the null hypothesis is accepted with a supporting p-value greater than 0.05.

When we consider the measures of center, that is the mean or median, rather than samples drawn from this distribution, the comparison is more selective. In addition, the median is less sensitive

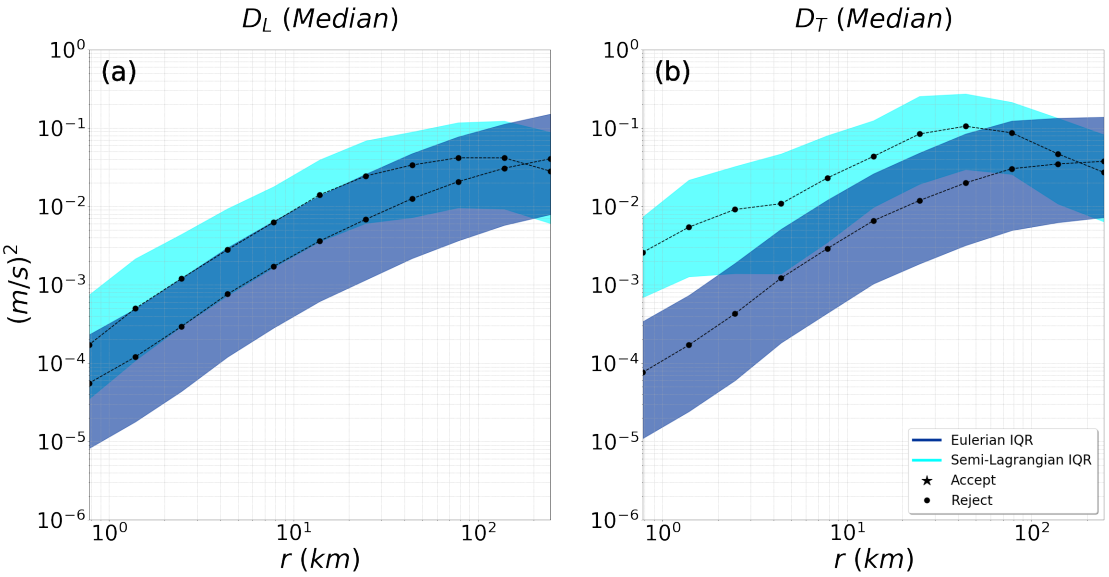

Figure 2.4: Medians of ESF2s and LSF2s in winter. The interquartile range is represented by shading. Circles represent rejection of the null hypothesis that the two datasets have equal medians. Stars represent acceptance of this hypothesis with a corresponding p-value of greater than 0.05.

to outliers, and may be a more representative measure of center than the traditional mean. For comparison of medians by WRST, the ESF2s and CSF2s disagree across all scales. This is largely due to the size of the sets being compared. With deployments of 90-300 drifters, and a time frame of 3 months, there are millions of data points within a given bin of the CSF2s, and the ESF2s also contain a comparable amount of points. This makes knowledge of the median quite certain, and the test becomes extremely sensitive to any differences between the two datasets, even though the qualitative similarity in Fig. 2.4 is striking. At the rawest level however, the structure function interquartile range only overlaps sufficiently across scales in D_L, suggesting that even within the spread of the data there are differences between CSFs and ESFs. In sum, *a statistically significant difference is the rule between the Eulerian and semi-Lagrangian second order structure functions.*

2.4.4 Helmholtz Decomposition

The divergent and rotational structure functions of the cluster releases are plotted in Fig. 2.5(a,b). A challenge of interpretation is that the Lindborg (2015) method frequently arrived at negative divergent structure functions for both CSF2s and ESF2s due to the large differences between the longitudinal and transverse statistics. While this method fails to reproduce the Eulerian divergent structure functions well, the rotational structure functions are captured much better, both in terms of sign and magnitude (not shown). Note from the Eulerian structure functions in Fig. 2.5(a,b) that the rotational structure functions are significantly larger in magnitude than the divergent ones, especially on larger scales, which suggests that small errors in the rotational part may overwhelm the divergent part in (2.5). This point is highlighted by the fact that the transverse components are more

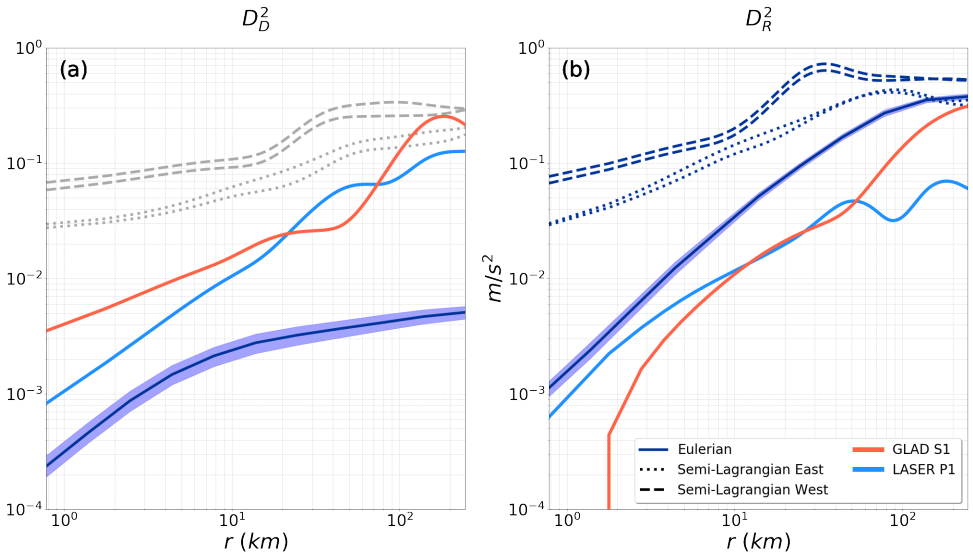

Figure 2.5: The second order structure functions of (a) divergent D_D^2, and (b) rotational D_R^2 motions. Eulerian structure functions are calculated by decomposing the velocity field directly. The semi-Lagrangian cluster release structure functions are calculated from the longitudinal and transverse structure functions following Lindborg (2015). Note that for (a) the semi-Lagrangian divergence structure functions are faded gray, as they were all negative, but have been reproduced as positive values on this plot to make clear their magnitude is similar to that of other positive structure functions.

consistent if the number of drifters increases. Furthermore, note that the Eulerian modeled rotational and divergent parts do not share the same slope or largest correlation scale, which is perhaps expected from theory (McWilliams, 1985), but should inform the understanding of errors in (2.5). Beyond the significance of these internal discrepancies, however, the Eulerian and semi-Lagrangian structure functions are drastically different from one another, in support of the hypothesis that semi-Lagrangian statistics are biased in ways that may correlate with convergent zones.

The divergent structure functions for the synthetic cluster trajectories were completely negative (denoted by faded colors in the plot, see caption). The negative values are problematic, as (2.3) demands that D_D^2 and D_R^2 should be non-negative. Lindborg (2015) also comes across this problem, albeit only at the largest of scales, and suggests anisotropy is the issue. We examined the anisotropic, or angle dependent, structure functions by removing averaging over angles (not shown) and similarly the spatially-dependent structure functions by removing averaging over location ($\mathbf{x}$). However, due to the particular sampling patterns of the trajectories, gaps in directional and spatial information exist, making it impossible to attribute the presence of negative values to anisotropy or heterogeneity. A number of issues could ultimately affect the results of this decomposition. Aside from those addressed above, we find that the cross-correlations between rotational and divergent parts of the velocity (not shown) are non-negligible, and as suggested above the difference in magnitude between rotational and divergent parts makes estimating the minor (divergent) contributor error-prone.

To get a handle on the limitations of this theory for our data, we assess how large D_T^2 needs to be in order to produce negative values of D_D^2 due to the difference of D_T^2 and D_D^2 in the integral term of (2.5) alone. Assuming positive and equal slopes (s), and positive yet different magnitudes (c_1 for D_L^2 and c_2 for D_T^2), we find the ratio $\beta = \frac{c_1}{c_2} = \frac{D_L^2}{D_T^2}$ to be bounded as: $\frac{1}{1+s} \leq \beta \leq s+1$. For the ESF2s, $s \approx 1 \rightarrow 1/2 \leq \beta \leq 2$. Callies and Ferrari (2013) and Balwada et al. (2016) use similar ratios to argue for wave-like or vortex-like cascades from ESF2s. By contrast, the modeled rotational and divergent ESF2s do not have the same slope. Here, using the CSF2s, β is estimated by averaging the ratios of y-intercepts of D_L^2 and D_T^2. From this analysis, $\beta \approx 0.0798$, well below the threshold for which we expect the divergent structure function to be negative.

If these concerns with the Lindborg (2015) method are put aside and the structure functions in Fig. 2.5(a,b) are taken at face value, then overall the divergent part of the observations is larger than in the model, perhaps indicating that forced variability (e.g., internal waves) or resolution limitations are significant. However, it is difficult to eliminate the possibility that the particular boundary conditions chosen for the Helmholtz decomposition may be the source of these divergent motions. The large discrepancy between modeled Eulerian and semi-Lagrangian rotational structure functions and the failure of the Lindborg (2015) method to predict positive semi-Lagrangian divergent structure functions both suggest significant caution in interpreting the Helmholtz-decomposed observed structure functions without comparable Eulerian observations.

Another approach to understanding the impacts of convergent zones is directly calculating the structure functions of the curl and divergence of the velocity field, denoted (ECSF,EDSF) for Eulerian, and (CCSF,CDSF) for the semi-Lagrangian clusters. These fields can be interpreted as twice the enstrophy or divergence-squared minus the autocorrelation of the curl or divergence. It is possible to apply this approach to real drifter trajectories by estimating divergence and vorticity fields (e.g. D'Asaro et al. (2018)). However, in the model these fields are readily available. Further, unlike the Helmholtz decomposition, there are no issues of non-unique decompositions, and we do not have to subset the domain. Therefore we are capable of producing semi-Lagrangian estimates of the structure functions by utilizing the Eulerian fields to estimate the Lagrangian fields. These structure functions are plotted in Fig. 2.6, with bootstrapped 95% confidence intervals from 10,000 resamples denoted by shading for the Eulerian structure functions.

It is expected that curl and divergence structure functions will be flatter than the velocity structure functions, as they are related through derivatives with respect to r when in power-law regimes. Interestingly, the EDSFs are nearly flat for the entire range of scales, while the CDSFs and both CCSFs and ECSFs show a significant power law on the smaller scales, and only flatten out above 10 km (well above the estimated effective resolution and below the range of scales at which boundaries may come into play). Over this range of scales the CSFs are sloped more steeply than the ESFs, and this implies there is greater autocorrelation of divergence, and also of curl, in the CSFs than in the ESFs. This is probably indicative of convergent coherent structures with correlated divergence and curl, as evidenced by the cross-correlations noted previously between the divergence and vorticity. Further, both the Eulerian transverse and longitudinal velocity structure functions

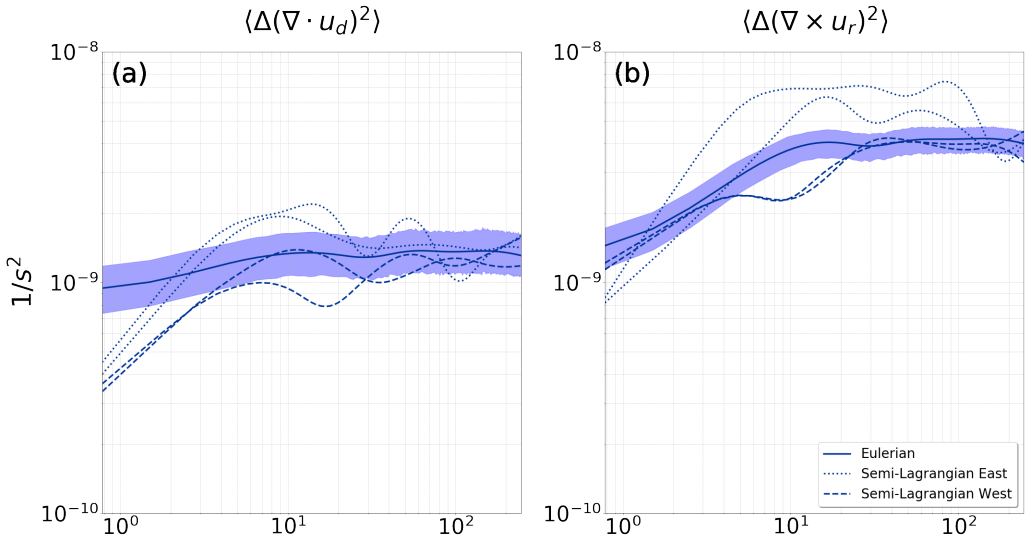

Figure 2.6: Second order structure functions from the cluster releases of (a) divergence, and (b) curl calculated using means. Bootstrapped 95% confidence intervals for the Eulerian statistics from 10,000 resamples are denoted by shading.

of Figure 2.2 scale as r, which, if taken as representative of a front-dominated regime, means it is possible to not only have non-zero, but also different divergence and curl structure function slopes for this class of turbulence.

The scale of the largest coherent features for which the semi-Lagrangian and Eulerian structure functions differ in slope is about 10 km, and this correlation over smaller length scales agrees with expectations that gradients increase the appearance of finer scale features. This is also in agreement with the gridded releases, whose second order velocity structure functions deviate from the Eulerian statistics most strongly at 10 km and below. Note that it is the correlation across scales that we treat as evidence of 'drifter trapping'. Assuming homogeneity and that variables decorrelate at the largest scales then $D^2_\gamma(r) = D^2(\infty) - 2\langle u_\gamma(\mathbf{x})u_\gamma(\mathbf{x}+\mathbf{r})\rangle)$, and the correlation at separation r is equal to half the difference between the largest-scale structure function $D^2(\infty)$ and $D^2(r)$. In reality decorrelation occurs at finite r and both the Eulerian and drifter structure functions plateau to similar values ($\approx D^2(\infty) = 2\langle u_\gamma(\mathbf{x})^2\rangle$). As a result, smaller structure functions at a given scale imply more correlation at that scale, rather than decreased variance, and equivalently steeper slopes imply a greater increase in correlation with decreasing r. Our results show that drifter structure functions fall below Eulerian structure functions below 10km where the drifters have biased sampling and are therefore more correlated.

The positive definiteness of this statistic tends to blend convergence and divergence together, and separating them explicitly is not possible with these metrics. However, we suggest at the scales over which the semi-Lagrangian structure functions are strongly correlated, and therefore within features of similar convergence (possibly divergence), coincide with submesoscale frontogenesis or

other convergent features, and use that as the primary interpretation as demonstrated in D'Asaro et al. (2018, e.g. see Figure 5), although others may be possible. This interpretation is also in keeping with the results of a PDF analysis from a similar setup in Choi et al. (2017), where it was shown through the Kullback-Leibler divergence measure (Kullback and Leibler, 1951) that the semi-Lagrangian PDFs of both vorticity and divergence were different from the Eulerian PDFs for the duration of the experiment.

Most of the CDSFs and CCSFs fall approximately within confidence intervals of the Eulerian structure functions at scales above 10 km. The curl and divergence decorrelation length scale, that is the scale above which the respective structure functions flatten out, is generally consistent between Eulerian and semi-Lagrangian estimates, with the exception of the eastern deployment which overestimates the ECSF across most scales. Below 10 km, the Eulerian fields tend to have shallower slope, indicating less detected small-scale correlation than in the semi-Lagrangian sampling. This effect is more pronounced in the divergence structure function, rather than the curl, suggesting that small scale convergences could indeed be oversampled in the semi-Lagrangian locations. In contrast, the breakpoint in scale between correlated and uncorrelated variability is fairly consistent between the Eulerian and semi-Lagrangian estimates.

2.5 Conclusions

By examining the sensitivity of structure functions to semi-Lagrangian data it is revealed that semi-Lagrangian structure functions are susceptible to changes in both magnitude and slope compared to corresponding Eulerian statistics. The degree of this effect in the cluster releases depends strongly on launch location and weakly on launch pattern, preventing a direct correction of observed semi-Lagrangian statistics to an equivalent Eulerian slope and magnitude. Gridded releases help to isolate the biases solely due to the semi-Lagrangian nature of the surface drifters, and like the cluster releases show systematic differences when compared to the Eulerian structure functions, although unlike the cluster releases better approximate the structure function slope at the large scales, but not the magnitude. Generally, both the GSF2s and CSF2s tend to indicate preferential sampling of energetic submesoscales, confirming the PDF analysis in Choi et al. (2017), with slopes that are shallower than Eulerian statistics. All third order CSFs show a change of sign reliably, but overestimate the energy flux and underestimate the largest scales involved in the cascade. When taken collectively, the CSFs are statistically distinct from ESFs. The breakdown of the Helmholtz decomposition method in the trajectories causes concern for clear interpretation. However, evaluating the curl and divergence structure functions directly shows important differences between semi-Lagrangian and Eulerian correlations of these fields on scales below 10 km–i.e., the submesoscales. The Eulerian structure functions are flatter, and therefore less strongly correlated at small scales than the semi-Lagrangian structure functions. This is consistent with the notion that drifters collect in convergent, coherent structures (D'Asaro et al., 2018), and calls to question the interpretation of previous studies using drifter statistics at pair separations below 10 km (e.g Balwada et al., 2016; Poje et al., 2017)

to extrapolate information about the Eulerian flow field. Surface drifter statistics for separations below 10 km consistently exhibit scaling laws close to 2/3, which are shallower than the Eulerian second order statistics, as shown in this work. From our analysis it is apparent that the effects of the submesoscale trapping structures diminish with scale, and drifter statistics at mesoscale separations remain reliable, provided that sampling is sufficient.

2.6 Acknowledgments

This research was made possible in part by a grant from The Gulf of Mexico Research Initiative, and in part by the National Key Research Program of China (2017YFA0604100). Data are publicly available through the Gulf of Mexico Research Initiative Information & Data Cooperative (GRIIDC) at https://data.gulfresearchinitiative.org (doi: 10.7266/N7JS9NVS, 10.7266/N75H7DQ5, Jun Particles).

Chapter 3

Refining the Bias: Accumulation vs. Background Bias from Surface Drifter Observations

This chapter is in revision for the Journal of Geophysical Research: Oceans with the title "Biases in structure functions from observations of submesoscale flows", with lead author Jenna Pearson and coauthors Baylor Fox-Kemper, Brodie Pearson, Henry Chang, Brian K. Haus, Jochen Horstmann, Helga S. Huntley, A.D. Kirwan, Jr., Bjöorn Lund, and Andrew Poje. This chapter has two objectives: (1) to utilize regional and local observing platforms to validate the numerical modelling results presented in Pearson et al. (2019), and (2) to refine the types of biases that manifest in structure functions due to sampling of regions of strong convergence and vorticity. Comparison of Eulerian and semi-Lagrangian structure functions yield similar results to that of Pearson et al. (2019), shallower semi-Lagrangian than Eulerian second-order structure functions, and larger magnitude third-order structure functions. However, this biases identified here are two-fold. The first is an accumulation bias, similar to that discussed in Chapter 2. The second is a background bias related to a non-zero first-order structure function, which is correctable unlike the accumulation bias. The benefits of the biases identified in this chapter are then used in Chapter 1 alongside other semi-Lagrangian statistics to describe flow features related to convergence and rotation.

Abstract

Surface drifter observations from the LASER campaign in the Gulf of Mexico are paired with Eulerian (ship-borne X-band radar) data to demonstrate that velocity structure functions from drifters differ systematically from Eulerian structure functions over scales from 0.4 to 7 km. These differences result from drifters oversampling surface convergences and regions of intense vorticity. The first-, second-, and third-order structure functions are calculated using quasi-Lagrangian (drifter) and

Eulerian data from approximately the same location and time. Differences between quasi-Lagrangian and Eulerian structure functions are attributed to two forms of bias. The first bias results from the mean divergence or vorticity of the background flow creating non-zero first-order structure functions. This background bias affects both quasi-Lagrangian and Eulerian data when insufficiently time-averaged. It severely biases the drifter third-order structure functions, but is smaller in Eulerian structure functions at both second and third order. This bias can be corrected for using lower-order structure functions. The second form of bias results from drifters accumulating in regions with flow statistics that differ from under-sampled regions. This accumulation bias is diagnosed by identifying the dependence of the Eulerian structure functions on divergence and vorticity as well as scale. Together both biases suggest that caution is needed when interpreting second-order drifter statistics, and that linking raw third-order drifter statistics to energy fluxes is often erroneous in ocean data: even with background correction and sufficient time-averaging, drifters overestimate the Eulerian estimate of the third-order structure function by up to a factor of 5 when signs are consistent.

Plain Language Summary

Structure functions are a statistic used to measure the spreading of material floating in the ocean, such as plastics or spilled oil, as well as the transfer of properties like energy across scales. Their calculation requires knowledge of velocities of nearby particles. These can be measured either by (nearly) stationary instruments, such as a radar, or by tracking drifters. Offshore drifter tracking is generally easier, but they are known to be attracted to specific flow features, such as fronts, windrows, and vortices, leading to less sampling of other areas. By considering a unique dataset of nearly simultaneous velocity measurements from both radar and drifters, this paper investigates how the uneven sampling by drifters, as well as the limited area coverage of radar measurements, impacts the structure function statistics and their interpretation.

3.1 Introduction

Surface dispersion of plankton, contaminants, and plastics is largely controlled by the variability of surface currents over a rich array of scales. While absolute dispersion is dominated by mesoscale and larger ($\geq \mathcal{O}(100\,\mathrm{km})$) motion, for relative dispersion the submesoscales — characterized by horizontal scales of $\mathcal{O}(0.1 - 10\ \mathrm{km})$, timescales of hours to days, and $\mathcal{O}(1)$ Rossby and Richardson numbers — are of particular importance. The equal competition of planetary vorticity with horizontal shear at submesoscales leads to a transition from large quasi-geostrophically balanced motions to smaller forward-cascading turbulence, providing a pathway for dissipation of both energy and tracer variance McWilliams et al. (2001); McWilliams (2016). Submesoscale phenomena are pervasive in the mixed layer as seen in observations Poje et al. (2014); Omand et al. (2015); Callies et al. (2015); Buckingham et al. (2016); Johnson et al. (2016); Ohlmann et al. (2017); du Plessis et al. (2019) and suggested

by numerical models and theory Thomas et al. (2008); Capet et al. (2008b,a,c); Fox-Kemper et al. (2011); Zhong et al. (2012); Luo et al. (2016). They are strong contributors to the transfer of energy between scales and energy dissipation Molemaker et al. (2005); McWilliams (2008); D'Asaro et al. (2011); Poje et al. (2017) and affect the distribution of biogeochemical variables throughout the near-surface ocean Mahadevan and Tandon (2006); Klein and Lapeyre (2009); Zhong et al. (2012); Li et al. (2012); Omand et al. (2015). Although ubiquitous, submesoscale turbulence is difficult to detect with most observational platforms due to limited resources, remoteness, and the ephemeral nature of submesoscale currents McWilliams (2016); D'Asaro et al. (2011); D'Asaro et al. (2018). Lagrangian instruments are well suited for this purpose because they approximately follow currents at depth Riser (1982); Davis (1991b) and at the surface Novelli et al. (2017) on submesoscale timescales, and thus targeted deployments of Lagrangian instruments are capable of capturing the spatiotemporal evolution of the fronts, eddies, and filaments associated with the submesoscale.

Drifters provide a low-cost measurement platform with the potential for high-resolution in both space and time, but they have a tendency to cluster in regions of convergence associated with horizontal density gradients and positive vorticity Choi et al. (2017); D'Asaro et al. (2018); Pearson et al. (2019); Chang et al. (2019). Numerical simulations of the Northern Gulf of Mexico by Choi et al. (2017) and Pearson et al. (2019) show that impacts of this biased sampling on turbulence statistics are strongest in the submesoscale. At scales less than 30 km, large releases of ∼30,000 synthetic drifters produced shallower second order structure functions and larger third order structure functions than Eulerian structure functions calculated using the model grid. Individual releases of clusters of synthetic drifters (∼300 - 1000) to emulate previous drifter launches in the Gulf of Mexico were also analyzed. The structure functions from cluster releases were similarly shallow and large for second- and third-order structure functions respectively but much more variable across scales. Divergence and vorticity structure functions suggest that coherent and correlated submesoscale features are responsible for different Eulerian and drifter statistics, findings that can now be verified with observations from the LAgrangian Submesoscale ExpeRiment (LASER) in winter of 2016.

LASER generated both Eulerian and quasi-Lagrangian surface velocity observations, in the form of shipboard X-band radar measurements Lund et al. (2018) and GPS-tracked drifters drogued at 60 cm Novelli et al. (2017); D'Asaro et al. (2018). The drifters are only 'quasi-Lagrangian' as they are confined to the surface and therefore do not capture the full three-dimensional velocity field in the true Lagrangian sense. Thus, throughout this paper "convergences" in the drifter trajectories do not imply three-dimensional convergence, only surface convergence. Simultaneous and co-located Eulerian and quasi-Lagrangian measurements are rare, and this is the first experiment we know of where the measurements are close enough and dense enough in space and time to provide comparable statistics. See Section 2 for more details.

Structure functions are a common tool for quantifying dispersion properties of fluid flows and placing the statistics into the context of turbulence theory. Following Pearson et al. (2019), differences between Eulerian and Lagrangian structure functions are investigated through an analysis of the impact of specific flow conditions on the statistics. These methods are described in Section 3.

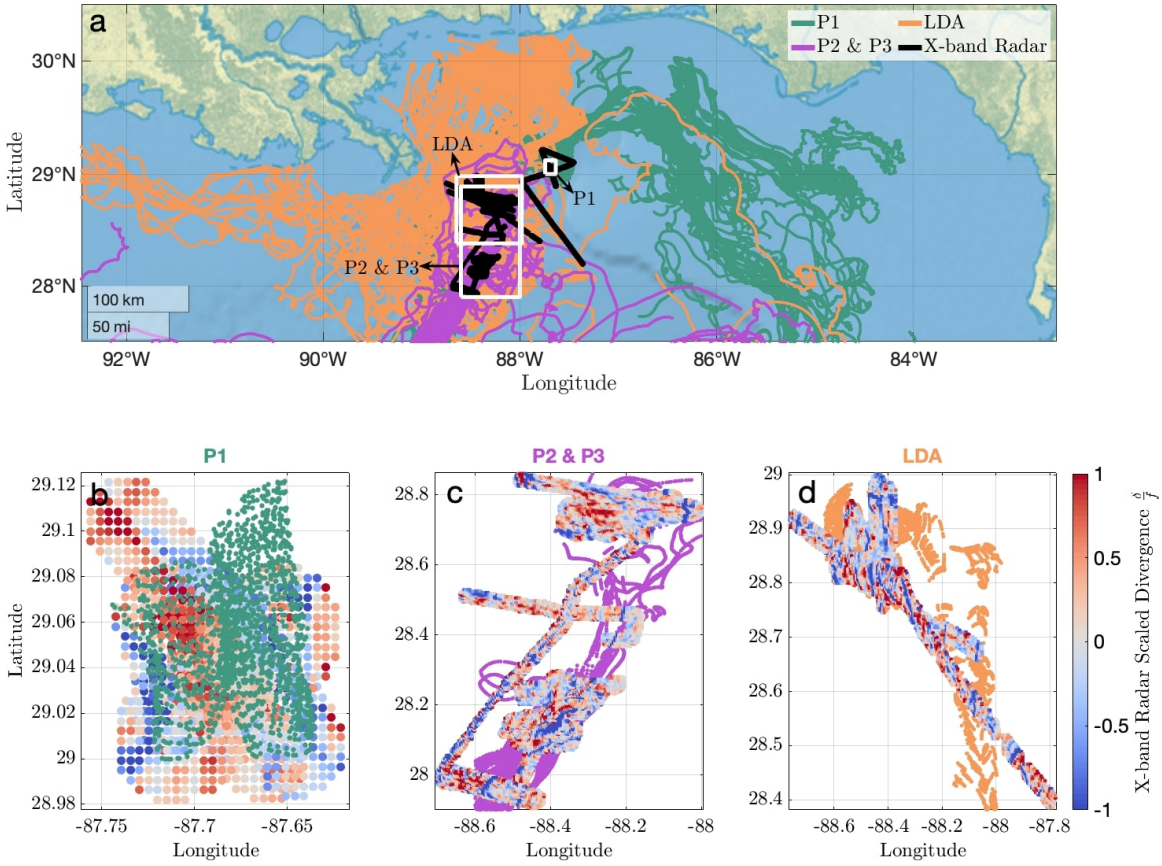

Figure 3.1: **(a)** Trajectories for the P1 **(green)**, P2 & P3 **(pink)** and LDA **(orange)** drifter deployments. The shiptrack X-band radar footprint is shown in black. To ensure the best overlap between the two datasets, the drifters and X-band measurements were analyzed only in the indicated domains and the time-frames shown in Table 1. **(b)** – **(d)** Scaled divergence δ/f from X-band radar for the time-frames and domains for **(b)** P1, **(c)** P2 & P3, and **(d)** LDA.

Section 4 describes the results, and discussion and conclusions follow in Section 5.

3.2 Data

3.2.1 LASER Drifters

Roughly one thousand GPS-tracked CARTHE-type surface drifters Novelli et al. (2017) were released in the Northern Gulf of Mexico as a part of the LAgrangian Submesoscale ExpeRiment (LASER) between 18 January and 13 February 2016 (see Figure 3.1(a)). These drifters were specifically engineered to be cheap, easy to assemble, and biodegradable to reduce pollution. They reported position data nominally every 5 minutes for several months and were drogued to follow the integrated flow of the top 60 cm of the water column Novelli et al. (2017). Tank experiments show the drifters are subject to less than 0.5% windage at 10-m wind speeds of 8 – 23 m/s Novelli et al. (2017). The

drifter trajectories were processed by removing outliers, low-pass filtering Yaremchuk and Coelho (2015) and interpolating positions to uniform 15-minute intervals. Some of the drifters lost their drogues during or following deployment, and the data following drogue-loss was discarded, based on the drogue-loss detection method of Haza et al. (2018).

To examine sampling bias caused by different local flow regimes, we consider separately three groups of observations, across four deployments (one group combines two deployments). The three groups are denoted 'P1', 'P2 & P3', and 'LDA'. P1 was a deployment of 300 drifters in a cloverleaf pattern over an 8 km x 8 km region with submesoscale activity and a modest horizontal density gradient, east of the freshwater front from the Mississippi River, on 21 January 2016. LDA was a deployment of 326 drifters on an approximately uniform grid over a 20 km x 20 km region targeting a vortex identified in satellite images and aerial sea surface temperature maps on 7 February 2016 (D'Asaro et al., 2018). This launch overlapped more substantially with the ship-track data than other available launches (see Figure 3.1). Lastly, P2 & P3 were distributed drifter releases from 25 January through 31 January 2016 (265 drifters in all) targeting submesoscale fronts, filaments, and Langmuir circulation. This group samples conditions when frontogenesis is the primary feature.

3.2.2 X-band Radar

A Doppler (coherent-on-receive) marine X-band radar developed by Helmholtz Zentrum Geesthacht (HZG), Geesthacht, Germany, was installed on the *R/V Walton Smith* in support of LASER. It consisted of a commercial GEM elettronica marine X-band (9.4 GHz) radar with a 2.3 m long HH-polarized antenna and a scanning period of 2 s. The antenna was situated at a height of ∼12.5 m above the sea surface with an unobstructed view in all directions. The radar transceiver operates with 12 kW output power and a pulse repetition frequency of 2 kHz in short pulse mode (i.e., a pulse length of 50 ns). The corresponding range and azimuthal resolutions are 7.5 m and 0.8°, respectively. The radar was modified by HZG to measure both intensity and phase of the radar backscatter signal from the sea surface Braun et al. (2008). The raw, uncalibrated radar measurements are linearly amplified and digitized at 20 MHz with 13-bit precision per channel. The A/D converter and amplifier are located inside the radar transceiver. The system samples the radar backscatter signal up to a maximum range of ∼3.1 km.

The X-band radar backscatter from the sea surface is due to a combination of Bragg scattering Barrick and Peake (1968); Wright (1968) and sea spikes associated with wave breaking Wetzel (1990); Trizna et al. (1991). This study uses near-surface current vectors derived from the long (>15 m) surface wave signal within the X-band radar backscatter intensity imagery. Surface waves appear as bands of enhanced and weakened backscatter primarily due to tilt modulation, i.e., wave-induced changes to the local incidence angle Lyzenga and Walker (2015); Støle-Hentschel et al. (2018). Additional wave imaging mechanisms are partial shadowing and hydrodynamic modulation Nieto Borge et al. (2004). The ship-motion-corrected and georeferenced radar backscatter intensity measurements were partitioned into evenly distributed and partially overlapping circular analysis windows with a radius of 480 m and 30 min periods, with the actual number of data points per

analysis window and period depending on the ship track. We note that smoothing from overlapping analysis windows lowers the total variability, and may affect scales below 1km. While comparison with tests from synthetic data suggests this contribution is likely small, a more detailed analysis of the effects of overlap size is necessary to account for the full effects and will be investigated in future studies.

Simultaneous georeferenced measurements in a field of view surrounding the ship allow the radar data to be interpreted as an Eulerian field of near-continuous observations. The methodology employed here is based on the well-established three-dimensional Fourier transform technique, which identifies the wave-related wavenumber-frequency coordinates within a radar image power spectrum, and then solves for the current vector by minimizing the wave coordinates' distance from the linear wave dispersion relationship Young et al. (1985); Senet et al. (2001). The effective depth of the resulting current vector depends on the lengths of the underlying surface waves Lund et al. (2015); Campana et al. (2017). Here, the currents are based on ocean wavenumbers ranging from 0.1-0.3 rad m^{-1}, which corresponds to an approximate effective depth of 1-5 m Stewart and Joy (1974). Based on a comparison between the X-band radar and CARTHE drifter measurements analyzed here, the X-band radar currents have an accuracy better than 0.04 m s^{-1} in terms of speed and 12° in terms of direction. For additional details on the X-band radar processing and validation, the reader is referred to Lund et al. (2018).

3.2.3 Data Windows

To ensure robustness of the statistics, windows in space and time were chosen that were densely sampled by drifters and the X-band radar. These are summarized in Table 3.1. The geographic domains for each launch group are shown in Figure 3.1. The drifter times were also constrained to match the time step of the Eulerian data by taking the nearest available drifter measurement for each Eulerian time-step. These data subsets were used for the structure function analysis presented in Sections 4.1 and 4.2.1. For the joint probability density function and structure function dependent on scale and divergence or vorticity presented in Section 4.2.2, all available X-band radar data was used covering the domain (lat $\in$ [27.9049, 29.2305], lon $\in$ [-88.7640, -87.3916]), time $\in$ [20 January 2016, 15:56:10, 12 February 2016, 19:40:50]). Additionally, the structure functions of both drifters and X-band radar were compared for two individual snapshots of a front on 31 January 2016, 12:16:19, and a vortex on 12 February 2016, 6:00:59.

3.3 Methods

3.3.1 Structure Functions

Velocity structure functions are the moments of velocity increments between two points, and provide information about the properties of turbulent dynamics at different scales. Given two drifters, the velocity components of interest are those projected onto the longitudinal (along-separation) and

Table 3.1: Data Windows

Launch	*Time-frame*	*No. Drifters*	*Features Sampled*
P1	21 January 2016, 13:51:04 to 21 January 2016, 19:08:39	300	submesoscale activity, modest density front
P2 & P3	26 January 2016, 00:16:44 to 01 February 2016, 19:40:23	197	submesoscale fronts, filaments, and Langmuir circulation
LDA	07 February 2016, 02:47:41 to 12 February 2016, 19:40:50	326	vortex

transverse (cross-separation) directions. If the positions of a pair of drifters are (x_1, y_1) and (x_2, y_2), then the horizontal separation vector between them is given as $\mathbf{r} = \Delta x\hat{\mathbf{i}} + \Delta y\hat{\mathbf{j}}$, where $\Delta x = x_2 - x_1$, $\Delta y = y_2 - y_1$. The drifter positions can be rewritten in terms of the separation vector, $\mathbf{r}$, by letting (x_1, y_1) correspond to $\mathbf{x}$ and (x_2, y_2) correspond to $\mathbf{x}+\mathbf{r}$. The longitudinal velocity increment is the projection of $\Delta\mathbf{u} = \mathbf{u}(\mathbf{x}+\mathbf{r}) - \mathbf{u}(\mathbf{x})$ in the direction of $\mathbf{r}$, and given by $\Delta u_L = (\mathbf{u}(\mathbf{x}+\mathbf{r}) - \mathbf{u}(\mathbf{x})) \cdot \hat{\mathbf{r}}$. The transverse velocity increment is perpendicular to both $\mathbf{r}$ and the local vertical $\hat{\mathbf{k}}$, and is given by $\Delta u_T = \hat{\mathbf{k}} \cdot ([\mathbf{u}(\mathbf{x}+\mathbf{r}) - \mathbf{u}(\mathbf{x})] \times \hat{\mathbf{r}})$ or equivalently $\Delta u_T = (\hat{\mathbf{r}} \times \hat{\mathbf{k}}) \cdot (\mathbf{u}(\mathbf{x}+\mathbf{r}) - \mathbf{u}(\mathbf{x}))$. These increments are used to construct the isotropic and homogeneous n^{th}-order structure function, defined as

$$S_\gamma^n(r) = \langle (\Delta u_\gamma)^n \rangle \tag{3.1}$$

where $\langle \cdot \rangle$ is an ensemble, time, or spatial average, n is the order of the structure function (or equivalently the n^{th} raw statistical moment of the velocity increment field), and γ refers to the velocity components (either longitudinal (L) or transverse (T)).

While Eq. 3.1 can be constructed with any value of n, it is the second- and third-order ($n = 2, 3$) structure functions that are most commonly analyzed and relevant in turbulence studies. Note that the higher the moment, the more sensitive it is to the tails of the distribution. Thus, with limited sampling the higher-order statistics are noisier and harder to estimate than the lower-order statistics. The second-order structure function, which is the variance of the velocity increments, is related to the kinetic energy spectrum through a Fourier cosine transform Webb (1964). This results in a linear relation between the respective slopes of structure functions and spectra McCaffrey (2015b), provided the spectral slopes fall between -1 and -3 Babiano et al. (1985). Spectral power law predictions for different turbulent regimes can therefore be transcribed to make structure function predictions for these regimes Bennett (1984); Babiano et al. (1985); LaCasce (2008); Callies and Ferrari (2013), even when multiple power laws are present at different scales as is sometimes the case for geophysical flows Frehlich and Sharman (2010); McCaffrey (2015a); Pearson et al. (2019). In this paper guidelines comparing theoretical structure function slopes for particular classical cascade theories will be provided by dashed gray lines alongside observed structure functions, but these are provided only for reference: power spectra are poorly constrained by drifters LaCasce (2016). We evaluate the biases of structure functions regardless of whether conversions between spectra and structure functions are possible (per Babiano et al., 1985). Third-order structure functions may

offer information about energy transfer between scales, and when paired with first- and second-order structure functions provide a more complete classification of turbulence statistics. The details of relevant third-order structure function theories can be found in Lindborg (1999, 2007); Poje et al. (2017); Pearson et al. (2019).

In homogeneous flows, statistics do not vary from location to location. This implies the mean velocity must be constant and there are no mean gradients of scalars or vectors in the flow. Consequently, the first-order structure function is zero. As a result there is no distinction between the *central* moments and the *raw* moments of the velocity increments as calculated using Equation 3.1 for homogenous turbulence. In isotropic turbulence, the statistics have no preferred directionality, implying there can be no mean vectors. With this restriction even a constant mean velocity is disallowed.

However, in observed flows a Reynolds decomposition (where $\mathbf{u} = \langle \mathbf{u} \rangle + \mathbf{u}'$, $\langle \mathbf{u}' \rangle = 0$, and $\langle ... \rangle$ is an ensemble, space, or time average) is often assumed where the background flow is generally nonzero and not uniform, and thus not homogeneous or isotropic. Due to these variable flow properties, the first-order structure function of the total velocity (background plus perturbation) calculated using Equation 3.1 is expected to be nonzero. For example, when the longitudinal first-order structure function is positive, the background flow has mean divergence. Similarly, a positive transverse first-order structure function implies a counter-clockwise background flow. If the first-order longitudinal and transverse structure functions are negative, it indicates a background flow with average convergence and clockwise rotation, respectively. Figure 3.2 illustrates these kinematic effects. Note that in the general definition, $\Delta u_{\gamma_1} = u_{\gamma_2} - u_{\gamma_1}$, where γ is any velocity component, and we wish to evaluate the effect on the longitudinal (u_L) and transverse (u_T) components through projection of the Cartesian meridional (u_y) and zonal (u_x) velocities given as $\Delta u_L = (\Delta u_x \Delta x + \Delta u_y \Delta y)/r$ and $\Delta u_T = (-\Delta u_x \Delta y + \Delta u_y \Delta x)/r$.

Under a Reynolds decomposition the first-order structure function calculated by Equation 3.1 is related algebraically to the second- and third-order statistics by

$$\begin{aligned}
\left\langle (\Delta u_\gamma)^2 \right\rangle &= \left\langle \langle \Delta u_\gamma \rangle^2 + 2 \langle \Delta u_\gamma \rangle \Delta u'_\gamma + (\Delta u'_\gamma)^2 \right\rangle \\
&= \langle \Delta u_\gamma \rangle^2 + \left\langle (\Delta u'_\gamma)^2 \right\rangle
\end{aligned}$$

$$\begin{aligned}
\left\langle (\Delta u_\gamma)^3 \right\rangle &= \left\langle \langle \Delta u_\gamma \rangle^3 + 3 \langle \Delta u_\gamma \rangle^2 \Delta u'_\gamma + 3 \langle \Delta u_\gamma \rangle (\Delta u'_\gamma)^2 + (\Delta u'_\gamma)^3 \right\rangle \\
&= \langle \Delta u_\gamma \rangle^3 + 3 \langle \Delta u_\gamma \rangle \left\langle (\Delta u'_\gamma)^2 \right\rangle + \left\langle (\Delta u'_\gamma)^3 \right\rangle \\
&= \langle \Delta u_\gamma \rangle^3 + 3 \langle \Delta u_\gamma \rangle \left[\left\langle (\Delta u_\gamma)^2 \right\rangle - \langle \Delta u_\gamma \rangle^2 \right] + \left\langle (\Delta u'_\gamma)^3 \right\rangle \\
&= 3 \langle \Delta u_\gamma \rangle \left\langle (\Delta u_\gamma)^2 \right\rangle - 2 \langle \Delta u_\gamma \rangle^3 + \left\langle (\Delta u'_\gamma)^3 \right\rangle
\end{aligned}$$

Thus, when the perturbation statistics are subdominant, the nonzero first-order structure function can determine the sign and magnitude of the third-order structure function (if the first terms on the

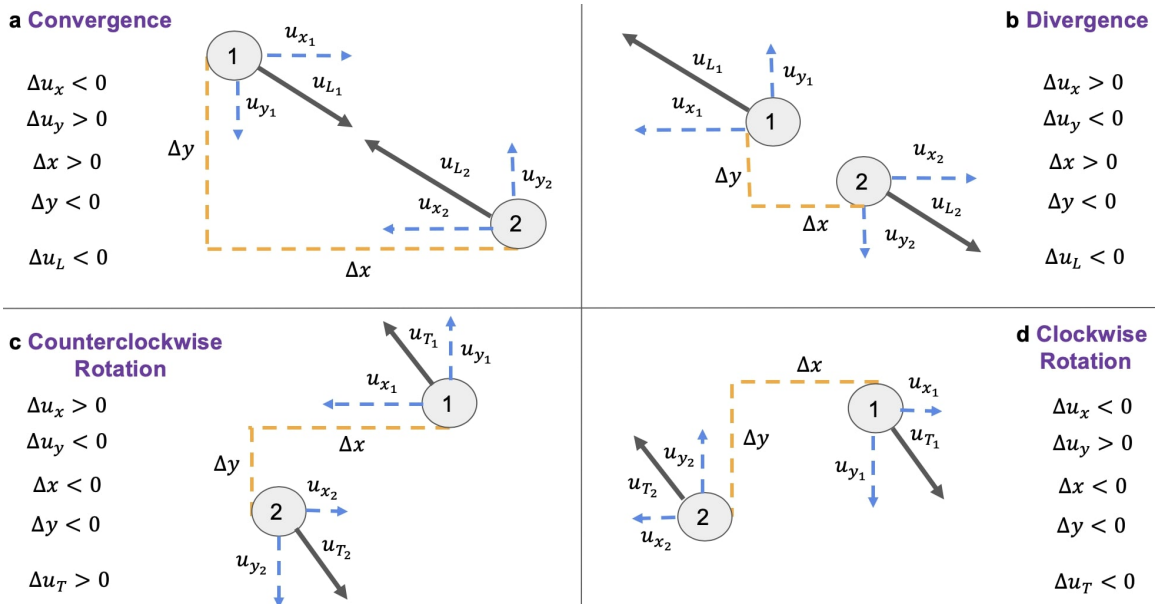

Figure 3.2: Demonstration of the relationship between the first-order structure function and drifters subject to **(a)** convergent flow, **(b)** divergent flow, **(c)** counterclockwise rotation, and **(d)** clockwise rotation. When subtracting the variables of the second drifter from the first (an arbitrary choice), the sign of the first-order structure function is determined. The signs of the differences that go into forming the $S_L^1 = \langle \Delta u_x \Delta x + \Delta u_y \Delta y \rangle$ and $S_T^1 = -\Delta u_x \Delta y + \Delta u_y \Delta x$ are provided.

right side are much larger than the second), and can determine the magnitude of the second-order structure function. In this paper, these effects are termed *background biases*, to indicate that the background flow biases the uncorrected structure function statistics. To isolate the central (i.e., with the mean removed) moments when the mean increment is non-zero due to background flow, the *corrected structure function*, $S_\gamma^{n'}(r) = \left\langle (\Delta u'_\gamma)^n \right\rangle$, is defined by the following equations to find the centralized distributions for the perturbation field statistics, which may then be potentially homogeneous and isotropic even if the background flow is not,

$$S_\gamma^{2'}(r) = \left\langle (\Delta u_\gamma)^2 \right\rangle - \left\langle \Delta u_\gamma \right\rangle^2 = S_\gamma^2(r) - \left[S_\gamma^1(r) \right]^2 \tag{3.2}$$

$$S_\gamma^{3'}(r) = \left\langle (\Delta u_\gamma)^3 \right\rangle - 3 \left\langle \Delta u_\gamma \right\rangle \left\langle (\Delta u_\gamma)^2 \right\rangle + 2 \left\langle \Delta u_\gamma \right\rangle^3 = S_\gamma^3(r) - 3 S_\gamma^1(r) S_\gamma^2(r) + 2 \left[S_\gamma^1(r) \right]^3 \tag{3.3}$$

The use of a Reynolds decomposition implies that there is a meaningful dynamical distinction between the background and perturbation fields. The further assumption that the energy transfer across scales is dominated by the perturbations, justifying the focus on the second- and third-order statistics of the perturbation fields (without the mixed background-perturbation and background-background nonlinear interaction terms) also implicitly assumes a scale, organizational, or amplitude separation between the mean and the perturbation fields. The idealization in this approach, then, is

similar to that used in boundary layer turbulence, where mean shear leads to shear production energizing the perturbation fields which then transfer energy across scales, but that the transfer across scales of the mean field by the mean field is negligible. If this assumption holds, then the standard derivations of the energy transfer terms via the Karman-Howarth equation (e.g Kolmogorov, 1941b; Frisch, 1995) are readily constructed from the perturbation equations instead of the total equations, retaining the background-perturbation shear production terms as a source in the perturbation equations (and a sink in the background equations) and assuming the background-background interactions are negligible in transfers across scales. Alternatively, one might choose not to distinguish between background and perturbation fields and using the total flow structure function. However, as the background field is neither homogeneous nor isotropic, this limits the applications of this approach. For example, the Karman-Howarth equation that relates the structure functions to the energy transfer across scales fails at the outset when considering heterogeneous, isotropic structure functions. The total flow structure function may be useful as a statistical descriptor of the flow (albeit a very high dimensional one), but most existing theory cannot be reconciled with this statistic. Frisch (1995) notes that there is an anisotropic generalization of this the Karman-Howarth equation in earlier works by Monin and Yaglom, but pursuing this approach is not feasible with the limited set of observations here.

3.3.2 Computational Details

At each time a structure function is found across all available scales. This is accomplished by binning the velocity increments from individual pairs at the given time-step into logarithmically defined separation scale bins with width 0.2 and averaging over all pairs in each bin. For data windows with multiple time-steps, these structure functions were then averaged over time, excluding any bin with less than 10 measurements to ensure the robustness of the statistics. The 95% bias corrected and accelerated confidence interval of the time-mean is found by bootstrapping with 10,000 resamples. For the specific snapshots of a front (Sections 4.2.3 and 4.3.3) and vortex (Sections 4.3.4 and 4.3.4), the structure function at the single time-step is calculated across all scales and binned in the same fashion, except that no time-averaging is done and the bootstrapped bias corrected and accelerated confidence intervals are found using all the data at each scale from the single time-step with 10,000 resamples. For the joint probability distributions and the structure function dependent on divergence and vorticity (sections 3.4.2 and 3.4.3), divergence and vorticity are given by the two-point (pairwise) average of the single-point divergence and vorticity values for each value within a pair.

3.4 Results

3.4.1 First-Order Structure Functions

The first-order velocity structure functions (denoted S^1_γ) are plotted in the upper panels of Figure 3.3. A detectable background flow is indicated by non-zero values in either the longitudinal or transverse

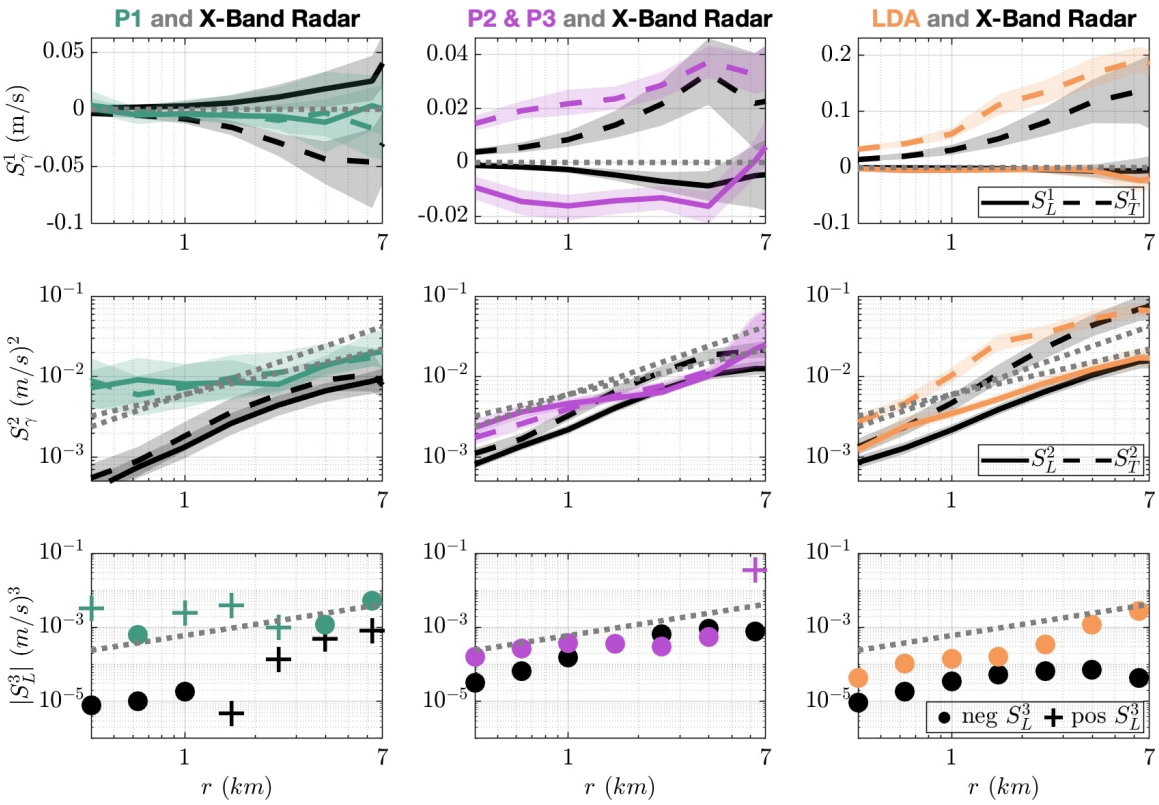

Figure 3.3: The **(top row)** first-order and **(middle row)** second-order longitudinal *(solid)* and transverse *(dashed)* velocity structure functions, and **(bottom row)** the absolute values of negative *(circle)* and positive *(plus)* third-order longitudinal velocity structure function values for the P1 *(left)*, P2 & P3 *(middle)*, and LDA *(right)* launches. The drifter deployments are given by the colored lines and symbols and the corresponding Eulerian X-band radar data by the black lines and symbols. Bootstrapped 95% bias corrected and accelerated confidence intervals for the time mean of the first- and second-order structure functions are provided as shading around each line. Dashed gray guidelines through zero are shown in the upper panels. Dashed gray guidelines for the middle panels correspond to theoretical second-order structure function slopes in 3D (2/3) and frontogenesis or an internal gravity wave field (1). A guideline of slope 1 is also shown for the lower panels for the linear slope of the 3rd order structure function predicted in the energy cascade region of 3D, 2D, or QG turbulence. Notice the difference in the y-axes for the first and third-order structure functions.

components for all samples, except the P1 drifters. Unlike the other deployments, these were not targeted at a strong flow feature, and because of the relatively short sample window for P1 (see Table 3.1), the drifters did not converge on an individual flow feature, resulting in more homogeneous sampling.

The only drifter deployment that shows a statistically significant non-zero longitudinal first-order structure function is P2 & P3, which was intentionally launched to sample frontal regions: S_L^1 is generally negative, though small, suggesting convergence. For 6.4 km and above, however, it is positive, indicating divergence. The change in sign identifies a scale at which drifters no longer cluster but are drawn into neighboring convergence zones. See also the related discussion in Section

4.2.3, which presents results on a single front with no accompanying sign-change in S_L^1.

Both P2 & P3 and LDA drifters show a positive S_T^1 across all scales, indicative of counter-clockwise rotation. For P2 & P3, S_T^1 is small compared to LDA. The larger values for the LDA drifters reflect the targeted vortex structure. Individual drifter tracks also trace out the counter-clockwise vortex of LDA repeatedly, resulting in loops (cf. Griffa et al., 2008).

In the first-order velocity structure function, quasi-Lagrangian and Eulerian statistics are overall consistent, with a few exceptions in the P1 domain. The X-band radar yields positive S_L^1 for scales above 4 km, consistent with the strong divergence seen in the domain given in Figure 3.1(b). Eulerian S_T^1 for scales between 1 km and 6 km is negative, making this the only dataset where clockwise vorticity dominates on average. These discrepancies within the smallest domain, where sampling by both drifters and X-band radar appears to be spatially most uniform (Figure 3.1), points to the challenges with obtaining unbiased samples.

3.4.2 Second-Order Structure Functions

The second-order velocity structure functions are plotted in the middle row of Figure 3.3. Pearson et al. (2019) found that the second-order structure function slopes derived from a large gridded synthetic drifter release in a model were on average shallower than the Eulerian structure functions computed on the model grid on scales below 10 km. The authors attribute this shallowness to over-sampling of convergence regions, consistent with previous studies Choi et al. (2017); D'Asaro et al. (2018). The results in Figure 3.3 (middle row) compound the *accumulation* bias from drifters over-sampling convergent regions with the *background* bias from non-zero first-order structure functions, shown in both Eulerian and quasi-Lagrangian structure functions, particularly in the transverse component. Here the compounded effects of both biases are discussed, and in the following two sections the effects of the background and accumulation biases will be isolated and discussed.

The Eulerian second-order structure functions, both transverse and longitudinal, are similar across all three sampling windows, with slopes around 1 or somewhat steeper. Only in the LDA sampling period is the transverse component noticeably steeper than the longitudinal component. Such steep slopes are consistent with the model results for Eulerian statistics of Pearson et al. (2019). The results for the quasi-Lagrangian calculations are not as consistent. P2 & P3 and LDA drifters exhibit slopes in both transverse and longitudinal second-order structure functions around 2/3, thus somewhat shallower than the Eulerian estimates and consistent with the preferential sampling of convergence zones by these drifters. However, P1 drifters show very little scale-dependence at all, much different than the slope of 2/3 found in Pearson et al. (2019), and likely due to the small window of time and spatial domain considered here. The disconnect between drifter-derived and radar-derived second-order structure functions for P1 demonstrates that the more uniform sampling in space by the drifters does not suffice to emulate Eulerian sampling, nor does a short time window.

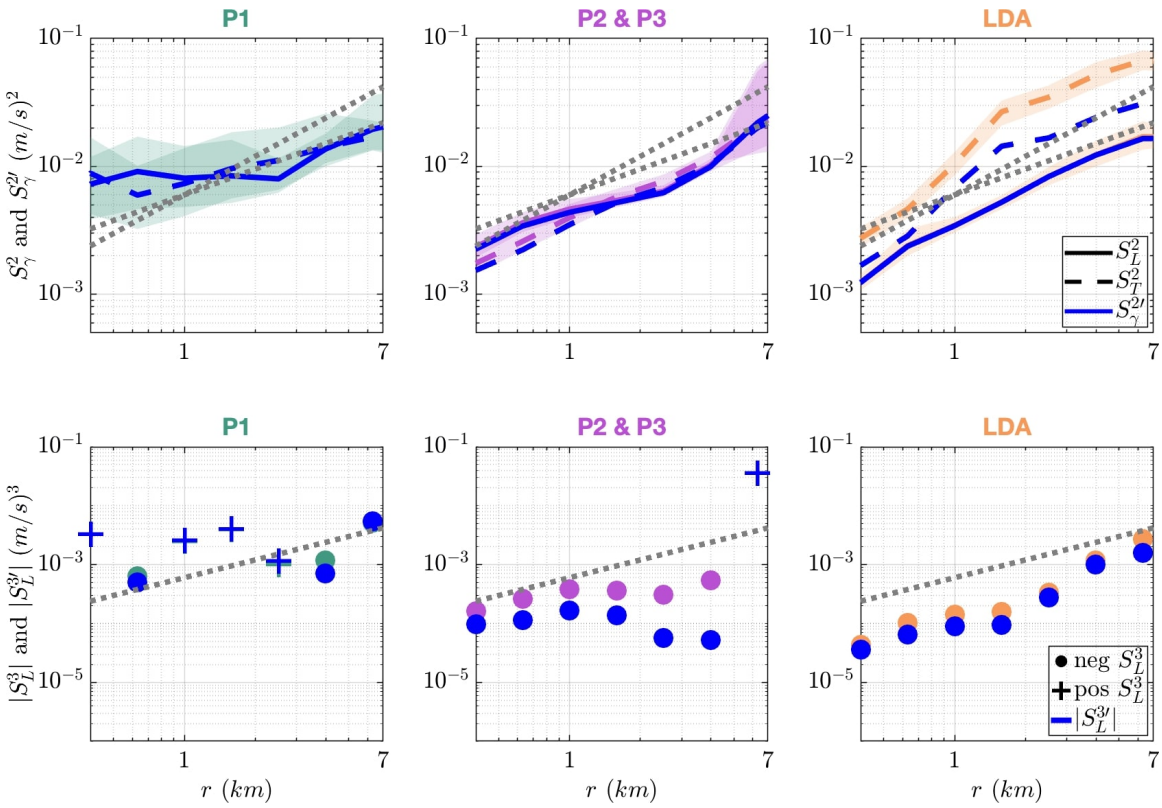

Figure 3.4: The quasi-Lagrangian second-order **(upper row)** and third-order **(lower row)** structure functions (green, pink, and orange) and corrected structure functions (blue) from P1 **(left)**, P2 & P3 **(middle)** and LDA **(right)** drifter data. Confidence intervals and guidelines are the same as in Figure 3.3.

Corrected Second-Order Structure Functions

The second-order structure functions corrected for background bias, $S_\gamma^{2'}$, (cf. equations (4.10) – (3.3)) are plotted in blue in the upper panels of Figure 3.4 and Figure 3.5 alongside the uncorrected structure functions with matching line styles. Most of the second-order corrected and uncorrected structure functions agree within uncertainty intervals, indicating a negligible background flow effect within the limits of detection of our method. The exceptions are the LDA launch, where the quasi-Lagrangian transverse second-order structure function is reduced in magnitude well outside the confidence intervals of S_T^2 and the Eulerian one lies at the outer limit of the confidence interval. Thus, ignoring the background flow for the longitudinal second-order structure functions may be appropriate in ocean surface submesoscale flows, but the transverse structure functions are more prone to bias from background flow effects.

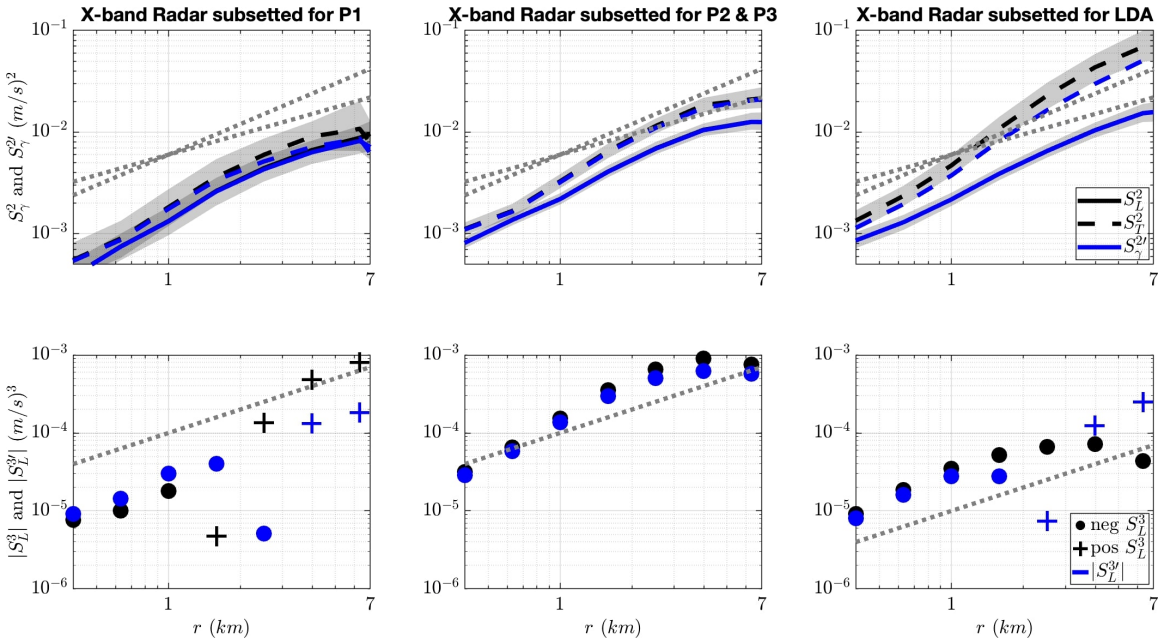

Figure 3.5: The X-band second-order **(upper row)** and third-order **(lower row)** structure functions (black) and corrected structure functions (blue) in the P1 **(left)**, P2 & P3 **(middle)**, and LDA **(right)** domains. Confidence intervals and guidelines are the same as in Figure 3.3.

S_γ^2 as a Function of Divergence and Vorticity

The differences between the quasi-Lagrangian and Eulerian structure functions are not predominantly due to the background bias, an effect of mean divergence or vorticity, as established above. The features oversampled by the drifters (e.g. fronts, vortices) must have fundamentally different structure functions than the domain as a whole, amounting to an accumulation bias. To further diagnose this accumulation bias, we investigate how S_γ^2 varies with divergence and vorticity. For this purpose, the complete time-series of Eulerian radar data (see Section 2.3) is analyzed. The (uncorrected) second-order structure function is computed as a function of both separation distance r and divergence ($S_\gamma^2(r,\delta)$), then of r and vorticity ($S_\gamma^2(r,\zeta)$). The uncorrected structure function values were chosen in lieu of the corrected values for direct comparison with other uncorrected structure functions in the literature (including the results of Pearson et al. (2019)), as well as the relatively small first-order structure function dependent on separation from all available X-band measurements (not shown). This is complimentary to the results of Figure 3.5, where the correction for X-band measurements is generally within confidence intervals of the uncorrected structure functions even for subsetted data.

Figure 3.6 shows the results in the yellow-blue colored field. Overlaid with black-white contours are the joint probability density functions (JPDFs) of divergence and separation distance (top) and of vorticity and separation distance (bottom) to show the sampling distribution. Similar to the structure functions of specific launches (Figure 3.3), both $S_\gamma^2(r,\delta)$ of the upper panels and $S_\gamma^2(r,\zeta)$

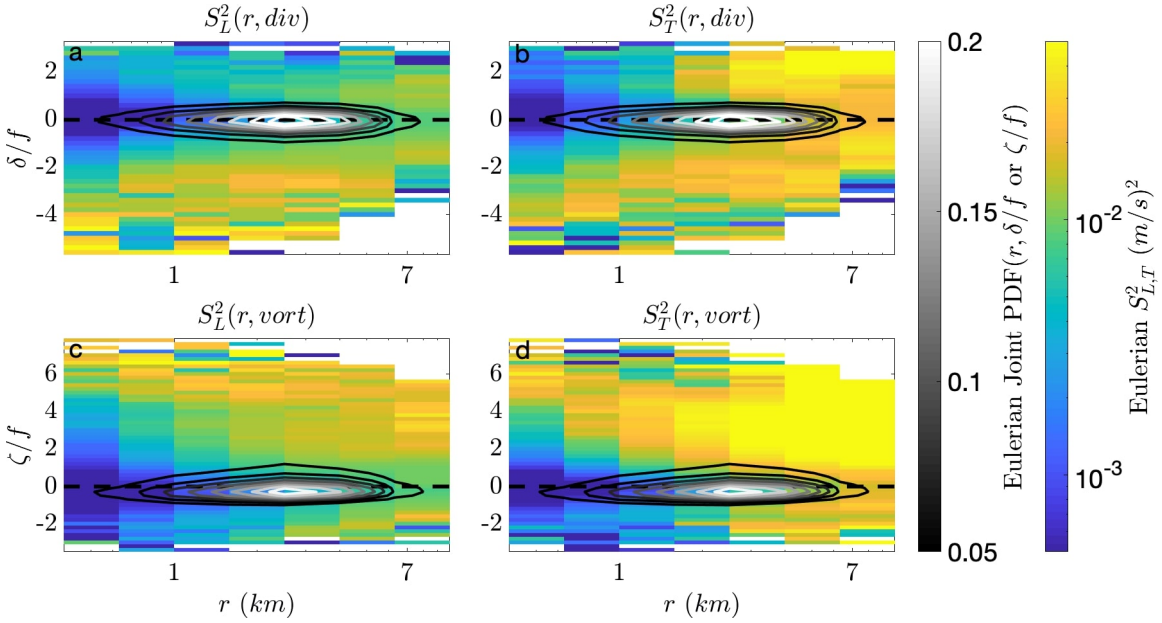

Figure 3.6: Eulerian longitudinal **(a,c)** and transverse **(b,d)** uncorrected second-order structure functions as a function of divergence and scale **(a,b)** and of vorticity and scale **(c,d)**, denoted by the blue to yellow logarithmic colormap. The joint probability density function of divergence and separation distance **(a,b)** and vorticity and separation distance **(c,d)** is shown by contours colored using the black to white colormap. Both divergence and vorticity are scaled by the mean Coriolis parameter in the domain.

of the lower panels show strong dependence on separation distance r. This is especially true at the most frequently sampled Eulerian divergence and vorticity levels, highlighted by the maxima in the joint PDF. Based on the overlaps between the JPDF and the structure function values across scales, the Eulerian structure functions $S_\gamma^2(r)$ are expected to be steeply sloped. The panels also show that lower divergence and higher vorticity levels (from oversampling regions of strong convergence and counter-clockwise rotation) could lead to larger or shallower second-order structure functions.

Below two specific events are isolated that are characterized by significant convergence and vorticity, respectively. Such strong events are hypothesized to be the primary causes of the different slopes between Eulerian and quasi-Lagrangian structure functions, consistent with the findings of Pearson et al. (2019).

Biases in Second-Order Structure Functions at a Front

The statistics at a front, as observed concurrently on 31 January 2016 with X-band radar and some of the drifters launched during the P2 & P3 deployments, are presented in Figure 3.7. The front itself is characterized by a strong convergence region near the center of the domain (Figure 3.7a), as indicated by the blues in the Eulerian divergence field, which reaches values around $-2f$. This convergence can also be detected in the drifter velocity field (pink arrows) and in the drifter distribution itself, with many drifters drawn into the frontal region. The western side of the front shows positive vorticity

(Figure 3.7b), with values up to $2f$, while weaker negative vorticity dominates the eastern side. The quasi-Lagrangian first-order structure functions are both significantly different from zero and larger than for the full P2 & P3 dataset (cf. Figure 3.3). The signs reflect the drifters' preferential sampling of negative divergence and positive vorticity nearly equally across all scales, consistent

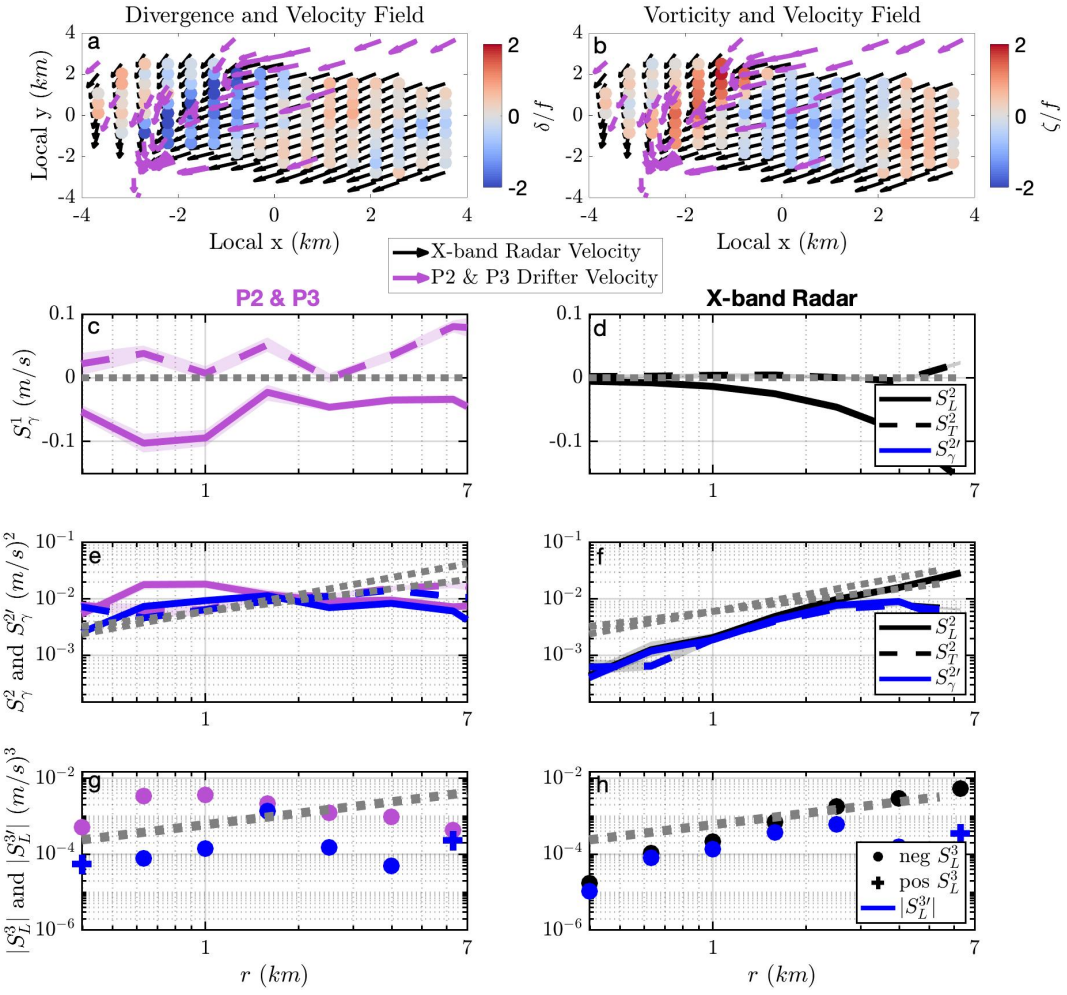

Figure 3.7: **(a)** The velocity and divergence fields at a front on 31 January 2016 at 12:16:19 UTC. Eulerian velocities are given by black arrows, and the P2 & P3 velocities by the pink arrows. Underlain is the Eulerian divergence field scaled by f. **(b)** Same as (a) but with the scaled vorticity field instead of divergence. P2 & P3 drifter (left) and corresponding X-band (right) **(c, d)** first-order, **(e, f)** second-order, and **(g, h)** third-order structure functions. The corrected second- and third-order structure functions are given by the blue markers in **(e)**–**(h)**. Negative and positive values for the third-order structure functions are plotted with dots and pluses, respectively. The 95% bias corrected and accelerated confidence intervals are shown with shading. Note that these confidence intervals are formed from the mean value at a given scale for this particular snapshot. Guidelines are the same as in Figure 3.3.

with Figure 3.7a and b. The Eulerian field extends farther away from the front than the drifter samples and thus incorporates regions of quite weak divergence and vorticity (Figure 3.7a and b). This leads to the Eulerian S_T^1 being indistinguishable from zero, except at the largest scale. The Eulerian S_L^1, on the other hand, is only near-zero for small scales and significantly negative at large scales (Figure 3.7c). This is a result of the presence of relatively strong negative divergence in the domain, east of the front, while any positive divergence in the domain is weak (Figure 3.7a and b).

As previously seen in Section 3.4.2 for the larger sample domains, the background bias correction does not significantly alter the second-order structure functions, except at the largest scales, which may not be sampled sufficiently. Both longitudinal and transverse S_γ^2 are nearly flat for the drifter data (Figure 3.7e) — in contrast to the statistics for the full P2 & P3 domain (Figure 3.4). The Eulerian S_γ^2, on the other hand, exhibit slopes comparable to those from the full P2 & P3 domain (Figure 3.5), and are therefore much steeper than the quasi-Lagrangian statistics observed directly at the front.

These results are consistent with the discussion in Section 3.4.2, considering the divergence and vorticity values being sampled. Figure 3.6a and b shows that S_γ^2 at an average divergence around $-2f$ should be relatively flat, although Figure 3.6c and d suggest that for vorticity values near $2f$, lower values are expected at the small scales for S_L^2 and to a lesser degree also for of S_T^2. The lack of a slope at small scales in the frontal data indicates that the presence of strong divergence dominates the vorticity in the second-order structure function. Since the small scales of the X-band radar data are less biased toward strong convergence and not biased toward positive vorticity (as is seen both in Figure 3.7a and b and in the Eulerian S_γ^1), the same flattening of the S_γ^2 slopes is not observed in the Eulerian statistics. This is an illustration of the strong impact the accumulation bias in the drifter data can have on the statistics.

Biases in Second-Order Structure Functions in a Vortex

Figure 3.8 illustrates a different event: a vortex sampled with X-band radar and some of the drifters from the LDA deployment on 12 February 2016. The vortex is characterized by strong positive vorticity everywhere, reaching values up to $4f$ (Figure 3.8b). While the domain is generally marked by weak divergence (less than $1f$), it contains small pockets of stronger positive divergence (up to $3f$); see Figure 3.8b. The sampling by the drifters is strongly non-uniform and takes the shape of a counter-clockwise spiral into the vortex.

Figure 3.8c and d, showing the first-order structure functions, suggest that both the X-band radar and drifters tend to sample larger divergence and vorticity at larger scales. Unlike in the frontal example, the corrections for non-zero S_γ^1 to S_γ^2 are significant for the transverse components. Note that S_T^1 is 2 to 3 times larger here than either S_T^1 or S_L^1 near the front. The impact of background bias on the slope is not clear for the drifters, but appears to be flattening for the Eulerian data.

As before, the variability of S_γ^2 as a function of vorticity and divergence examined in Section 3.4.2 can link the observed slopes to an accumulation bias. The increasing vorticity sampling with increasing scale suggests a diagonal cross-section through the fields in Figure 3.6c and d is appropriate, from

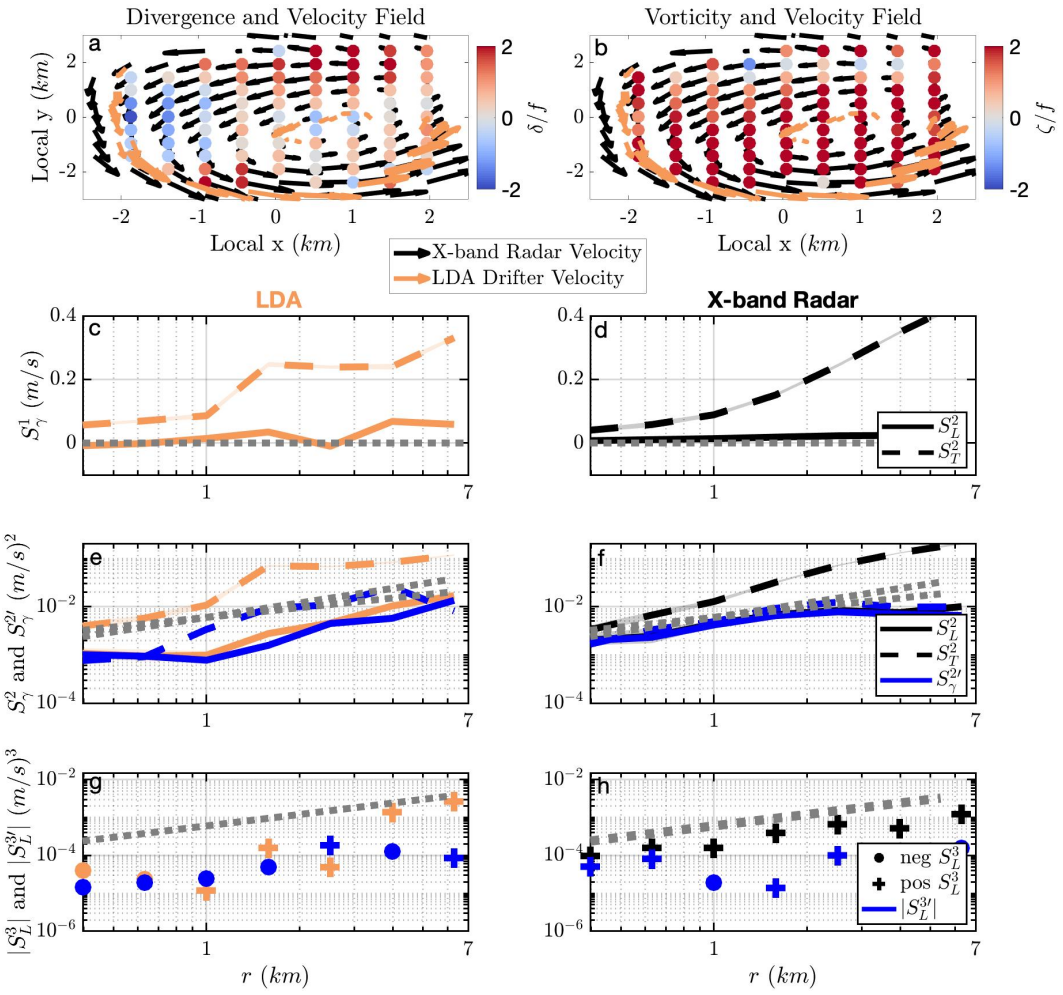

Figure 3.8: Same as Figure 3.6 but for data from a vortex on 12 February 2016 at 6:00:59 UTC, using LDA drifters instead of P2 & P3 drifters.

the left just above zero to the top right, or from low to high S^2_γ values. The increasing divergence sampling with increasing scale reinforces this pattern. Note that the drifters are not in an obvious convergence region in this sample. Nonetheless, the non-uniform sampling of vorticity produces an accumulation bias effect. It is, therefore, important to keep in mind over what variety of flow fields the structure functions are computed when interpreting them.

3.4.3 Third-order Structure Functions

The third-order longitudinal structure function, S^3_L, is plotted in the lower panels of Figure 3.3 for the drifters and the X-band radar data available during each launch. In contrast to the second-order structure function, the third-order structure function is not positive definite, so the absolute

value is plotted with symbols denoting negative (•) or positive (+) values. Confidence intervals are not plotted, but the quasi-Lagrangian estimates fall mostly outside the 95% confidence window for Eulerian data below 2 km for P1, and P2 & P3. The exception is the LDA deployment, for which only the largest scale falls outside Eulerian confidence intervals. Even so, the LDA drifter S_L^3 exceeds the X-band radar S_L^3 by a factor of 3 to 5, especially over the middle range of scales where the structure functions tend to be most reliable due to adequate sampling. In terms of sign, both the quasi-Lagrangian and the Eulerian structure functions are consistently negative in the LDA domain. The same is true of the Eulerian S_L^3 in the P2 & P3 domain, but here the quasi-Lagrangian S_L^3 changes sign above 5 km. For P1, the Eulerian third-order structure function changes sign at about 1.5 km, but the drifter-based statistics do not have a single clear transition from negative to positive S_L^3. The slopes for the Eulerian estimates for P2 & P3 and for LDA are somewhat steeper than 1. S_L^3 of the corresponding drifter launches are more variable across scales, but the slope for the LDA launch is comparable, while that for P2 & P3 is shallower. These less than conclusive results limit the utility of using this statistic to diagnose energy flux across scales.

Corrected Third-Order Structure Functions

The corrections to the third-order structure function for the background bias proposed in equation (3.3) tends to be more substantial than that to the second-order structure function from equation (4.10), especially at larger scales, because it contains a term proportional to $S_\gamma^1 S_\gamma^2$. Consequently,

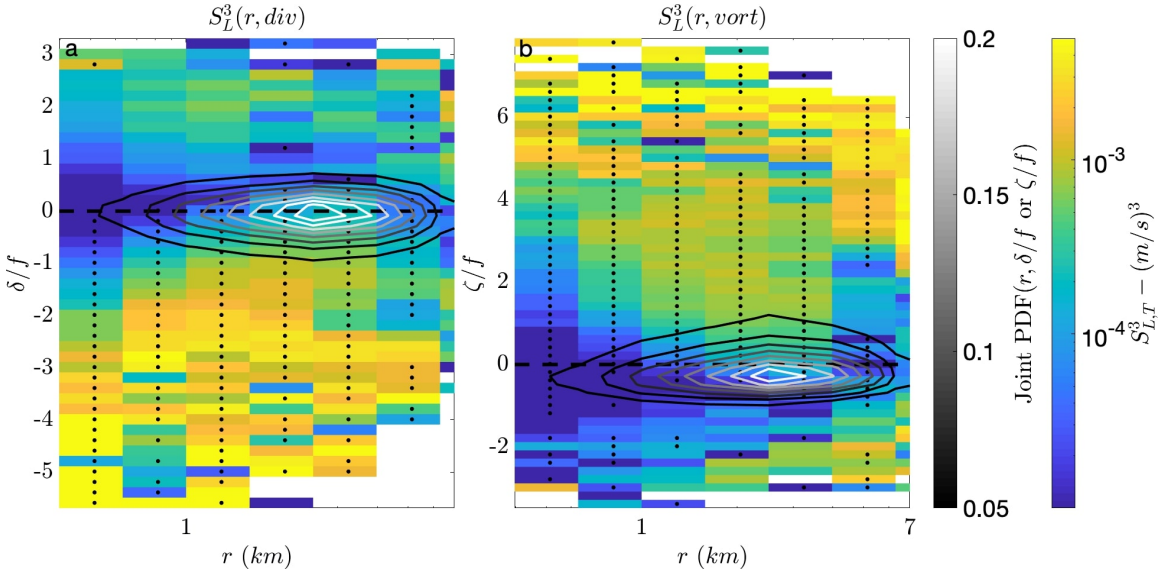

Figure 3.9: The absolute value of the Eulerian longitudinal *uncorrected* third-order structure function dependent on divergence and scale **(a)** and vorticity and scale **(b)**, denoted by the blue to yellow logarithmic colorbar. Negative values are stippled with a '•' and positive values are left un-stippled. The joint probability density function of divergence and separation distance **(a)** and vorticity and separation distance **(b)** is shown by contours and the black to white linear colorbar.

the sign and magnitude of the third-order uncorrected structure function is potentially dependent through background bias on the sign and magnitude of the first-order structure function. The corrected quasi-Lagrangian and Eulerian third-order structure functions, $S_L^{3'}$, are presented in Figure 3.4 and Figure 3.5, respectively. While the Eulerian $S_L^{3'}$ does not deviate much from the Eulerian S_L^3 for the P2 & P3 sample, its sign changes for scales above 1.5km in both the P1 and LDA samples. The quasi-Lagrangian $S_L^{3'}$ agrees in sign with the uncorrected S_L^3 for all estimates, but the magnitudes are lower for LDA and P2 & P3 (though not for P1) across almost all scales. Nonetheless, the corrected third-order structure functions fall inside the confidence intervals of the uncorrected third-order structure functions for both drifter and X-band data, with the exception of the P2 & P3 drifters, which fall outside across most scales, and P1 which does above 2 km. This is a consequence of the inherent noisiness of higher order statistics and illustrates the challenges of drawing reliable conclusions from the third-order structure function estimates from noisy observations.

S_γ^3 as a Function of Divergence and Vorticity

Mirroring the analysis in Section 3.4.2, the potential effect of accumulation bias on the third-order structure function is investigated by considering the absolute value of the uncorrected S_L^3 as a function of both scale and divergence ($S_L^3(r,\delta)$), and then of both scale and vorticity ($S_L^3(r,\zeta)$). See the yellow-blue colored fields in Figure 3.9a and b, respectively. Negative values are marked with black bullets. Overlaid with black-white contours are again the JPDF of scale and divergence (left) and of scale and vorticity (right). The distributions are, as expected, noisier than the corresponding results for S_L^2. Nonetheless, some broad patterns can be discerned. A gradient with respect to r exists for small values of divergence and vorticty where the bulk of the samples lie. Gradients with respect to δ and ζ also exist. Negative values of S_L^3 are associated with negative values of divergence and increase with increasing divergence, becoming positive except for a handful of bins with very high divergence, which are likely not sampled well. The transition point to positive values is scale-dependent. With respect to vorticity, negative values of S_L^3 are associated with positive vorticity and S_L^3 increasing as vorticity decreases. The transition to positive values is not as clear. The figure suggests that a disproportionate sampling of large convergence and/or positive vorticity is expected to flatten the slope and increase the magnitude of $S_L^3(r)$.

Biases in Third-Order Structure Functions at a Front

The third-order uncorrected and corrected structure functions at a front are plotted in Figure 3.7g and h. Note first that here the drifters and the X-band radar S_L^3 are significantly affected by nonzero S_L^1, which changes both the sign and magnitude of the third-order structure function across all separation scales. Unlike S_L^3 for the full P2 & P3 dataset (cf. Figure 3.4 and Figure Figure 3.5), the corrected third-order statistics for this frontal snapshot lie well outside the confidence intervals of the uncorrected S_L^3 across all separations except 1.5 km for the P2 & P3 drifters , and at all scales above 1 km for the X-band radar data (not shown). As observed in section 3.4.3, the strong convergence ($-2f$) and the high vorticity ($2f$) sampled by the drifters are both associated with

a flatter, negative S_L^3, which is seen in Figure 3.7g. As with the Eulerian S_L^2, sampling that is less biased toward high convergence and vorticity results in an S_L^3 that is comparable to that from the full P2 & P3 dataset (Figure 3.5) in slope, although with lower values across all scales.

Biases in Third-Order Structure Functions at a Vortex

The third-order uncorrected and corrected structure functions at a vortex are plotted in Figure 3.8g and h. As with the frontal case, sign and magnitude of both the drifters and the X-band radar S_L^3 are impacted across all separation scales by the correction for nonzero S_L^1. Additionally, the corrected S_L^3 are outside of the confidence intervals of the uncorrected S_L^3 above 1 km (not shown). As noted in section 3.4.2, the first-order structure functions indicate stronger vorticity and divergence being sampled at larger scales. Unlike for S_L^2, however, this sampling bias results in contradictory trends in S_L^3, as shown in Figure 3.9. The variability, particularly in sign, seen in Figure 3.8g and h may therefore be a consequence of the sampling biases.

3.5 Conclusions

Surface drifters are a powerful observational platform providing high spatial and temporal resolution hard to come by via other instrumentation to assess dispersion of floating material in the ocean. Previous studies suggest a key characteristic is that their sampling pattern is not agnostic to the flow properties, making such a quasi-Lagrangian velocity data set fundamentally different from an Eulerian one. In particular, Pearson et al. (2019) demonstrate that correlated divergence and vorticity lead to shallower second-order and larger third-order structure functions at scales below 30km. The second- and third-order structure functions presented here are shallower and larger respectively than the corresponding Eulerian statistics, consistent with the results of Pearson et al. (2019). Alongside validating the prevalence of the drifter biases in observations, this study builds upon the work of Pearson et al. (2019) by refining the impacts of convergence and vorticity on the second- and third order structure functions. The observational analysis highlights that the preferential sampling of convergence regions and areas with strong vorticity results in an *accumulation* bias. Its potential impact on structure function statistics can be determined by considering the statistics computed from an Eulerian velocity field as a function not just of separation scale but also of divergence or vorticity. We found that the steepest gradient as a function of r is associated with near-zero values of divergence and vorticity, which are also most commonly sampled by the Eulerian X-band radar along the shiptrack in our data. At stronger convergence, the S_γ^2 and S_L^3 show shallower slopes, as they increase more at smaller scales. Evidence of this effect is seen in the statistics of data subsampled specifically to coincide with a strong front. Similarly, high positive vorticity tends to increase the magnitudes of the structure functions and flatten them. This tendency can be identified in data subsampled in a strong vortex.

In classic turbulence theory, the flow is assumed to be statistically isotropic and homogeneous, so that the first-order structure function is zero for all scales. However, this assumption does not

hold in either the quasi-Lagrangian or the Eulerian observational data. This raises the question whether second- and third-order structure functions should be computed after the mean flow has been removed. Such a correction for *background* bias can have a great impact on the statistics. In particular, the sign and magnitude of the third-order structure function can be driven by the sign and magnitude of the first-order structure function, not the perturbations that are related to energy transfer across scales. The effect is smaller in the Eulerian data when sampled over a sufficiently large domain.

The sizable influence of these biases on the structure function statistics demonstrates that any interpretation or comparison must take the sampling schemes into account. In particular, it may not be appropriate to attempt to link third-order structure functions to energy fluxes, especially when based on drifter data that is almost invariably subject to both background and accumulation biases. While Eulerian measurements can be flow-independent by design, they, too, may be subject to background and sampling representativeness biases akin to accumulation biases, requiring caution even when deriving statistics from them.

The authors wish to thank the large team of scientists and support staff during the LASER campaign. This research was made possible in part by a grant from The Gulf of Mexico Research Initiative to the Consortium for Advanced Research on the Transport of Hydrocarbons in the Environment (CARTHE) and in part by grant N00014-17-1-2963 from the Office of Naval Research. Data are publicly available through the Gulf of Mexico Research Initiative Information & Data Cooperative (GRIIDC) at https://data.gulfresearchinitiative.org under DOIs 10.7266/N7N01550 (X-band radar) and 10.7266/N7W0940J (drifters).

Chapter 4

Benefits of the Bias: Corrected Estimates of Transport and Dispersion Parameters from Surface Drifter Observations

This chapter is in preparation for submission with lead author Jenna Pearson and coauthor Baylor Fox-Kemper. The objective of this chapter is to describe the impact of the turbulent velocity field on particle transport and dispersion. This section builds on the methods of Chapter 3 by applying a similar correction to second-order Lagrangian structure functions to account for heterogeneity and non-stationarity in the flow field due to both submesoscale and mesoscale features. Estimates are made of the absolute diffusivity from the Lagrangian structure functions, which describes the efficiency of turbulence at dispersing tracers in the ocean. These are analyzed alongside probability and travel time maps, with results spanning a wide range of applications to include coastal management, accident mitigation, and climate problems.

Abstract

Characterizing the mixing properties of the upper ocean plays a crucial role in understanding how buoyant material – like marine litter, plankton, and oil – spread and move throughout ocean basins. The influence of turbulent processes on the rate of particle dispersal in the Northern Gulf of Mexico is investigated by geographically mapping absolute eddy diffusivities estimated from surface drifters from the Grand LAgrangian Deployment (GLAD) of summer 2012 and the LAgrangian Submesoscale ExpeRiment (LASER) of winter 2016. The Lagrangian structure function is calculated to find the autocorrelation function, the integral of which is used to estimate the eddy diffusivity. A correction

method is applied to the Lagrangian structure function to remove the impacts of heterogeneity and non-stationarity, and the maps of the Lagrangian integral time and absolute eddy diffusivity are analyzed alongside probability and travel time maps. The GLAD and LASER drifters have vastly different sampling patterns, which is a reflection of the different forcing mechanisms during the sampling period. Maps of Lagrangian integral times and absolute eddy diffusivities are heterogeneous and anisotropic for both GLAD and LASER. Corrected estimates of both Lagrangian integral times and eddy diffusivities are 2-10 times larger than uncorrected estimates, and show different spatial structure. This suggests the importance of accounting for the effects of the mean flow when calculating turbulence statistics.

4.1 Introduction

The dynamics of the ocean manifest over a wide range of spatiotemporally varying motion, from ocean currents spanning thousands of kilometers down to centimeter dissipation scales. This includes eddies of various sizes (e.g. Chelton et al., 2007), where an "eddy" is defined here as a deviation from the mean flow. Mesocscale eddies, with length scales of 100s of kilometers and times scales of many days, play a large role in the physical transport and dispersal of heat, oil, marine litter, and other tracers (e.g. Bryden and Brady, 1989; McGillicuddy et al., 2007; Early et al., 2011; Van Sebille et al., 2012). In numerical models, an eddy diffusivity, analagous to molecular diffusivity, is often implemented to represent the unresolved and underesolved efficiency of lateral (or along an isopycnal or isoneutral surface at depth) transport from mesoscale eddies (e.g. Fox-Kemper et al., 2011; Bachman et al., 2015). Note here that eddies do not themselves mix tracers, but rather fold and strain tracer isolines, which initiates a spectral flux of tracer variance towards higher, dissipative, wavenumbers (Eckart, 1948; Batchelor, 1959; Solomon, 1971; Redi, 1982). Thus there is an adjustment time, which in the Lagrangian sense (i.e. following water parcels), means that only after the parcels have travelled a distance greater than the largest eddies of the flow is the transport meaningfully approximated as a diffusive process (Taylor, 1921; Klocker et al., 2012).

Many diffusion based parametrizations also conventionally assume constant and isotropic values for the diffusion parameters, as well as a constant background velocity, which is likely not suitable for the heterogeneous, intermittent, and anisotropic ocean (e.g. Freeland et al., 1975; Spall et al., 1993; LaCasce, 2000; LaCasce and Bower, 2000; Mariano et al., 2016; Kamenkovich et al., 2015; Rypina et al., 2016). Anisotropy, intermittancy, and heterogeneity are particularly prevalent in coastal oceans, where energy input from winds and tides compete with dissipation on the seafloor as well as along coastlines, and shallow flows feel the effects of, and respond to, varying bathymetry. The combination of these processes results in a complex set of multi-scale features that are notably different from most of the open ocean (Haidvogel et al., 2000; Simpson and Sharples, 2012; Orfila et al., 2014). In addition to intricate physics, many coastal oceans are often subject to large-scale inputs of pollution, for example the Deepwater Horizon oil spill of 2010 in the Gulf of Mexico (Crone and Tolstoy, 2010) or the Fukushima nuclear accident in 2011 off the eastern coast of Japan (Buesseler

et al., 2012). Here we focus on the Gulf of Mexico, and the main purpose of this work is to quantify the role of the eddying ocean in mixing particles and tracers, with results applicable to the accident mitigation, biogeochemical processes, and the climate system.

Transport and dispersion of buoyant material is naturally investigated in a Lagrangian framework, and surface drifters have been used to estimate absolute eddy diffusivities throughout the global ocean (e.g., Krauß and Böning, 1987; Davis, 1991b,a; Swenson and Niiler, 1996; Poulain, 2001; Lumpkin and Flament, 2001; Zhurbas and Oh, 2004; Sallée et al., 2008; Koszalka et al., 2011; Zhurbas et al., 2014; Peng et al., 2015; Mariano et al., 2016; Rypina et al., 2016). It is important to note that surface drifters are not purely Lagrangian, as they are buoyantly confined to the surface. However, many pollutants, such as oil, also remain concentrated near the surface and drifters are taken as surrogates in this context (e.g. Poje et al., 2014; Novelli et al., 2017; D'Asaro et al., 2018; Mariano et al., 2016; Huntley et al., 2019; Pearson et al., 2019, 2020). Throughout the paper, "Lagrangian" and "semi-Lagrangian" are used interchangeably, although the authors wish to make the distinction very clear here, with the former being the motion following the fluid and the latter being the motion of an observation that partly matches the fluid, such as a buoyant pollutant or drifter.

In the Gulf of Mexico, unprecedented numbers of surface drifters were released during the Grand LAgrangian Deployment (GLAD) of summer 2012 (Poje et al., 2014) and the LAgrangian Submesoscale ExpeRiement (LASER) of winter 2016 (Novelli et al., 2017; D'Asaro et al., 2018). Even with plentiful data, a number of difficulties arise under conventional methods of estimating the absolute eddy diffusivity in a Lagrangian framework. This includes (but is not limited to) the proper separation of the mean flow and eddy components (Griesel et al., 2014; LaCasce, 2008), as well as accounting for the different turbulent regimes sampled by drifters that lead to spatial variability of diffusivity estimates (Berloff and McWilliams, 2002; Koszalka et al., 2011; De Dominicis et al., 2012). The novelty of the methods developed in this study expand on previous methodology to address both of these issues parsimoniously by correcting for gradients in the mean flow as well as determining the optimal length of trajectory to be used in the initial calculations, both of which can have significant impacts on dispersion metrics (Taylor, 1953; Bennett, 1987; Young and Jones, 1991; LaCasce, 2008; De Dominicis et al., 2012; Nilsson et al., 2013).

Absolute eddy diffusivities are conventionally estimated with surface drifters by computing the correlation between the velocity and displacement (Davis, 1991b; Zhurbas and Oh, 2004), the absolute (single-particle) dispersion (LaCasce, 2008; Rypina et al., 2012; Kamenkovich et al., 2015), or integrating the velocity autocorrelation function (Davis, 1991b; Sallée et al., 2008; Griesel et al., 2010) of ensembles of Lagrangian particles. The latter is the choice of this paper, although there are several differences in our approach. First, the autocorrelation function is not directly computed, it is found through the relationship to the second-order Lagrangian structure function for stationary and homogeneous flows (Babiano et al., 1987), which is corrected to account for the effects of mean gradients in velocity along a trajectory. The correction is a combination of persistent Eulerian spatial gradients, as well as gradients due to the time dependence of the flow. Second, the length of integration is chosen as the last time when the integral is positive, as opposed to other methods such

as the "first zero-crossing method" (see Griffa et al. (2007) for a review). This choice is particularly suitable for the oscillatory autocorrelation functions found in this study. To compliment the eddy diffusivity estimates, probability and travel time maps show drifter sampling patterns as well as the mean time of arrival to the sampled regions. Collectively these methods provide a comprehensive picture the efficiency of turbulence at spreading material within the Gulf of Mexico across two seasons, as well as offer bulk metrics for assessing the fidelity of, and informing, models used to describe the spread of tracers.

4.2 GLAD and LASER Drifters

As a part of the Grand LAgrangian Deployment (Poje et al., 2014) about 300 GPS-tracked CODE type surface drifters were released in the Northern GoM from 20 July to 31 July 2012, and as a part of the LAgrangian Submesoscale ExpeRiment (LASER), roughly one thousand GPS-tracked CARTHE-type surface drifters (Novelli et al., 2017) were released in the Northern GoM from 18 January to 13 February 2016. These drifters reported position data nominally every 5 minutes for several months and were drogued to follow the integrated flow of the top ∼1m of the water column (Poje et al., 2014; Novelli et al., 2017). The drifter trajectories were processed by removing outliers, low-pass filtering (Yaremchuk and Coelho, 2015) and interpolating positions to uniform 15-minute intervals. Some of the LASER drifters lost their drogues, and the timesteps where drifters were without drogues were discarded based on the drogue-loss detection method of Haza et al. (2018). While previous work has utilized specific launches (Pearson et al., 2019; Chang et al., 2019; Pearson et al., 2020), this study uses drogued drifters for all available times.

4.3 Methods

4.3.1 Probability and Travel Time Maps

Ocean dynamics in the Gulf of Mexico are highly-variable, and consequently the exact nature of near-surface dispersion is reliant on the time and location of release. However, there is utility in defining drifter distributions in a probabilistic sense (Rypina et al., 2011, 2014, 2017). The probability map characterizes the number of trajectories that passed through a given bin (only counted at the first arrival) and the travel time map indicates the mean time at which the trajectories that passed through a bin first arrived there. This provides context for drifter sampling patterns and interpretations for both the Lagrangian integral times and diffusivities presented in the next sections. To calculate the probability, the domain is broken up into boxes with lengths $dlon \approx dlat \approx 0.05km$, and the percentage of drifters that visit the i^{th} box is given by

$$P_i = \frac{N_i}{N} \tag{4.1}$$

Where N_i is the number of trajectories that made it to the i^{th} bin at least once in the roughly

three month period for each season and N is the total number of trajectories that could have made it to the i^{th} bin over that timeframe. For GLAD, $N = 297$ and for LASER $N = 956$.

The travel time map is constructed such that the average time of arrival of the successful trajectories entering the i^{th} bin is given by

$$\overline{T}_i = \frac{\Sigma T_i}{N_i} \tag{4.2}$$

where the overbar indicates the arithmetic average, and the sum is over all 'first-hit' times T_i for the successful trajectories N_i.

4.3.2 Lagrangian Structure Functions and Autocorrelation Functions

Lagrangian velocity structure functions are the averaged powers of the Cartesian velocity difference between time $t + \tau$ and the time t along a trajectory (Babiano et al., 1987). Mathematically this is given by

$$S_{L\gamma}^{n}(\mathbf{a}, t, \tau) = \langle (u_\gamma(\mathbf{a}, t + \tau) - u_\gamma(\mathbf{a}, t))^n \rangle \tag{4.3}$$

where the subscript L emphasizes a Lagrangian structure function (as opposed to Eulerian structure functions often used in other studies), subscript γ is the Cartesian velocity increment along a particle trajectory (either zonal or meridional), $\mathbf{a}$ is the initial particle position, t is time, τ is the time lag, n is the order of the structure function, and $\langle \cdot \rangle$ is an average over all values at a given lag and often over all particle trajectories as well. The nth-order Lagrangian structure function corresponds to the nth-moment of the probability density function (PDF) of Lagrangian velocity differences. Statistical stationarity and homogeneity imply that the PDFs, and therefore the moments of the PDFs, are unchanged under translations in space and time. This removes the dependence on the initial position $\mathbf{a}$ and ensures that the structure function is only dependent on the time lag τ, and not the absolute time t. Under these assumptions, Equation 4.3 is reduced to $S_{L\gamma}^{n}(\tau) = \langle (\Delta u_\gamma)^n \rangle$ where Δu_γ is difference in velocity at time lag τ.

In stationary and homogeneous flows, the Lagrangian second-order structure is related to the temporal autocorrelation function, $R_{L\gamma}(\tau) = \frac{1}{\sigma_\gamma^2} \langle u_\gamma(\mathbf{a}, t) u_\gamma(\mathbf{a}, t + \tau) \rangle$, by

$$R_{L\gamma}(\tau) = 1 - \frac{S_{L\gamma}^{2}(\tau)}{2\sigma_\gamma^2} \tag{4.4}$$

where σ_γ^2 is the velocity variance of the γ component of velocity. Throughout this work, $R_{L\gamma}(\tau)$ is estimated using $S_{L\gamma}^{2}(\tau)$. There are several benefits to this method, although there are also certainly some pitfalls (e.g. non-stationarity). Notable of the benefits are that the structure function approach does not require an estimate of the sample mean, and also removes any linear trends present in the time series (equivalent to first-differencing methods). Use of the structure function as traditionally prescribed does not however account for the effects of mean gradients, which will be discussed in the following section. To eliminate the effects of non-stationarity and heterogeneity that preclude the

use of Equation 4.4, segmentation of the individual drifter trajectories under a variety of segment lengths are considered such that the structure function (and therefore the autocorrelation function) are well estimated but that the flow regimes sampled throughout a segment length do not vary much in time or space. The details of this are laid out in section 4.3.5.

4.3.3 Corrected Lagrangian Structure Functions and Autocorrelation Functions

In traditional turbulence studies, homogeneity implies that there is at most a constant background velocity and therefore no mean velocity gradients. Under these assumptions, the first-order Eulerian structure function is zero. However, in realistic flows this is often not well realized, and Pearson et al. (2020) defined a mathematical relationship to correct higher-order Eulerian structure functions using the non-zero first-order Eulerian structure function. This method is adapted here to correct for the presence of a temporally and spatially varying mean in a Lagrangian setting. Under the assumption of a Reynold's decomposition, the flow is separated into it's time mean and time-varying turbulent components as $\mathbf{u} = \langle \mathbf{u} \rangle + \mathbf{u}'$ respectively, with $\langle \mathbf{u}' \rangle = 0$. There are different choices to calculate the mean, and the consequences of this are touched on in Section 4.3.4. For the purposes of this section, a generic linear averaging operator is implied. Substituting this into Equation 4.3 yields

$$
\begin{aligned}
S_{L_\gamma}^2(\tau) &= \langle (\Delta \langle u_\gamma \rangle + \Delta u'_\gamma)^2 \rangle && (4.5)\\
&= \langle \Delta \langle u_\gamma \rangle^2 + 2\Delta \langle u_\gamma \rangle \Delta u'_\gamma + (\Delta u'_\gamma)^2 \rangle && (4.6)\\
&= \langle \Delta \langle u_\gamma \rangle^2 \rangle + \langle (\Delta u'_\gamma)^2 \rangle && (4.7)\\
&= [S_{L_\gamma}^1(\tau)]^2 + S_{L_\gamma}^{2\prime}(\tau) && (4.8)
\end{aligned}
$$

where $S_{L_\gamma}^{2\prime}(\tau)$ is the *corrected* second-order Lagrangian structure function. Solving the above for the perturbation yields

$$
S_{L_\gamma}^{2\prime}(\tau) = \langle (\Delta u'_\gamma)^2 \rangle = S_{L_\gamma}^2(\tau) - [S_{L_\gamma}^1(\tau)]^2 \tag{4.9}
$$

Thus, the perturbation statistics can be recovered by subtracting off the square of the first order structure function from the second order structure function calculated with the total velocity. The corrected structure functions can similarly be used to correct the autocorrelation functions

$$
R'_{L_\gamma}(\tau) = 1 - \frac{S_{L_\gamma}^{2\prime}(\tau)}{2\sigma_\gamma^2} \tag{4.10}
$$

The correction removes the effects of mean gradients in the flow due to either persistent horizontal spatial gradients, or changes in the flow field over time, which are not accounted for with other methods (e.g. Mariano et al., 2016). In addition to removing these effects in a scale-dependent manner, this method does not require the inclusion of additional data sources, which is likely to reduce uncertainty.

4.3.4 Horizontal Eddy Diffusivity and the Lagrangian Integral Time

Passive tracers are particularly instrumental for transport studies because they in principle do not provide any feedbacks on the flow itself, and many materials such as oil, nutrients, and plankton are often approximated as passive tracers. However, due to spatial and temporal discretization in numerical models, parametrizations are needed to account for the scales of turbulent motion that are not fully resolved in the modelled velocity field responsible for tracer transport and distributions. Diffusive models are often implemented, and are analogous to molecular diffusivity except with an enhanced diffusivity coefficient (e.g. Fox-Kemper et al., 2011; Bachman et al., 2015). Then, if there is meaningful separation between the scales of turbulence and the mean flow (Taylor, 1921), the evolution of a conservative passive tracer field can be represented in an Eulerian framework by an advection-diffusion equation,

$$\frac{\partial C}{dt} + \mathbf{U} \cdot \nabla C = -\nabla \cdot \langle \mathbf{u}' c' \rangle \equiv \nabla \cdot (\mathbf{K} \nabla C) \tag{4.11}$$

where $\mathbf{U} = (U, V, W)$ is the mean velocity vector, C is the mean concentration, c' is the concentration fluctuation, $\mathbf{u}' = (u', v', w')$ is the turbulent velocity vector (i.e. unresolved eddies), and $\mathbf{K}$ is the eddy diffusivity tensor, which includes an advective (antisymmetric) and diffusive (symmetric) part that constitute the reversible and irreversible affects of turbulence respectively. While future work will investigate all horizontal elements of the full eddy transport tensor (e.g. Rypina et al., 2016), this study focuses on the diffusive component.

Equation 4.11 is also a macroscopic representation of particles experiencing persistent random walks (Taylor, 1921). In this Lagrangian framework, the eddy diffusivity (K_γ) is defined as the rate of turbulent absolute (i.e. single-particle) dispersion

$$K_\gamma = \frac{1}{2}\frac{d}{dt}\langle (X'_\gamma)^2 \rangle = \frac{d}{dt}\Big[\sigma_\gamma^2 \int_0^t (t-\tau) R_{L\gamma}(\tau) d\tau\Big]. \tag{4.12}$$

where X' is the residual particle displacement. It is important to note that there are several approaches to separating the mean and residual components of displacement and velocity. Two common methods are often implemented. For example, with the velocity field used in the autocorrelation function, either the time averaged velocity along the particle trajectory, or a local average Eulerian velocity from nearby drifters or from other stationary observing systems is subtracted from the total velocity (Davis, 1991b; Zhang et al., 2001). The resulting statistics are typically dependent on this choice (e.g. LaCasce, 2008). However it is reiterated that when using the structure function, no sample mean is estimated and the the correction method proposed in Section 4.3.3 removes residual first-order structure functions present due to non-uniform mean fields. Thus, while the second order structure function does not depend on the choice of a sample mean, the interpretations of the correction itself will.

The Lagrangian integral time, $T_{L\gamma} = \int_0^\infty R_{L\gamma}(\tau) d\tau$, is a basic metric of predictability that describes the memory of a particle along its trajectory, for example how long a particle remembers it's initial conditions. It sets the boundary between different regimes of particle motion, which

is reflected by different shapes of the absolute dispersion curve. Thus, the Lagrangian integral time of can be used to investigate the asymptotic limits of the absolute dispersion, and therefore also the limits of the absolute eddy diffusivity. In the limit of comparatively short times (i.e. $t \ll T_{L\gamma}$), $R_{L\gamma}(\tau) \sim 1$, and $\langle (X'_\gamma)^2 \rangle \approx 2\sigma_\gamma^2 \int_0^t (t-\tau) d\tau = \sigma_\gamma^2 t^2$. This is the initial growth phase, where particles disperse ballistically due to the local velocity field. In the limit of long times (i.e $t \gg T_{L\gamma}$), the integral of $R_{L\gamma}(\tau)$ approaches $T_{L\gamma}$, and provided the integrals converge, $\langle (X'_\gamma)^2 \rangle = 2\sigma_\gamma^2 t \int_0^t R_{L\gamma}(\tau) d\tau - 2\sigma_\gamma^2 \int_0^t \tau R_{L\gamma}(\tau) d\tau \approx 2\sigma_\gamma^2 t T_{L\gamma}$. This is the random walk phase, where dispersion grows linearly in time. The presence of this phase implies that the eddy diffusivity is constant, and the motion is captured by a diffusion equation. Under the same limits, the absolute diffusivity is

$$K_\gamma \approx \begin{cases} \frac{1}{2}\frac{d}{dt}\left[\sigma_\gamma^2 t^2\right] = \sigma_\gamma^2 t & t \ll T_{L\gamma} \\ \\ \frac{1}{2}\frac{d}{dt}\left[2\sigma_\gamma^2 t T_{L\gamma}\right] = \sigma_\gamma^2 T_{L\gamma} & t \gg T_{L\gamma} \end{cases} \tag{4.13}$$

Thus, if the Lagrangian integral time is known as well as the velocity variance, an estimate of the absolute eddy diffusivity can be made. Note also that this is independent of the concentration, and is thus generic for a given passive tracer. A good review of these properties is given in LaCasce (2008).

4.3.5 Computational Details

To limit the effects of drifters sampling different turbulent regimes throughout their lifetimes, each drifter trajectory was broken up into non-overlapping segments of different lengths. Initial testing revealed that 15 days for both GLAD and LASER were a good trade off between the necessity for long trajectories to obtain robust structure functions and short segments to limit the impacts of heterogeneity and non-stationarity. Approximately 6% of values in each time lag bin were greater or less than twice the standard deviation of all values within the bin for both GLAD and LASER. This percentage was similar for 12 day long segments and did not change significantly (by about 0.5%) for 25 day segments, suggesting this was a reasonable choice. Future work will more fully investigate the influence of trajectory length on these methods. The Lagrangian integral timescales and eddy diffusivities were found as follows:

1. For each trajectory segment, and each drifter, the Lagrangian structure function values were calculated for all possible time differences along each trajectory for the segment
2. These values were placed into linear bins of width 0.05 days which were arithmetically averaged to obtain one value for each bin, for a given drifter, for a given segment.
3. The Lagrangian structure function for each segment and each drifter was then converted to the autocorrelation function and integrated as a function of time.
4. The Lagrangian integral time was taken as the last time that the integral of the autocorrelation function was positive.

5. The eddy diffusvity was found by multiplying by the Lagrangian integral time by the variance for each drifter, for each segment.

This process was repeated for the corrected Lagrangian structure function, which was found in the same manner except that the squared first-order Lagrangian structure function was subtracted from each binned second-order Lagrangian structure function before conversion to the autocorrolation function.

4.4 Results

4.4.1 Probability and Travel Time Maps

To illustrate how the drifters are transported throughout the GoM in a statistical sense, the probability and travel time maps are shown in Figure 4.1 for both GLAD and LASER. The probability maps (left column) show the likelihood of visiting a given location (here a roughly 0.05km by 0.05km lat-lon box) at least once. The travel time maps (right column) show the average time taken to get to a given spot by all the trajectories that visited that location. Comparing the top row to the bottom row, it is evident that drifters from GLAD travelled to very different locations at very different speeds than the LASER drifters. The yellow and orange areas of the left column of panels signify the highest probabilities of reaching a given location. In summer this is primarily to the southeast of the Mississippi River outflow, and patterns of counter-clockwise rotation are outlined with high probability. This is not the case for the LASER drifters, which show a strong preference for a direct path to the middle of the GoM, denoted by the yellow line from north to south. At around 23°N this region of high probability separates into two branches, likely constrained by the local bathymetry or the Loop current.

The travel time maps paired with the probability maps and other data sources illustrate the effect of different types of forcing on the fate of each set of drifters in the GoM. During LASER, the region of high probability is sampled 10-20 days after launch, denoted by purple coloring on the travel time map. Discharge, temperature, and salinity measurements from the Baton Rouge, LA station indicate that there was an anomalously large discharge of cold, fresh water that began shortly after the drifters were released and persisted for roughly 25 days, flushing the drifters away from the shelf and towards the interior of the GoM. Local radar measurements also suggest strong frontal activity during this time (D'Asaro et al., 2018; Pearson et al., 2020), and the narrow region of high probability could be related to the along front flow at the interface of the Mississippi River outflow and the interior loop current waters. During GLAD the drifters stay nearer the mouth of the Mississippi river until about 30-40 days after release. On August 27th, 2012, Hurricane Isaac entered the GoM from the southeast, and likely lead to the spread in trajectories present after 30-40 days which is supplemented by low probability.

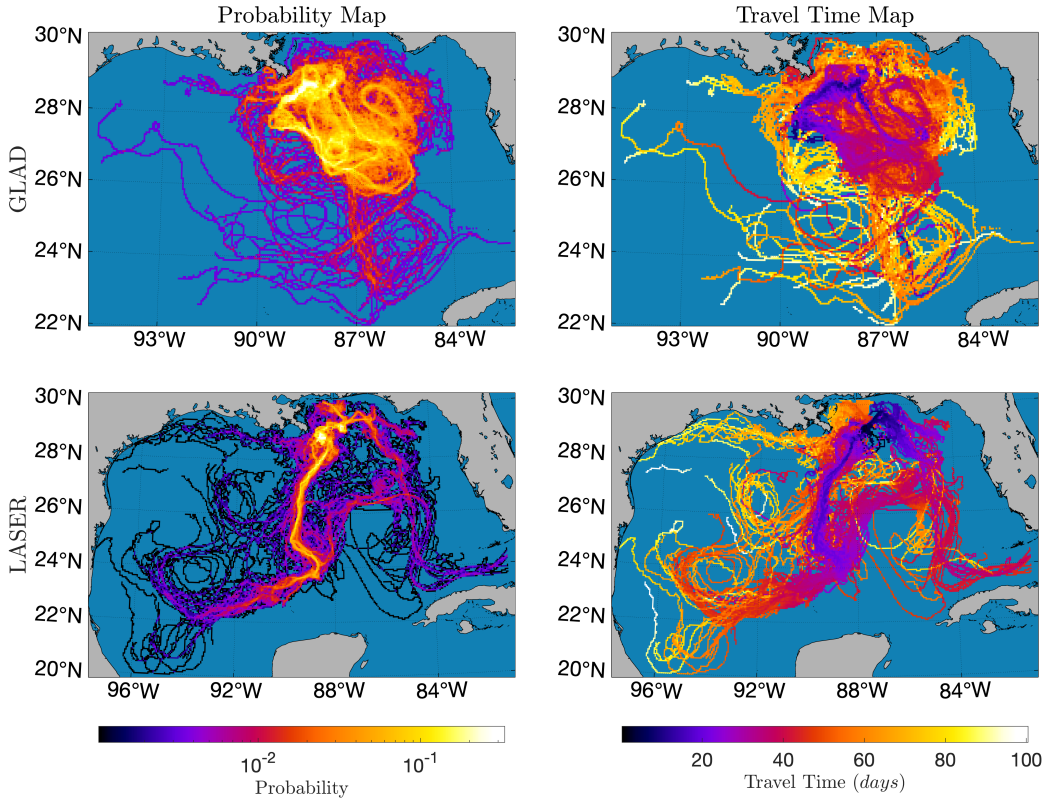

Figure 4.1: The GLAD **(top)** and LASER **(bottom)** probability **(left)** and mean travel time **(right)** maps. The colorscale for probability is logarithmic and the colorscale for mean travel time is linear. Colorbars are constrained such that the minimum value on the colorbar is the largest minimum value between GLAD and LASER and the minimum value on the colorbar is the smallest maximum value between GLAD and LASER. Note that because GLAD had fewer drifters total, the probability for just one drifter is higher than that for LASER.

4.4.2 Lagrangian Autocorrelation Functions

The average Lagrangian autocorrelation functions (LACs) for each time segment are plotted for GLAD and LASER in Figure 4.2. Lighter colors indicate earlier times, and darker colors indicate later times. The average is over all individual drifter structure functions for each segment. The zonal LACs are plotted in the first two columns, and the meridional LACs are plotted in the second two columns. Uncorrected estimates are shown in the first and third column, and corrected estimates are shown in the second and fourth column. GLAD is plotted in the first row, and LASER the second.

All LACs for both GLAD and LASER oscillate, rather than smoothly descending to zero. This is due to advective 'meanders' in the flow field, for example from the mean flow or near-inertial waves. Visually, the prominent cycle in all LACs is diurnal. In the Gulf of Mexico, at least three processes occur on nearly diurnal timescales: inertial oscillations, tides, and the sea breeze (e.g. Gough et al., 2016). Inertial oscillations are the response of the ocean to winds on a rotating Earth (Ekman,

1905), and are expected to vary in magnitude with the mixed layer depth (Pollard and Millard Jr, 1970), as well as the strength of variable wind forcing at frequencies near the inertial frequency. This may explain the more pronounced diurnal cycle in GLAD compared to LASER, and is consistent with other studies in this region where thin mixed layers and more consistent diurnal wind forcing in summer lead to more energy in the inertial band, and deeper mixed layers and intermittent wind forcing due to frontal passages lead to less energy in the inertial band in winter (DiMarco et al., 2000; Jarosz et al., 2007; Anderson and Sharma, 2008; Teague et al., 2014; Gough et al., 2016).

Large river discharge during LASER as well as the presence of Hurricane Isaac during GLAD is also likely to have influenced the shape and magnitude of the LACs. For GLAD, a dramatic reduction in the amplitude of the oscillations is seen for later segments (darker colors), suggestive of an increase in variance possibly due to changes in winds. For LASER, since the mixed layer depth is tied to inertial oscillations, the freshwater induced shoaling of the mixed layer could have produced enhanced inertial motion relative to other winters.

Testing with longer trajectory segments revealed that other, longer periods are also present, and thus the LACs are not expected to asymptote to zero over the 15 day window shown here. Regardless of the generating mechanism of these oscillations, it emphasizes the importance of refining conventional methods for calculating the Lagrangian integral timescale. Many approaches are based on the time to reach the first and second zero-crossing of the autocorrelation function. When autocorrelation functions are oscillatory, as is the case here, that approach would lead to erroneously low integral times due to the initial lobes that are negative for many segments with large amplitudes. Note that using the relative diffusivity (i.e. from particle pairs instead of single-particles), which asymptotes to the absolute eddy diffusivity after particles decorrolate) would likely reduce these

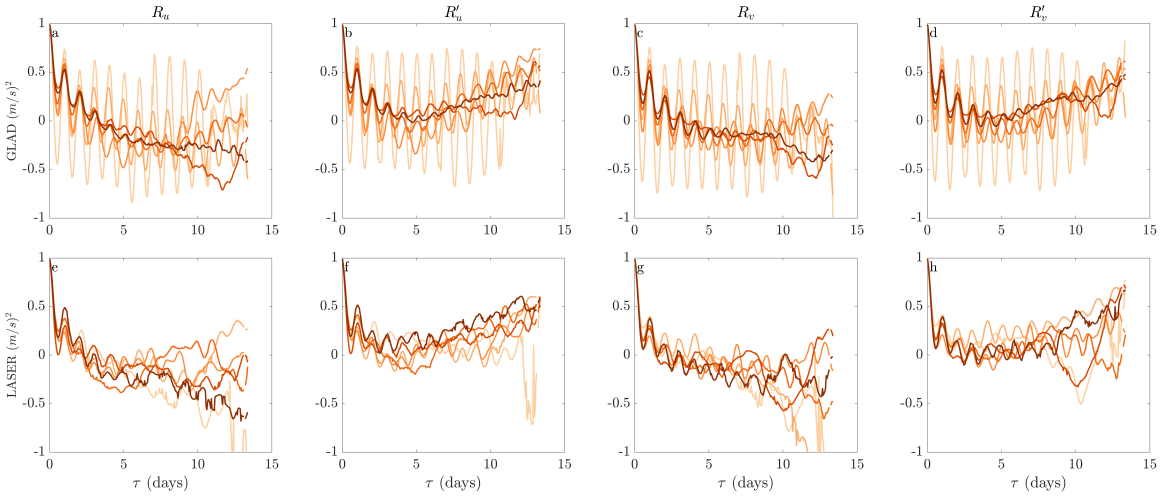

Figure 4.2: Uncorrected **(a,c,e,f)** and corrected **(b,d,g,h)** Lagrangian autocorrelation functions in the zonal **(a,b,e,f)** and meridional **(c,d,g,h)** directions of GLAD **(upper)** and LASER **(lower)** drifters. Analysis is for 15 day long non-overlapping trajectory segments, and bins that have less then 10% of the maximum number of values in any bin for individual drifter estimates are removed.

contributions, as long as both particles experience sufficiently similar meanders. Our method of taking the last time that the integral is positive, while having its own limitations (for example if the longest periods are intermediately captured in the last cycle), alleviates some of this by taking into account the wavy motion that should in principle integrate to zero with sufficient time.

The corrections for the Lagrangian structure functions (LSFs, not shown) are largest at the longest time lags, and therefore so are the corrections to the LACs. Note that the variance comes into play when converting from the LSFs to the LACs (per Equation 4.4), which scales the curves in the conversion. At larger time lags, the locations along the trajectory are also likely to be well separated in space, and the effects of mean gradients more prominent. The general behavior of the correction is to re-correlate at longer time lags. Note that the correction is positive definite, and thus includes the effects of gradients that are both shearing and compressing. Thus, it is likely that there are contributions from, for example, drifters being drawn into convergent submesoscale features as well as shearing from gradients perpendicular to drifter motion. Visually, the correction seems to become important for most LACs after 5 days, which is where the effects of submesoscale eddies are likely to begin (e.g. Mariano et al., 2016). Alongside recorrelation, the correction also has the effect of collapsing the more dispersed curves seen in the uncorrected estimates at longer time lags.

4.4.3 Lagrangian Integral Time

Spatial maps of the Lagrangian integral time (LIT= $T_{L\gamma}$) are plotted for GLAD and LASER in Figure 4.3. The zonal LIT is plotted in the first two columns, and the meridional LIT is plotted

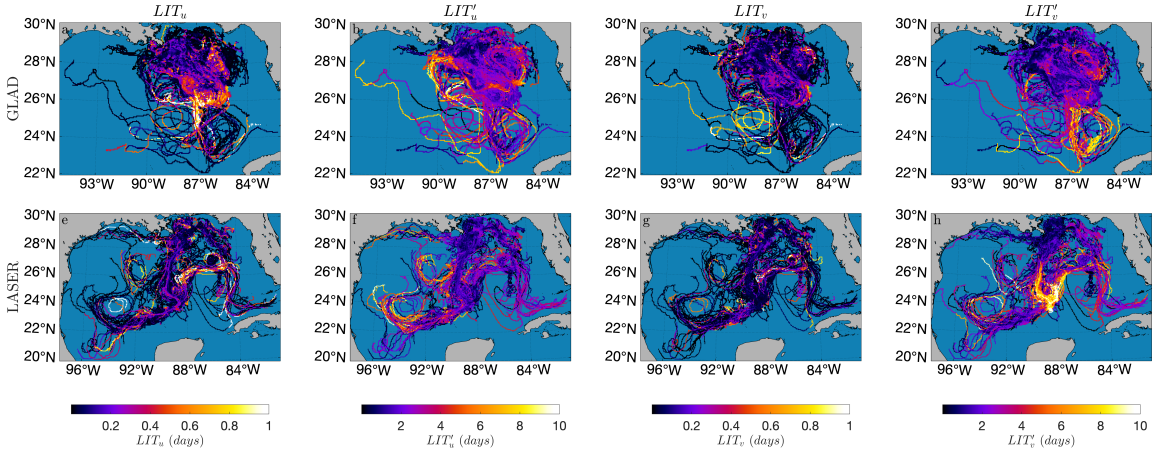

Figure 4.3: Uncorrected **(a,c,e,f)** and corrected **(b,d,g,h)** Lagrangian integral time in the zonal **(a,b,e,f)** and meridional **(c,d,g,h)** directions of GLAD **(upper)** and LASER **(lower)** drifters. Analysis is for 15 (12) day long non-overlapping trajectory segments GLAD (LASER). The colorbars are capped to 2 days for the uncorrected estimates and 10 days for the corrected estimates. The maximum values for GLAD rounded to the nearest 0.1 day are $LIT_u = 1.5$; $LIT'_u = 10.5$; $LIT_v = 2$; $LIT'_v = 8.9$. The maximum values for LASER are $LIT_u = 1.8$; $LIT'_u = 9.4$; $LIT_v = 1.6$; $LIT'_v = 11.7$.

in the second two columns. Uncorrected estimates are shown in the first and third column, and corrected estimates are shown in the second and fourth column. GLAD is plotted in the top row, and LASER the bottom row. It is expected from the literature that LITs are on the order of a day in coastal regions, 2-4 days or more in the open ocean, and 5 days or more in energetic regions with strong currents and eddy activity (see Mariano et al. (2016) for a literature review). The results of the uncorrected LITs are within the range of, but on the lower end, of previous estimates in the Northern Gulf of Mexico of a few days (Ohlmann and Niiler, 2005; Mariano et al., 2016). However, corrected estimates of zonal and meridional LITs are drastically larger for both GLAD and LASER, by as much as 10 times. This is in keeping with the presence of energetic mesoscale eddies and quick southerly jets noted in Figure 4.1. The amplified LITs are a consequence of recorrelation at longer time lags from the correction and from the method of integration of the autocorrelation function. It should be noted however that some of the largest values are in places where low numbers of drifters visited, for example the stray yellow and white colored trajectory on the western side of the Gulf during GLAD.

The uncorrected LITs also have a smaller range than the corrected LITs, denoted by a smaller difference between minimums and maximums on respective colorbars. Further, while all maps of LITs have structure that resonates with the sampling patterns shown in Figure 4.1 (e.g. flow bifurcations, eddies, topographic influences), it is more pronounced in the corrected estimates. For GLAD, distinct eddying motions can be discerned, with integral times of 3-8 days. Nearshore, LITs are smaller, particularly in the meridional direction, on the order of 2 days or less. For LASER, a notable jet shows correlation times of 3-9 days in the meridional direction and, consistent with Figure 4.1 which shows it took the drifters on average about 10 days to go from their initial locations to the flow bifurcation to the south. After the bifurcation, the flow splits likely due to interactions with the loop current and bathymetry, and zonal correlations are on the order of 3 days. Note the strong correlation of the jet this flow bifurcation is essentially absent in the uncorrected LITs. Mesoscale eddies are present in the western Gulf of Mexico, as well as near the loop current, with LITs ranging from 4-9 days.

4.4.4 Absolute Eddy Diffusivity

Spatial maps of the absolute eddy diffusivity (ED) are plotted for GLAD and LASER in Figure 4.4. The zonal ED is plotted in the first two columns, and the meridional ED is plotted in the second two columns. Uncorrected estimates are shown in the first and third column, and corrected estimates are shown in the second and fourth column. GLAD is plotted in to top row, and LASER the bottom row. All EDs for both GLAD and LASER show anisotropy and heterogeneity, which stresses the importance of including spatially varying and directionally dependent diffusivities in models. The uncorrected values are the order of $0.1 - 0.8 \times 10^4 m^2/s$ for GLAD, and less than $0.2 \times 10^4 m^2/s$ for LASER. This is in the range but typically less than previous estimates in this region using GLAD drifters (e.g. Mariano et al., 2016). Aside from smaller LITs, this could also be due to a change in velocity variance using shorter segments, which would reduce the diffusivity. Additionally LASER

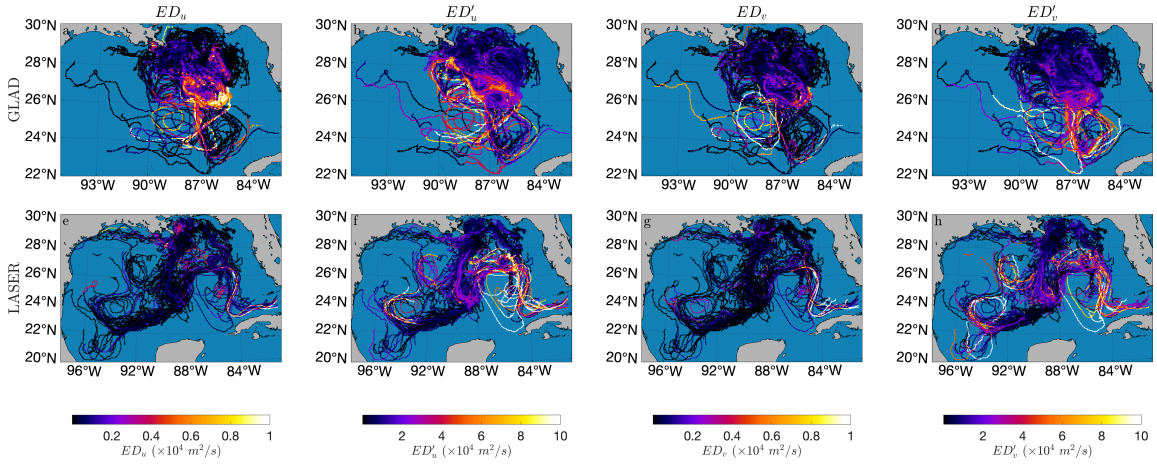

Figure 4.4: Uncorrected **(a,c,e,f)** and corrected **(b,d,g,h)** absolute eddy diffusivity in the zonal **(a,b,e,f)** and meridional **(c,d,g,h)** directions of GLAD **(upper)** and LASER **(lower)** drifters. Analysis is for 15 day long non-overlapping trajectory segments. The colorbars are capped to $1 \times 10^4 m^2/s$ for the uncorrected estimates and $0 times 10^4 m^2/s$ for the corrected estimates. The maximum values rounded to the nearest 0.1 $\times 10^4 m^2/s$ for GLAD are $ED_u = 2.9$; $ED'_u = 17.8$; $ED_v = 2.3$; $ED'_v = 15.0$. The maximum values rounded to the nearest 0.1 $\times 10^4 m^2/s$ for LASER are $ED_u = 1.7$; $ED'_u = 23.3$; $ED_v = 4.3$; $ED'_v = 19.2$.

shows a much smaller magnitude of spatial variability than GLAD.

As with the corrected LITs, the corrected ED estimates are much larger than uncorrected estimates, especially along the southerly jets where values are on the order of $3-4 \times 10^4 m^2/s$, and also nearer the loop current where values are on the order of $7-8 \times 10^4 m^2/s$. Additionally the differences between the maximum and minimum values of GLAD and LASER are less than the uncorrected estimates. For GLAD in particular, both uncorrected and corrected estimates have lower values near the coast than regions farther from the coast. This is also true of LASER in the corrected estimates. For the uncorrected estimates during GLAD, the ED is typically less than $0.2 \times 10^4 m^2/s$ near the shore and $1 \times 10^4 m^2/s$ farther from the coast. For the corrected estimates, this is less than $2 \times 10^4 m^2/s$ near the shore and $4 - 10 \times 10^4 m^2/s$ farther offshore. Note the gradient in EDs between nearshore and interior is larger than the same gradient for the LITs, and this is due to the spatial variability of the velocity variance (not shown). The difference between corrected and uncorrected estimates, however, resides in the product of the velocity variance (constant between the two estimation methods), paired with the larger values of corrected LITs. Further, the maps of EDs retain much of the structure of the maps of LITs in Figure 4.3. This is once again more prominent in the corrected maps, where eddy activity, the loop current, and the southerly jets all show distinct diffusivity values.

4.5 Discussion and Conclusions

Understanding and modelling the transport and dispersion of tracers by mesoscale eddies is a long-standing problem in oceanography. In addition, the complexity of obtaining mathematically and numerically feasible approximations of eddy induced mixing is complicated by the ability to obtain consistent estimates from observations using various techniques (e.g. Klocker et al., 2012). This study refines existing methodology to account for residual mean gradients. By correcting the auto-correlation function using the first-order Lagrangian structure function, it is found that estimates of both the Lagrangian integral time and absolute eddy diffusivities are larger and have different spatial structure than the uncorrected estimates. The corrected estimates better capture the features well sampled by the drifters, and correlation timescales map well to the length of time drifters spend in given features. The GLAD and LASER experiments were ground-breaking in the number of drifters used, and this method is much better suited to large numbers of drifters. With few drifters, the estimates of the first order structure function are not sufficiently well-determined to be removed. Here, the corrected estimates are only robust where there are many location pairs available to estimate the structure functions. In addition, while more work is needed to isolate the length of trajectories most suitable for this analysis, the results suggest this method is a promising tool for informing models as well as potentially reconciling differing estimates of absolute diffusivities with Lagrangian observations.

4.6 Acknowledgments

The authors wish to thank the large team of scientists and support staff during the LASER campaign. This research was made possible in part by a grant from The Gulf of Mexico Research Initiative to the Consortium for Advanced Research on the Transport of Hydrocarbons in the Environment (CARTHE) and in part by grant N00014-17-1-2963 from the Office of Naval Research. Data are publicly available through the Gulf of Mexico Research Initiative Information & Data Cooperative (GRIIDC) at https://data.gulfresearchinitiative.org under DOIs 10.7266/N7VD6WC8 (GLAD) and 10.7266/N7W0940J (LASER).

Chapter 5

Conclusions

Submesoscale features and processes with length scales of 1-10km strongly affect the state of the upper ocean by providing routes for large-scale energy to be dissipated, and by altering the distribution and transport of physical quantities (e.g. heat, freshwater, sea ice), biogeochemical tracers (e.g. nutrients and marine life) ans anthropogenic material (e.g. floating debris and pollutants). Surface drifters are a powerful observational platform that while simultaneously sampling larger scales, id capable of tracking submesoscale features – characteristics hard to come by via other instrumentation. This thesis utilizes drifter observations and numerical simulations to characterize turbulent dispersion in the Gulf of Mexico, with heavy emphasis on how features over the submesoscale range of motion, as well as heterogenous and non-stationary flows, affect their single- and two-point statistics. In this chapter, I will review and summarize the major findings of this thesis, outline the implications of these results, and discuss future work.

5.1 Summary

The Eulerian velocity structure function is commonly used as a way to describe the cascade of energy or enstrophy in a turbulent velocity field. With the release of unprecedented drifters in the Gulf of Mexico, the ability of (semi) Lagrangian surface drifters to provide representative estimates of Eulerian structure functions is tested in Chapter 2 as well as Chapter 3. In Chapter 2, numerical simulations of the Northern Gulf of Mexico are paired with Lagrangian particle tracking to understand the impact of convergence zones and vortices on turbulence statistics derived from synthetic surface drifters. When compared to Eulerian structure functions, drifter derived structure functions were susceptible to changes in both slope and magnitude, metrics that are typically used to diagnose the class of turbulence present. When taken collectively, the second-order statistics of cluster releases of synthetic drifters that emulate observations are statistically distinct from Eulerian second-order statistics. Specifically, second-order drifter structure functions were consistently shallower, scaling as $r^{2/3}$, while Eulerian structure functions scaled as r. Finally, third-order drifter structure functions had larger magnitudes than Eulerian third-order statistics, overestimating the energy flux across

scales.

These differences are explained by correlated divergence and curl structure functions over the submesoscale range of motion, where unlike the mesoscales, the surface divergence due to ageostrophic flows is non-negligible. These correlations lead to shallower second-order structure functions and larger third-order structure functions when compared to Eulerian statistics, which has implications for interpreting these structure functions as the cascades of energy or enstrophy. Alongside the curl and divergence structure functions, a Helmholtz decomposition reformulated in structure-function space was applied. The results show that drifters are ill-suited for this method due to large differences between the longitudinal and transverse structure functions. which based on the results of Chapter 3, are in line with oversampling of vorticity and divergence. The degree of difference between drifter and Eulerian statistics depends on the launch location and pattern, making it difficult to correct for this bias. Additionally, analysis of a large synthetic drifter release reveals the bias appears to diminish with scale. This suggests that drifters may be appropriate for approximating mesoscale statistics, provided sampling is sufficient, but over the submesoscale range drifter-derived statistics are not agnostic to the flow properties which determine their sampling patterns.

In Chapter 3, observed velocity structure functions from Eulerian X-band radar measurements and semi-Lagrangian surface drifter measurements are also compared, and disagree in a way consistent with the results from the numerical simulations presented in Chapter 2. Second-order drifter structure functions are typically shallower than Eulerian second-order structure functions, and drifter third-order structure function magnitudes are typically larger than Eulerian third-order structure function magnitudes. Alongside validating the prevalence of the drifter biases in observations, this study builds upon the work of Pearson et al. (2019) by refining the impacts of convergence and vorticity on the second- and third order structure functions.

The biases investigated with the observations in Chapter 3 are two-fold. In addition to the accumulation bias from oversampling frontal regions and vortices in keeping with the results of Chapter 2, the differences between Eulerian and surface drifter velocity structure function are also shown to be due to a background bias from non-zero first-order structure functions. The accumulation bias is highlighted by analyzing the joint probability distribution of divergence (vorticity) and scale, alongside the structure function dependent on divergence (vorticity) and scale from X-band radar measurements. The steepest gradient as a function of r is associated with near-zero values of divergence and vorticity, which are also the most commonly sampled measurements with our data. At stronger convergence, the second-order structure functions have shallower slopes, consistent with the findings of Chapter 2. The same analysis of the joint probability distribution functions and third-order structure functions shows that they are expected to be larger at smaller scales with stronger convergence. These findings provide additional context for interpretations of the accumulation bias first presented in Chapter 2.

In Chapter 3 the notion of a background bias is introduced, which is the residual first-order structure function present in higher order statistics due to a heterogeneous and anisotropic flow field. Unlike the accumulation bias, the background bias is correctable. In classical turbulence, the

first-order structure function should be zero. However for heterogeneous and anisotropic flows, the first-order structure is often non-zero due to mean gradients that persist in the flow field. Assuming a Reynold's decomposition, these effects can be accounted for in both the second- and third-order statistics. Analysis suggests that when averaging and coverage is sufficient, the effects can be small. However, for isolated regions, or when not averaged over a long enough period, the effects can be large. This is true of both the drifter and Eulerian statistics, suggesting the importance of averaging windows and domain coverage when interpreting statistics of this nature.

In Chapter 4, transport and dispersion are investigated through probability and travel time maps as well as the spatial distribution of the absolute eddy diffusivity. The absolute eddy diffusivity is found by first converting the Lagrangian second-order structure function to the Lagrangian autocorrelation function. The autocorrelation function is then integrated until the last time that the integral was positive to obtain the Lagrangian integral time, which when multiplied by the velocity variance yields the absolute eddy diffusivity Taylor (1921). On its own, this procedure is advantageous compared to other methods, as when using the structure function the sample mean as well as any linear trends are automatically removed, equivalent to first differencing. Second, unlike traditional methods where the first zero-crossing is used as the integration upper limit, choosing the last time the integral itself was positive accounts for wavy autocorrelation functions from drifters that are subject to inertial oscillations, tides, and submesoscale processes.

A corrected estimate, using the same procedure outlined previously, but with the effects of non-zero first-order Lagrangian structure functions are also made. This procedure is analogous to that outlined in Pearson et al. (2020) and Chapter 3, but the velocity increments are in time following a trajectory, rather than from pairs of drifters in space. This, in principle, removes the effects of mean shear in space or time from heterogeneous and non-stationary flows that corrupt the second-order statistic calculated with the total velocity. It is found that estimates of both the Lagrangian integral time and absolute eddy diffusivities are larger and have different spatial structure than the uncorrected estimates. The corrected estimates better capture the features well sampled by the drifters, and correlation timescales map well to the length of time drifters spend in given features. While more work is needed to isolate the length of trajectories most suitable for this analysis, the results suggest this method is a promising tool for informing models as well as potentially reconciling differing estimates of absolute diffusivities with Lagrangian observations.

5.2 Implications and Future Work

The evolution of tracers (such as oil) in the ocean depends on the interaction of a wide spectrum of time and space scales, making it inherently difficult to predict and elucidate. This is particularly true over the submesoscale range of motion, where divergent flows challenge conventional theories of energy cascades and particle dispersion. Lagrangian observations are a promising platform to capture the temporal evolution and particle-statistics hard to come by with other observations. The results and conclusions of this thesis provide insights into submesoscale turbulence by identifying the

limitations of using surface drifters to estimate sought after Eulerian statistics, as well as offering corrected observational constraints on important parameters needed to model tracer transport and dispersion by mesoscale eddies.

Future work is necessary to improve our understanding of processes that occur in an anisotropic, heterogeneous, and non-stationary ocean. All Chapters highlight the tendency of drifters to preferentially sample features with statistics distinct from other parts of the flow field, as well as statistics that vary along the paths they travel. In Chapter 3, a correction method to account for heterogeneity in the flow field is introduced and applies to correct both second- and third-order structure functions. Chapter 4 introduces a similar method that also encapsulates nonstationarity. While these correction methods are steps towards developing techniques suitable for realistic ocean conditions, they are not exhaustive, and come with their own limitations. Entirely new structure functions, where anisotropy is built in, are desirable. Additionally, many tracers such as oil and nutrients are not conservative, but feature chemical or biological reactions in addition to advection and diffusion. Active research by the author and others is underway to this end (Pearson and Fox-Kemper, In Prep; Pearson et al., In Prep). The results of those studies will increase understanding of energy dissipation and reactive tracer variance reduction across scales, with significant applications for oil and biogeochemical modelling.

Bibliography

Anderson, S.P., Sharma, N., 2008. Satellite-tracked drifter measurements of inertial currents in the gulf of mexico, in: 2008 IEEE/OES 9th Working Conference on Current Measurement Technology, IEEE. pp. 285–288.

Andersson, A., Fennig, K., Klepp, C., Bakan, S., Graßl, H., Schulz, J., 2010. The Hamburg ocean atmosphere parameters and fluxes from satellite data–hoaps-3. Earth System Science Data 2, 215–234.

Andrews, D., Hoskins, B., 1978. Energy spectra predicted by semi-geostrophic theories of frontogenesis. Journal of the atmospheric sciences 35, 509–512.

Babiano, A., Basdevant, C., Le Roy, P., Sadourny, R., 1987. Single-particle dispersion, lagrangian structure function and lagrangian energy spectrum in two-dimensional incompressible turbulence. Journal of marine research 45, 107–131.

Babiano, A., Basdevant, C., Sadourny, R., 1985. Structure functions and dispersion laws in two-dimensional turbulence. J. Atmos. Sci. 42, 941–949.

Bachman, S.D., Fox-Kemper, B., Bryan, F.O., 2015. A tracer-based inversion method for diagnosing eddy-induced diffusivity and advection. Ocean Modelling 86, 1–14.

Bachman, S.D., Fox-Kemper, B., Pearson, B., 2017. A scale-aware subgrid model for quasi-geostrophic turbulence. Journal of Geophysical Research: Oceans 122, 1529–1554.

Bacosa, H.P., Liu, Z., Erdner, D.L., 2015. Natural sunlight shapes crude oil-degrading bacterial communities in northern gulf of mexico surface waters. Frontiers in microbiology 6, 1325.

Badin, G., 2013. Surface semi-geostrophic dynamics in the ocean. Geophysical & Astrophysical Fluid Dynamics 107, 526–540.

Balwada, D., LaCasce, J.H., Speer, K.G., 2016. Scale-dependent distribution of kinetic energy from surface drifters in the gulf of mexico. Geophysical Research Letters 43, 10–856.

Barkan, R., McWilliams, J.C., Molemaker, M.J., Choi, J., Srinivasan, K., Shchepetkin, A.F., Bracco, A., 2017a. Submesoscale dynamics in the northern gulf of mexico. part ii: Temperature–salinity relations and cross-shelf transport processes. Journal of Physical Oceanography 47, 2347–2360.

Barkan, R., McWilliams, J.C., Shchepetkin, A.F., Molemaker, M.J., Renault, L., Bracco, A., Choi, J., 2017b. Submesoscale dynamics in the northern gulf of mexico. part i: Regional and seasonal characterization and the role of river outflow. Journal of Physical Oceanography 47, 2325–2346.

Barrick, D.E., Peake, W.H., 1968. A review of scattering from surfaces with different roughness scales. Radio Sci. 3, 865–868.

Batchelor, G., 1949. Diffusion in a field of homogeneous turbulence. i. eulerian analysis. Australian Journal of Chemistry 2, 437–450.

Batchelor, G., 1953. Theory of Homogeneous Turbulence. Cambridge University Press, Cambridge.

Batchelor, G.K., 1959. Small-scale variation of convected quantities like temperature in turbulent fluid part 1. general discussion and the case of small conductivity. Journal of Fluid Mechanics 5, 113–133.

Baumert, H.Z., Simpson, J., Simpson, J.H., Sundermann, J., Sündermann, J., 2005. Marine turbulence: theories, observations, and models. Cambridge University Press.

Bennett, A., 1984. Relative dispersion: Local and nonlocal dynamics. Journal of the atmospheric sciences 41, 1881–1886.

Bennett, A., et al., 2006. Lagrangian fluid dynamics. Cambridge University Press.

Bennett, A.F., 1987. A lagrangian analysis of turbulent diffusion. Reviews of Geophysics 25, 799–822.

Berloff, P.S., McWilliams, J.C., 2002. Material transport in oceanic gyres. part ii: Hierarchy of stochastic models. Journal of Physical Oceanography 32, 797–830.

Beron-Vera, F.J., LaCasce, J., 2016. Statistics of simulated and observed pair separations in the Gulf of Mexico. J. Phys. Oceanogr. 46, 2183–2199.

Blumen, W., 1978. Uniform potential vorticity flow: Part i. theory of wave interactions and two-dimensional turbulence. Journal of the Atmospheric Sciences 35, 774–783.

Boccaletti, G., Ferrari, R., Fox-Kemper, B., 2007. Mixed layer instabilities and restratification. Journal of Physical Oceanography 37, 2228–2250.

Boyd, J.P., 1992. The energy spectrum of fronts: Time evolution of shocks in burgers equation. Journal of the atmospheric sciences 49, 128–139.

Brannigan, L., Marshall, D.P., Naveira-Garabato, A., Nurser, A.G., 2015. The seasonal cycle of submesoscale flows. Ocean Modelling 92, 69–84.

Braun, N., Ziemer, F., Bezuglov, A., Cysewski, M., Schymura, G., 2008. Sea-surface current features observed by Doppler radar. IEEE Trans. Geosci. Remote Sens. 46, 1125–1133.

Brickman, D., Smith, P., 2002. Lagrangian stochastic modeling in coastal oceanography. Journal of atmospheric and oceanic technology 19, 83–99.

Bryan, K., 1982. Poleward heat transport by the ocean: Observations and models. Annual Review of Earth and Planetary Sciences 10, 15–38.

Bryden, H.L., Brady, E.C., 1989. Eddy momentum and heat fluxes and their effects on the circulation of the equatorial pacific ocean. Journal of Marine Research 47, 55–79.

Buckingham, C.E., Naveira Garabato, A.C., Thompson, A.F., Brannigan, L., Lazar, A., Marshall, D.P., George Nurser, A.J., Damerell, G., Heywood, K.J., Belcher, S.E., 2016. Seasonality of submesoscale flows in the ocean surface boundary layer. Geophysical Research Letters 43, 2118–2126.

Buesseler, K.O., Jayne, S.R., Fisher, N.S., Rypina, I.I., Baumann, H., Baumann, Z., Breier, C.F., Douglass, E.M., George, J., Macdonald, A.M., et al., 2012. Fukushima-derived radionuclides in the ocean and biota off japan. Proceedings of the National Academy of Sciences 109, 5984–5988.

Bühler, O., Callies, J., Ferrari, R., 2014. Wave–vortex decomposition of one-dimensional ship-track data. Journal of Fluid Mechanics 756, 1007–1026.

Callies, J., Ferrari, R., 2013. Interpreting energy and tracer spectra of upper-ocean turbulence in the submesoscale range (1–200 km). Journal of Physical Oceanography 43, 2456–2474.

Callies, J., Ferrari, R., Bühler, O., 2014. Transition from geostrophic turbulence to inertia–gravity waves in the atmospheric energy spectrum. Proceedings of the National Academy of Sciences 111, 17033–17038.

Callies, J., Ferrari, R., Klymak, J.M., Gula, J., 2015. Seasonality in submesoscale turbulence. Nature communications 6, 1–8.

Campana, J., Terrill, E.J., de Paolo, T., 2017. A new inversion method to obtain upper-ocean current-depth profiles using X-band observations of deep-water waves. J. Atmos. Oceanic Technol. 34, 957–970.

Cao, H., Jing, Z., Fox-Kemper, B., Yan, T., Qi, Y., 2019. Scale transition from geostrophic motions to internal waves in the northern south china sea. Journal of Geophysical Research: Oceans 124, 9364–9383.

Capet, X., Campos, E., Paiva, A., 2008a. Submesoscale activity over the Argentinian shelf. Geophys. Res. Lett. 35.

Capet, X., McWilliams, J.C., Molemaker, M.J., Shchepetkin, A., 2008b. Mesoscale to submesoscale transition in the california current system. part i: Flow structure, eddy flux, and observational tests. Journal of physical oceanography 38, 29–43.

Capet, X., McWilliams, J.C., Molemaker, M.J., Shchepetkin, A., 2008c. Mesoscale to submesoscale transition in the California Current System. Part III: Energy balance and flux. J. Phys. Oceanogr. 38, 2256–2269.

Carlson, J.A., Jaffe, A., Wiles, A., 2006. The millennium prize problems. American Mathematical Society Providence, RI.

Carrier, M.J., Ngodock, H., Smith, S., Jacobs, G., Muscarella, P., Özgökmen, T., Haus, B., Lipphardt, B., 2014a. Impact of assimilating ocean velocity observations inferred from lagrangian drifter data using the ncom-4dvar. Monthly Weather Review 142, 1509–1524.

Carrier, M.J., Ngodock, H., Smith, S., Jacobs, G., Muscarella, P., Özgökmen, T., Haus, B., Lipphardt, B., 2014b. Impact of assimilating ocean velocity observations inferred from lagrangian drifter data using the ncom-4dvar. Monthly Weather Review 142, 1509–1524.

Chang, H., Huntley, H.S., Kirwan Jr., A.D., Carlson, D.F., Mensa, J.A., Mehta, S., Novelli, G., Özgökmen, T.M., Fox-Kemper, B., Pearson, B., Pearson, J., Harcourt, R., Poje, A.C., 2019. Small-scale dispersion in the presence of Langmuir circulation. J. Phys. Oceanogr. In Press.

Charney, J.G., 1971. Geostrophic Turbulence. Journal of Atmospheric Sciences 28, 1087–1094.

Chelton, D.B., deSzoeke, R.A., Schlax, M.G., Naggar, K.E., Siwertz, N., 1998. Geographical variability of the first baroclinic rossby radius of deformation. Journal of Physical Oceanography 28, 433–460.

Chelton, D.B., Schlax, M.G., Samelson, R.M., 2011. Global observations of nonlinear mesoscale eddies. Progress in oceanography 91, 167–216.

Chelton, D.B., Schlax, M.G., Samelson, R.M., de Szoeke, R.A., 2007. Global observations of large oceanic eddies. Geophysical Research Letters 34.

Chereskin, T.K., Rocha, C.B., Gille, S.T., Menemenlis, D., Passaro, M., 2019. Characterizing the transition from balanced to unbalanced motions in the southern california current. Journal of Geophysical Research: Oceans 124, 2088–2109.

Choi, J., Bracco, A., Barkan, R., Shchepetkin, A.F., McWilliams, J.C., Molemaker, J.M., 2017. Submesoscale dynamics in the northern gulf of mexico. part iii: Lagrangian implications. Journal of Physical Oceanography 47, 2361–2376.

Corrsin, S., 1963. Estimates of the relations between eulerian and lagrangian scales in large reynolds number turbulence. Journal of the Atmospheric Sciences 20, 115–119.

Crone, T.J., Tolstoy, M., 2010. Magnitude of the 2010 gulf of mexico oil leak. Science 330, 634–634.

Cushman-Roisin, B., Manga, M., 1995. Introduction to geophysical fluid dynamics. Pure and Applied Geophysics 144, 177–178.

Daling, P.S., Moldestad, M.Ø., Johansen, Ø., Lewis, A., Rødal, J., 2003. Norwegian testing of emulsion properties at sea—-the importance of oil type and release conditions. Spill Science & Technology Bulletin 8, 123–136.

D'Asaro, E., Lee, C., Rainville, L., Harcourt, R., Thomas, L., 2011. Enhanced turbulence and energy dissipation at ocean fronts. Science 332, 318–322.

D'Asaro, E.A., Shcherbina, A.Y., Klymak, J.M., Molemaker, J., Novelli, G., Guigand, C.M., Haza, A.C., Haus, B.K., Ryan, E.H., Jacobs, G.A., Huntley, H.S., Laxague, N.J.M., Chen, S., Judt, F., McWilliams, J.C., Barkan, R., Kirwan, A.D., Poje, A.C., Özgökmen, T.M., 2018. Ocean convergence and the dispersion of flotsam. P. Natl. Acad. Sci. USA 115, 1162.

Davidson, P., Pearson, B., 2005. Identifying turbulent energy distributions in real, rather than fourier, space. Physical review letters 95, 214501.

Davis, R.E., 1987. Modeling eddy transport of passive tracers. Journal of Marine Research 45, 635–666.

Davis, R.E., 1991a. Lagrangian ocean studies. Annual Review of Fluid Mechanics 23, 43–64.

Davis, R.E., 1991b. Observing the general circulation with floats. Deep Sea Research Part A. Oceanographic Research Papers 38, S531–S571.

De Dominicis, M., Leuzzi, G., Monti, P., Pinardi, N., Poulain, P.M., 2012. Eddy diffusivity derived from drifter data for dispersion model applications. Ocean Dynamics 62, 1381–1398.

De Karman, T., Howarth, L., 1938. On the statistical theory of isotropic turbulence. Proceedings of the Royal Society of London. Series A-Mathematical and Physical Sciences 164, 192–215.

DiMarco, S.F., Howard, M.K., Reid, R.O., 2000. Seasonal variation of wind-driven diurnal current cycling on the texas-louisiana continental shelf. Geophysical Research Letters 27, 1017–1020.

Early, J.J., Samelson, R., Chelton, D.B., 2011. The evolution and propagation of quasigeostrophic ocean eddies. Journal of Physical Oceanography 41, 1535–1555.

Eckart, C., 1948. An analysis of stirring and mixing processes in incompressible fluids. Journal of Marine Research 7, 265–275.

Einstein, A., 1906. On the theory of the brownian movement. Ann. Phys 19, 371–381.

Einstein, A., 1956. Investigations on the Theory of the Brownian Movement. Courier Corporation.

Ekman, V.W., 1905. On the influence of the earth's rotation on ocean-currents. .

Eyink, G.L., Sreenivasan, K.R., 2006. Onsager and the theory of hydrodynamic turbulence. Reviews of modern physics 78, 87.

Faksness, L.G., Brandvik, P.J., Daling, P.S., Singsaas, I., Sørstrøm, S.E., 2016. The value of offshore field experiments in oil spill technology development for norwegian waters. Marine pollution bulletin 111, 402–410.

Falco, P., Griffa, A., Poulain, P.M., Zambianchi, E., 2000. Transport properties in the adriatic sea as deduced from drifter data. Journal of Physical Oceanography 30, 2055–2071.

Falkovich, G., Gawdzki, K., Vergassola, M., 2001. Particles and fields in fluid turbulence. Reviews of modern Physics 73, 913.

Ferrari, R., Wunsch, C., 2009. Ocean circulation kinetic energy: Reservoirs, sources, and sinks. Annual Review of Fluid Mechanics 41, 253–282.

Fingas, M., 2011. Buoys and devices for oil spill tracking, in: International Oil Spill Conference Proceedings (IOSC), American Petroleum Institute. p. abs9.

Fox-Kemper, B., Danabasoglu, G., Ferrari, R., Griffies, S., Hallberg, R., Holland, M., Maltrud, M., Peacock, S., Samuels, B., 2011. Parameterization of mixed layer eddies. iii: Implementation and impact in global ocean climate simulations. Ocean Modelling 39, 61–78.

Fox-Kemper, B., Ferrari, R., Pedlosky, J., 2003. On the indeterminacy of rotational and divergent eddy fluxes. Journal of Physical Oceanography 33, 478–483.

Fox-Kemper, B., Lumpkin, R., Bryan, F., 2013. Lateral transport in the ocean interior, in: International Geophysics. Elsevier. volume 103, pp. 185–209.

Freeland, H., PB, R., et al., 1975. Statistical observations of the trajectories of neutrally buoyant floats in the north atlantic. .

Frehlich, R., Sharman, R., 2010. Climatology of velocity and temperature turbulence statistics determined from rawinsonde and acars/amdar data. Journal of Applied Meteorology and Climatology 49, 1149–1169.

Frisch, U., 1995. Turbulence: the legacy of A. N. Kolmogorov. Cambridge University Press.

Gage, K., Nastrom, G., 1986. Theoretical interpretation of atmospheric wavenumber spectra of wind and temperature observed by commercial aircraft during gasp. Journal of the atmospheric sciences 43, 729–740.

Gibson, C., Schwarz, W., 1963. The universal equilibrium spectra of turbulent velocity and scalar fields. Journal of Fluid Mechanics 16, 365–384.

Gough, M.K., Reniers, A., MacMahan, J.H., Howden, S.D., 2016. Resonant near-surface inertial oscillations in the northeastern gulf of mexico. Journal of Geophysical Research: Oceans 121, 2163–2182.

Grant, H., Stewart, R., Moilliet, A., 1962. Turbulence spectra from a tidal channel. Journal of Fluid Mechanics 12, 241–268.

Griesel, A., Gille, S.T., Sprintall, J., McClean, J.L., LaCasce, J.H., Maltrud, M.E., 2010. Isopycnal diffusivities in the antarctic circumpolar current inferred from lagrangian floats in an eddying model. Journal of Geophysical Research: Oceans 115.

Griesel, A., McClean, J., Gille, S., Sprintall, J., Eden, C., 2014. Eulerian and lagrangian isopycnal eddy diffusivities in the southern ocean of an eddying model. Journal of physical oceanography 44, 644–661.

Griffa, A., 1996. Applications of stochastic particle models to oceanographic problems, in: Stochastic modelling in physical oceanography. Springer, pp. 113–140.

Griffa, A., Kirwan Jr, A., Mariano, A.J., Özgökmen, T., Rossby, H.T., 2007. Lagrangian analysis and prediction of coastal and ocean dynamics. Cambridge University Press.

Griffa, A., Lumpkin, R., Veneziani, M., 2008. Cyclonic and anticyclonic motion in the upper ocean. Geophysical Research Letters 35.

Griffies, S.M., Adcroft, A.J., 2008. Formulating the equations of ocean models. Ocean modeling in an eddying regime 177, 281–317.

Grötsch, P., 2018. Environmental forcing of aquatic ecosystem variability: A matter of perspective .

Haidvogel, D., Blanton, J., Kindle, J., Lynch, D., 2000. Coastal ocean modeling: Processes and real-time systems. Oceanography 13, 35–46.

Hayworth, J., Clement, T., Valentine, J., 2011. Deepwater horizon oil spill impacts on alabama beaches. Hydrology & Earth System Sciences 15.

Haza, A., Özgökmen, T., Griffa, A., Ryan, E., 2014. Implementation of lagrangian stochastic models to parameterize submesoscale transport for tracking oil spills in the gulf of mexico, us department of the interior, bureau of ocean energy management, boem 2014-053. Herndon, VA, February .

Haza, A.C., D'Asaro, E., Chang, H., Chen, S., Curcic, M., Guigand, C., Huntley, H.S., Jacobs, G., Novelli, G., Özgökmen, T.M., Poje, A.C., Ryan, E., Shcherbina, A., 2018. Drogue-Loss Detection for Surface Drifters during the Lagrangian Submesoscale Experiment (LASER). Journal of Atmospheric and Oceanic Technology 35, 705–725.

Held, I.M., Pierrehumbert, R.T., Garner, S.T., Swanson, K.L., 1995. Surface quasi-geostrophic dynamics. Journal of Fluid Mechanics 282, 1–20.

Hoskins, B.J., Bretherton, F.P., 1972. Atmospheric frontogenesis models: Mathematical formulation and solution. Journal of the Atmospheric Sciences 29, 11–37.

Howard, L.N., 1961. Note on a paper of john w. miles. Journal of Fluid Mechanics 10, 509–512.

Huntley, H.S., Lipphardt Jr, B., Kirwan Jr, A., 2019. Anisotropy and inhomogeneity in drifter dispersion. Journal of Geophysical Research: Oceans .

Jarosz, E., Hallock, Z., Teague, W.J., 2007. Near-inertial currents in the desoto canyon region. Continental Shelf Research 27, 2407–2426.

Jiménez, J., 2004. The contributions of an kolmogorov to the theory of turbulence. Arbor 178, 589–606.

Johnson, L., Lee, C.M., D'Asaro, E.A., 2016. Global estimates of lateral springtime restratification. J. Phys. Oceanogr. 46, 1555–1573.

Jones, C.E., Dagestad, K.F., Breivik, Ø., Holt, B., Röhrs, J., Christensen, K.H., Espeseth, M., Brekke, C., Skrunes, S., 2016. Measurement and modeling of oil slick transport. Journal of Geophysical Research: Oceans 121, 7759–7775.

Juckes, M., 1995. Instability of surface and upper-tropospheric shear lines. Journal of the atmospheric sciences 52, 3247–3262.

Kamenkovich, I., Rypina, I.I., Berloff, P., 2015. Properties and origins of the anisotropic eddy-induced transport in the north atlantic. Journal of Physical Oceanography 45, 778–791.

Klein, P., Hua, B.L., Lapeyre, G., Capet, X., Le Gentil, S., Sasaki, H., 2008. Upper ocean turbulence from high-resolution 3d simulations. Journal of Physical Oceanography 38, 1748–1763.

Klein, P., Lapeyre, G., 2009. The oceanic vertical pump induced by mesoscale and submesoscale turbulence. Annu. Rev. Mar. Sci. 1, 351–375.

Klein, P., Lapeyre, G., Roullet, G., Le Gentil, S., Sasaki, H., 2011. Ocean turbulence at meso and submesoscales: connection between surface and interior dynamics. Geophysical & Astrophysical Fluid Dynamics 105, 421–437.

Klocker, A., Ferrari, R., LaCasce, J.H., Merrifield, S.T., 2012. Reconciling float-based and tracer-based estimates of lateral diffusivities. Journal of Marine Research 70, 569–602.

Kolmogorov, A.N., 1941a. Dissipation of energy in locally isotropic turbulence, in: Akademiia Nauk SSSR Doklady, p. 16.

Kolmogorov, A.N., 1941b. The local structure of turbulence in incompressible viscous fluid for very large Reynolds numbers. Cr Acad. Sci. URSS 30, 301–305.

Koszalka, I., LaCasce, J., Andersson, M., Orvik, K., Mauritzen, C., 2011. Surface circulation in the nordic seas from clustered drifters. Deep Sea Research Part I: Oceanographic Research Papers 58, 468–485.

Kraichnan, R.H., 1967. Inertial ranges in two-dimensional turbulence. The Physics of Fluids 10, 1417–1423.

Kraichnan, R.H., 1971. Inertial-range transfer in two- and three-dimensional turbulence. Journal of Fluid Mechanics 47, 525–535.

Kramer, W., Keetels, G., Clercx, H., van Heijst, G., 2011. Structure-function scaling of bounded two-dimensional turbulence. Physical Review E 84, 026310.

Krauß, W., Böning, C.W., 1987. Lagrangian properties of eddy fields in the northern north atlantic as deduced from satellite-tracked buoys. Journal of Marine Research 45, 259–291.

Kullback, S., Leibler, R.A., 1951. On information and sufficiency. The annals of mathematical statistics 22, 79–86.

Kunze, E., 2019. A unified model spectrum for anisotropic stratified and isotropic turbulence in the ocean and atmosphere. Journal of Physical Oceanography 49, 385–407.

LaCasce, J., 2000. Floats and f/h. Journal of Marine Research 58, 61–95.

LaCasce, J., 2008. Statistics from lagrangian observations. Progress in Oceanography 77, 1–29.

LaCasce, J., 2016. Estimating Eulerian Energy Spectra from Drifters. Fluids 1, 33.

LaCasce, J., Bower, A., 2000. Relative dispersion in the subsurface north atlantic. Journal of marine research 58, 863–894.

LaCasce, J.H., Mahadevan, A., 2006. Estimating subsurface horizontal and vertical velocities from sea-surface temperature. Journal of Marine Research 64, 695–721.

Lapeyre, G., Klein, P., Hua, B.L., 2006. Oceanic restratification forced by surface frontogenesis. Journal of Physical Oceanography 36, 1577–1590.

Large, W., Yeager, S., 2009. The global climatology of an interannually varying air–sea flux data set. Climate Dyn. 33, 341–364.

Lévy, M., Franks, P.J., Smith, K.S., 2018. The role of submesoscale currents in structuring marine ecosystems. Nature communications 9, 4758.

Li, Q.P., Franks, P.J., Ohman, M.D., Landry, M.R., 2012. Enhanced nitrate fluxes and biological processes at a frontal zone in the southern California current system. J. Plankton Res. 34, 790–801.

Lindborg, E., 1996. A note on Kolmogorov's third-order structure-function law, the local isotropy hypothesis and the pressure–velocity correlation. Journal of Fluid Mechanics 326, 343.

Lindborg, E., 1999. Can the atmospheric kinetic energy spectrum be explained by two-dimensional turbulence? J. Fluid Mech. 388, 259–288.

Lindborg, E., 2005. The effect of rotation on the mesoscale energy cascade in the free atmosphere. Geophysical research letters 32.

Lindborg, E., 2006. The energy cascade in a strongly stratified fluid. Journal of Fluid Mechanics 550, 207–242.

Lindborg, E., 2007. Third-order structure function relations for quasi-geostrophic turbulence. J. Fluid Mech. 572, 255–260.

Lindborg, E., 2015. A helmholtz decomposition of structure functions and spectra calculated from aircraft data. Journal of Fluid Mechanics 762.

Lindborg, E., Cho, J.Y., 2001. Horizontal velocity structure functions in the upper troposphere and lower stratosphere: 2. theoretical considerations. Journal of Geophysical Research: Atmospheres 106, 10233–10241.

Lindborg, E., Cho, J.Y.N., 2000. Determining the Cascade of Passive Scalar Variance in the Lower Stratosphere. Physical Review Letters 85, 5663–5666.

Liu, L., Peng, S., Wang, J., Huang, R.X., 2014. Retrieving density and velocity fields of the ocean's interior from surface data. Journal of Geophysical Research: Oceans 119, 8512–8529.

Liu, Y., Weisberg, R.H., Hu, C., Zheng, L., 2011. Tracking the deepwater horizon oil spill: A modeling perspective. Eos, Transactions American Geophysical Union 92, 45–46.

Lumley, J.L., 1964. The spectrum of nearly inertial turbulence in a stably stratified fluid. Journal of the Atmospheric Sciences 21, 99–102.

Lumpkin, R., Flament, P., 2001. Lagrangian statistics in the central north pacific. Journal of Marine Systems 29, 141–155.

Lund, B., Graber, H.C., Tamura, H., Collins III, C.O., Varlamov, S.M., 2015. A new technique for the retrieval of near-surface vertical current shear from marine X-band radar images. J. Geophys. Res. 120, 8466–8486.

Lund, B., Haus, B.K., Horstmann, J., Graber, H.C., Carrasco, R., Laxague, N.J.M., Novelli, G., Guigand, C.M., Özgökmen, T.M., 2018. Near-surface current mapping by shipboard marine x-band radar: A validation. J. Atmos. Oceanic Tech. 35, 1077–1090.

Luo, H., Bracco, A., Cardona, Y., McWilliams, J.C., 2016. Submesoscale circulation in the northern gulf of mexico: Surface processes and the impact of the freshwater river input. Ocean Modelling 101, 68 – 82.

Lyzenga, D.R., Walker, D.T., 2015. A simple model for marine radar images of the ocean surface. IEEE Geosci. Remote. S. 12, 2389–2392.

Mahadevan, A., Jaeger, G.S., Freilich, M., Omand, M.M., Shroyer, E.L., Sengupta, D., 2016. Freshwater in the bay of bengal: Its fate and role in air-sea heat exchange. Oceanography 29, 72–81.

Mahadevan, A., Tandon, A., 2006. An analysis of mechanisms for submesoscale vertical motion at ocean fronts. Ocean Model. 14, 241–256.

Malardel, S., Thorpe, A., Joly, A., 1997. Consequences of the geostrophic momentum approximation on barotropic instability. Journal of the atmospheric sciences 54, 103–112.

Manucharyan, G.E., Thompson, A.F., 2017. Submesoscale sea ice-ocean interactions in marginal ice zones. Journal of Geophysical Research: Oceans 122, 9455–9475.

Mariano, A.J., Ryan, E., Huntley, H., Laurindo, L., Coelho, E., Griffa, A., Özgökmen, T., Berta, M., Bogucki, D., Chen, S.S., et al., 2016. Statistical properties of the surface velocity field in the northern gulf of mexico sampled by glad drifters. Journal of Geophysical Research: Oceans 121, 5193–5216.

Mason, E., Molemaker, J., Shchepetkin, A.F., Colas, F., McWilliams, J.C., Sangrà, P., 2010. Procedures for offline grid nesting in regional ocean models. Ocean Modelling 35, 1–15.

McCaffrey, K., 2015a. Characterization of turbulence anisotropy, coherence, and intermittency at a prospective tidal energy site: Observational data analysis. Renewable Energy 76, 441–453.

McCaffrey, K., 2015b. Estimates of ocean macroturbulence: Structure function and spectral slope from argo profiling floats. Journal of Physical Oceanography 45, 1773–1793.

McComb, W.D., 1990. The physics of fluid turbulence. Chemical physics .

McGillicuddy, D.J., Anderson, L.A., Bates, N.R., Bibby, T., Buesseler, K.O., Carlson, C.A., Davis, C.S., Ewart, C., Falkowski, P.G., Goldthwait, S.A., et al., 2007. Eddy/wind interactions stimulate extraordinary mid-ocean plankton blooms. Science 316, 1021–1026.

McKiver, W., Dritschel, D., 2008. Balance in non-hydrostatic rotating stratified turbulence. Journal of Fluid Mechanics 596, 201–219.

McWilliams, J.C., 1985. A Uniformly Valid Model Spanning the Regimes of Geostrophic and Isotropic, Stratified Turbulence: Balanced Turbulence. Journal of Atmospheric Sciences 42, 1773–1773.

McWilliams, J.C., 2003. Diagnostic force balance and its limits, in: Nonlinear processes in geophysical fluid dynamics. Springer, pp. 287–303.

McWilliams, J.C., 2008. Fluid dynamics at the margin of rotational control. Environ Fluid Mech. 8, 441–449.

McWilliams, J.C., 2016. Submesoscale currents in the ocean. P. Roy. Soc. A 472, 20160117.

McWilliams, J.C., 2019. A survey of submesoscale currents. Geoscience Letters 6, 1–15.

McWilliams, J.C., Molemaker, J., Yavneh, I., 2001. From stirring to mixing of momentum: Cascades from balanced flows to dissipation in the oceanic interior. Technical Report. CALIFORNIA UNIV LOS ANGELES INST OF GEOPHYSICS AND PLANETARY PHYSICS.

Mensa, J.A., Garraffo, Z., Griffa, A., Özgökmen, T.M., Haza, A., Veneziani, M., 2013. Seasonality of the submesoscale dynamics in the gulf stream region. Ocean Dynamics 63, 923–941.

Miles, J.W., 1961. On the stability of heterogeneous shear flows. Journal of Fluid Mechanics 10, 496–508.

Molemaker, M.J., McWilliams, J.C., Yavneh, I., 2005. Baroclinic instability and loss of balance. J. Phys. Oceanogr. 35, 1505–1517.

Moore, D., Craig, B., McCabe, G., 2014. Introduction to the Practice of Statistics. W.H. Freeman.

Nastrom, G., Gage, K., Jasperson, W., 1984. Kinetic energy spectrum of large-and mesoscale atmospheric processes. Nature 310, 36–38.

Nieto Borge, J.C., Rodríquez Rodríguez, G., Hessner, K., Izquierdo González, P., 2004. Inversion of marine radar images for surface wave analysis. J. Atmos. Oceanic Technol. 21, 1291–1300.

Nilsson, J.A., Döös, K., Ruti, P.M., Artale, V., Coward, A., Brodeau, L., 2013. Observed and modeled global ocean turbulence regimes as deduced from surface trajectory data. Journal of physical oceanography 43, 2249–2269.

North, E.W., Adams, E.E., Schlag, S., Sherwood, C.R., He, R., Socolofsky, S., 2011. Simulating oil droplet dispersal from the deepwater horizon spill with a lagrangian approach. AGU Book Series: Monitoring and Modeling the Deepwater Horizon Oil Spill: A Record-Breaking Enterprise .

Novelli, G., Guigand, C.M., Boufadel, M.C., Özgökmen, T.M., 2020. On the transport and landfall of marine oil spills, laboratory and field observations. Marine Pollution Bulletin 150, 110805.

Novelli, G., Guigand, C.M., Cousin, C., Ryan, E.H., Laxague, N.J.M., Dai, H., Haus, B.K., Özgökmen, T.M., 2017. A biodegradable surface drifter for ocean sampling on a massive scale. J. Atmos. Oceanic Tech. 34, 2509–2532.

Novelli, G., Guigand, C.M., Özgökmen, T.M., 2018. Technological advances in drifters for oil transport studies. Marine Technology Society Journal 52, 53–61.

Obukhov, A., 1941. Spectral energy distribution in a turbulent flow. Izv. Akad. Nauk. SSSR. Ser. Geogr. i. Geofiz 5, 453–466.

Ohlmann, J., Molemaker, M., Baschek, B., Holt, B., Marmorino, G., Smith, G., 2017. Drifter observations of submesoscale flow kinematics in the coastal ocean. Geophys. Res. Lett. 44, 330–337.

Ohlmann, J.C., Niiler, P.P., 2005. Circulation over the continental shelf in the northern gulf of mexico. Progress in oceanography 64, 45–81.

Omand, M.M., D'Asaro, E.A., Lee, C.M., Perry, M.J., Briggs, N., Cetinić, I., Mahadevan, A., 2015. Eddy-driven subduction exports particulate organic carbon from the spring bloom. Science 348, 222–225.

Onsager, L., 1945. The distribution of energy in turbulence. Minutes of the Meeting of the Metropolitan Section held at Columbia Physical Review 68, 286.

Orfila, A., Molcard, A., Sayol, J.M., Marmain, J., Bellomo, L., Quentin, C., Barbin, Y., 2014. Empirical forecasting of hf-radar velocity using genetic algorithms. IEEE Transactions on Geoscience and Remote Sensing 53, 2875–2886.

Özgökmen, T.M., Chassignet, E.P., Dawson, C.N., Dukhovskoy, D., Jacobs, G., Ledwell, J., Garcia-Pineda, O., MacDonald, I.R., Morey, S.L., Olascoaga, M.J., et al., 2016. Over what area did the oil and gas spread during the 2010 deepwater horizon oil spill? Oceanography 29, 96–107.

Passow, U., Ziervogel, K., Asper, V., Diercks, A., 2012. Marine snow formation in the aftermath of the deepwater horizon oil spill in the gulf of mexico. Environmental Research Letters 7, 035301.

Pearson, B., Fox-Kemper, B., 2018. Log-normal turbulence dissipation in global ocean models. Phys. Rev. Lett. 120, 094501.

Pearson, B., Pearson, J., Fox-Kemper, B., In Prep. Relation between structure functions and cascade rates in anisotropic geophysical turbulence. Phys. Rev. Lett. .

Pearson, J., Fox-Kemper, B., In Prep. Blended second-order structure function laws for passive-reactive tracers in geophysical flows. Journal of Physical Oceanography .

Pearson, J., Fox-Kemper, B., Barkan, R., Choi, J., Bracco, A., McWilliams, J.C., 2019. Impacts of convergence on structure functions from surface drifters in the Gulf of Mexico. J. Phys. Oceanogr. 49, 675–690.

Pearson, J., Fox-Kemper, B., Pearson, B., Chang, H., Haus, B.K., Horstmann, J., Huntley, H.S., Kirwan, Jr., A.D., Lund, B., , Poje, A., 2020. Biases in structure functions from observations of submesoscale flows. Journal of Geophysical Research: Oceans Under Review.

Peng, S., Qian, Y.K., Lumpkin, R., Li, P., Wang, D., Du, Y., 2015. Characteristics of the near-surface currents in the indian ocean as deduced from satellite-tracked surface drifters. part ii: Lagrangian statistics. Journal of Physical Oceanography 45, 459–477.

du Plessis, M., Swart, S., Ansorge, I.J., Mahadevan, A., Thompson, A.F., 2019. Southern ocean seasonal restratification delayed by submesoscale wind-front interactions. J. Phys. Oceanogr. .

Poje, A.C., Özgökmen, T.M., Bogucki, D.J., Kirwan, A.D., 2017. Evidence of a forward energy cascade and Kolmogorov self-similarity in submesoscale ocean surface drifter observations. Phys. Fluids 29, 020701.

Poje, A.C., Özgökmen, T.M., Lipphardt, B.L., Haus, B.K., Ryan, E.H., Haza, A.C., Jacobs, G.A., Reniers, A.J.H.M., Olascoaga, M.J., Novelli, G., Griffa, A., Beron-Vera, F.J., Chen, S.S., Coelho, E., Hogan, P.J., Kirwan, A.D., Huntley, H.S., Mariano, A.J., 2014. Submesoscale dispersion in the vicinity of the Deepwater Horizon spill. Proc. Natl. Acad. Sci. USA 111, 12693.

Pollard, R.T., Millard Jr, R., 1970. Comparison between observed and simulated wind-generated inertial oscillations, in: Deep Sea Research and Oceanographic Abstracts, Elsevier. pp. 813–821.

Pope, S.B., 2000. Turbulent Flows. Cambridge University Press.

Poulain, P.M., 2001. Adriatic sea surface circulation as derived from drifter data between 1990 and 1999. Journal of Marine Systems 29, 3–32.

Press, W.H., Rybicki, G.B., 1989. Fast algorithm for spectral analysis of unevenly sampled data. The Astrophysical Journal 338, 277–280.

Qiu, B., Nakano, T., Chen, S., Klein, P., 2017. Submesoscale transition from geostrophic flows to internal waves in the northwestern pacific upper ocean. Nature communications 8, 1–10.

Ragone, F., Badin, G., 2016. A study of surface semi-geostrophic turbulence: freely decaying dynamics. Journal of Fluid Mechanics 792, 740–774.

Redi, M.H., 1982. Oceanic isopycnal mixing by coordinate rotation. Journal of Physical Oceanography 12, 1154–1158.

Reed, M., Johansen, Ø., Brandvik, P.J., Daling, P., Lewis, A., Fiocco, R., Mackay, D., Prentki, R., 1999. Oil spill modeling towards the close of the 20th century: overview of the state of the art. Spill Science & Technology Bulletin 5, 3–16.

Reed, M., Turner, C., Odulo, A., 1994. The role of wind and emulsification in modelling oil spill and surface drifter trajectories. Spill Science & Technology Bulletin 1, 143–157.

Restrepo, J., Sankar, V., Dawson, C., 2014. Nearshore sticky waters. Ocean Modelling 80, 49 – 58.

Reynolds, O., 1883. Xxix. an experimental investigation of the circumstances which determine whether the motion of water shall be direct or sinuous, and of the law of resistance in parallel channels. Philosophical Transactions of the Royal society of London , 935–982.

Richardson, L.F., 1922. Weather prediction by numerical process. Cambridge University Press.

Richardson, L.F., 1926. Atmospheric diffusion shown on a distance-neighbour graph. Proceedings of the Royal Society of London. Series A, Containing Papers of a Mathematical and Physical Character 110, 709–737.

Riley, J.J., Lindborg, E., 2008. Stratified turbulence: A possible interpretation of some geophysical turbulence measurements. Journal of the atmospheric sciences 65, 2416–2424.

Riser, S.C., 1982. The quasi-Lagrangian nature of SOFAR floats. Deep-Sea Res. 29, 1587–1602.

Risien, C.M., Chelton, D.B., 2008. A global climatology of surface wind and wind stress fields from eight years of quikscat scatterometer data. J. Phys. Oceanogr. 38, 2379–2413.

Rocha, C.B., Chereskin, T.K., Gille, S.T., Menemenlis, D., 2016a. Mesoscale to submesoscale wavenumber spectra in drake passage. Journal of Physical Oceanography 46, 601–620.

Rocha, C.B., Gille, S.T., Chereskin, T.K., Menemenlis, D., 2016b. Seasonality of submesoscale dynamics in the kuroshio extension. Geophysical Research Letters 43, 11,304–11,311.

Rosso, I., Hogg, A.M., Strutton, P.G., Kiss, A.E., Matear, R., Klocker, A., van Sebille, E., 2014. Vertical transport in the ocean due to sub-mesoscale structures: Impacts in the kerguelen region. Ocean Modelling 80, 10–23.

Rypina, I.I., Fertitta, D., Macdonald, A., Yoshida, S., Jayne, S., 2017. Multi-iteration approach to studying tracer spreading using drifter data. Journal of Physical Oceanography 47, 339–351.

Rypina, I.I., Jayne, S.R., Yoshida, S., Macdonald, A.M., Buesseler, K., 2014. Drifter-based estimate of the 5 year dispersal of f ukushima-derived radionuclides. Journal of Geophysical Research: Oceans 119, 8177–8193.

Rypina, I.I., Kamenkovich, I., Berloff, P., Pratt, L.J., 2012. Eddy-induced particle dispersion in the near-surface north atlantic. Journal of Physical Oceanography 42, 2206–2228.

Rypina, I.I., Kirincich, A., Lentz, S., Sundermeyer, M., 2016. Investigating the eddy diffusivity concept in the coastal ocean. Journal of Physical Oceanography 46, 2201–2218.

Rypina, I.I., Pratt, L.J., Lozier, M.S., 2011. Near-surface transport pathways in the north atlantic ocean: Looking for throughput from the subtropical to the subpolar gyre. Journal of Physical Oceanography 41, 911–925.

Sallée, J., Speer, K., Morrow, R., Lumpkin, R., 2008. An estimate of lagrangian eddy statistics and diffusion in the mixed layer of the southern ocean. Journal of Marine Research 66, 441–463.

Salmon, R., 1978. Two-layer quasi-geostrophic turbulence in a simple special case. Geophysical & Astrophysical Fluid Dynamics 10, 25–52.

Sansón, L.Z., Pérez-Brunius, P., Sheinbaum, J., 2017. Point source dispersion of surface drifters in the southern gulf of mexico. Environmental Research Letters 12, 024006.

Schiller, R.V., Kourafalou, V.H., Hogan, P., Walker, N.D., 2011. The dynamics of the mississippi river plume: Impact of topography, wind and offshore forcing on the fate of plume waters. Journal of Geophysical Research: Oceans 116, n/a–n/a. C06029.

Senet, C.M., Seemann, J., Ziemer, F., 2001. The near-surface current velocity determined from image sequences of the sea surface. IEEE Trans. Geosci. Remote Sens. 39, 492–505.

Shchepetkin, A.F., McWilliams, J.C., 2005. The Regional Oceanic Modeling System: A split-explicit, free-surface, topography-following-coordinate oceanic model. Ocean Modelling 9, 347–404.

Siegelman, L., O'Toole, M., Flexas, M., Rivière, P., Klein, P., 2019. Submesoscale ocean fronts act as biological hotspot for southern elephant seal. Scientific reports 9, 5588.

Simpson, J.H., Sharples, J., 2012. Introduction to the physical and biological oceanography of shelf seas. Cambridge University Press.

Smith, K.M., Hamlington, P.E., Fox-Kemper, B., 2016. Effects of submesoscale turbulence on ocean tracers. Journal of Geophysical Research: Oceans 121, 908–933.

Solomon, H., 1971. On the representation of isentropic mixing in ocean circulation models. Journal of Physical Oceanography 1, 233–234.

Soufflet, Y., Marchesiello, P., Lemarié, F., Jouanno, J., Capet, X., Debreu, L., Benshila, R., 2016. On effective resolution in ocean models. Ocean Modelling 98, 36–50.

Spall, M.A., Richardson, P.L., Price, J., 1993. Advection and eddy mixing in the mediterranean salt tongue. Journal of Marine Research 51, 797–818.

Spaulding, M.L., 2017. State of the art review and future directions in oil spill modeling. Marine pollution bulletin 115, 7–19.

Sreenivasan, K.R., 1995. On the universality of the kolmogorov constant. Physics of Fluids 7, 2778–2784.

Stewart, R.H., Joy, J.W., 1974. HF radio measurements of surface currents. Deep-Sea Res. 21, 1039–1049.

Støle-Hentschel, S., Seemann, J., Nieto Borge, J.C., Trulsen, K., 2018. Consistency between sea surface reconstructions from nautical X-band radar doppler and amplitude measurements. J. Atmos. Oceanic Technol. 35, 1201–1220.

Swenson, M.S., Niiler, P.P., 1996. Statistical analysis of the surface circulation of the california current. Journal of Geophysical Research: Oceans 101, 22631–22645.

Taylor, G.I., 1921. Diffusion by continuous movements. Proceedings of the London Mathematical Society 2, 196–212.

Taylor, G.I., 1953. Dispersion of soluble matter in solvent flowing slowly through a tube. Proceedings of the Royal Society of London. Series A. Mathematical and Physical Sciences 219, 186–203.

Teague, W., Wijesekera, H., Jarosz, E., Lugo-Fernández, A., Hallock, Z., 2014. Wavelet analysis of near-inertial currents at the east flower garden bank. Continental Shelf Research 88, 47–60.

Thomas, L.N., Tandon, A., Mahadevan, A., 2008. Submesoscale processes and dynamics. Ocean modeling in an Eddying Regime 177, 17–38.

Thorpe, S.A., 2007. An Introduction to Ocean Turbulence. Cambridge University Press.

Timmermans, M.L., Winsor, P., 2013. Scales of horizontal density structure in the chukchi sea surface layer. Continental Shelf Research 52, 39 – 45.

Trizna, D.B., Hansen, J.P., Hwang, P., Wu, J., 1991. Laboratory studies of radar sea spikes at low grazing angles. J. Geophys. Res. 96, 12529–12537.

Tulloch, R., Smith, K., 2006. A theory for the atmospheric energy spectrum: Depth-limited temperature anomalies at the tropopause. Proceedings of the National Academy of Sciences 103, 14690–14694.

Tulloch, R., Smith, K.S., 2009. Quasigeostrophic turbulence with explicit surface dynamics: Application to the atmospheric energy spectrum. Journal of the atmospheric sciences 66, 450–467.

Van Sebille, E., England, M.H., Froyland, G., 2012. Origin, dynamics and evolution of ocean garbage patches from observed surface drifters. Environmental Research Letters 7, 044040.

Van Sebille, E., Griffies, S.M., Abernathey, R., Adams, T.P., Berloff, P., Biastoch, A., Blanke, B., Chassignet, E.P., Cheng, Y., Cotter, C.J., et al., 2018. Lagrangian ocean analysis: Fundamentals and practices. Ocean Modelling 121, 49–75.

Volkov, D.L., Lee, T., Fu, L.L., 2008. Eddy-induced meridional heat transport in the ocean. Geophysical Research Letters 35.

Wang, J., Flierl, G.R., LaCasce, J.H., McClean, J.L., Mahadevan, A., 2013. Reconstructing the ocean's interior from surface data. Journal of physical oceanography 43, 1611–1626.

Wang, Z., Hollebone, B., Fingas, M., Fieldhouse, B., Sigouin, L., Landriault, M., Smith, P., Noonan, J., Thouin, G., Weaver, J.W., 2003. Characteristics of spilled oils, fuels, and petroleum products: 1. composition and properties of selected oils. United States Enviromental Protection Agency .

Webb, E., 1964. Ratio of spectrum and structure-function constants in the inertial subrange. Quarterly Journal of the Royal Meteorological Society 90, 344–346.

Wetzel, L.B., 1990. Surface Waves and Fluxes. Kluwer, Dordrecht, the Netherlands. chapter Electromagnetic scattering from the sea at low grazing angles. pp. 109–171.

White, H.K., Hsing, P.Y., Cho, W., Shank, T.M., Cordes, E.E., Quattrini, A.M., Nelson, R.K., Camilli, R., Demopoulos, A.W., German, C.R., et al., 2012. Impact of the deepwater horizon oil spill on a deep-water coral community in the gulf of mexico. Proceedings of the National Academy of Sciences 109, 20303–20308.

Wright, J., 1968. A new model for sea clutter. IEEE Trans. Antennas Propag. 16, 217–223.

Yaglom, A., 1966. The influence of fluctuations in energy dissipation on the shape of turbulence characteristics in the inertial interval, in: Sov. Phys. Dokl., pp. 26–29.

Yaglom, A., 1994. An kolmogorov as a fluid mechanician and founder of a school in turbulence research. Annual review of fluid mechanics 26, 1–23.

Yaremchuk, M., Coelho, E.F., 2015. Filtering drifter trajectories sampled at submesoscale resolution. IEEE J. Oceanic Eng. 40, 497–505.

Young, I.R., Rosenthal, W., Ziemer, F., 1985. A three-dimensional analysis of marine radar images for the determination of ocean wave directionality and surface currents. J. Geophys. Res. 90, 1049–1059.

Young, W.a., Jones, S., 1991. Shear dispersion. Physics of Fluids A: Fluid Dynamics 3, 1087–1101.

Zambianchi, E., Griffa, A., 1994. Effects of finite scales of turbulence on dispersion estimates. Journal of marine research 52, 129–148.

Zang, X., Wunsch, C., 2001. Spectral description of low-frequency oceanic variability. Journal of Physical Oceanography 31, 3073–3095.

Zhang, H.M., Prater, M.D., Rossby, T., 2001. Isopycnal lagrangian statistics from the north atlantic current rafos float observations. Journal of Geophysical Research: Oceans 106, 13817–13836.

Zhang, Z., Wang, W., Qiu, B., 2014. Oceanic mass transport by mesoscale eddies. Science 345, 322–324.

Zhong, Y., Bracco, A., 2013. Submesoscale impacts on horizontal and vertical transport in the gulf of mexico. Journal of Geophysical Research: Oceans 118, 5651–5668.

Zhong, Y., Bracco, A., Villareal, T.A., 2012. Pattern formation at the ocean surface: Sargassum distribution and the role of the eddy field. Limnol. Oceanogr. 2, 12–27.

Zhurbas, V., Lyzhkov, D., Kuzmina, N., 2014. Drifter-derived estimates of lateral eddy diffusivity in the world ocean with emphasis on the indian ocean and problems of parameterisation. Deep Sea Research Part I: Oceanographic Research Papers 83, 1–11.

Zhurbas, V., Oh, I.S., 2004. Drifter-derived maps of lateral diffusivity in the pacific and atlantic oceans in relation to surface circulation patterns. Journal of Geophysical Research: Oceans 109.